

Thermodynamics, Geometry and Electronic Structure of Confined systems

By

Prachi Chandrachud

Adviser

Prof. Mihir Arjunwadkar

THESIS SUBMITTED IN TOTAL FULFILLMENT OF THE REQUIREMENTS OF
THE DEGREE OF
DOCTOR OF PHILOSOPHY
IN PHYSICS

October 2012

*Department of Physics, University of Pune,
Pune - 411007, India.*

Thermodynamics, Geometry and Electronic Structure of Confined systems

By

Prachi Chandrachud

Adviser

Prof. Mihir Arjunwadkar

Co-Adviser

Prof. D. G Kanhere

October 2012

Department of Physics, University of Pune,

Pune - 411007, India.

Declaration

I hereby declare that the present thesis entitled

‘Thermodynamics, Geometry and Electronic structure of Confined systems’

is an account of original work carried out by me. This work or part of the work thereof has not been submitted to any other university or institution for the award of any degree/diploma.

Prachi Chandrachud
Candidate
Department of Physics
University of Pune,
Pune, India

Certificate

This is to certify that the work in this thesis

**‘Thermodynamics, Geometry and Electronic structure of
Confined systems’**

submitted by Prachi Chandrachud was carried out by the candidate under my guidance. Such material as has been obtained from other sources has been duly acknowledged in the thesis.

Prof. Mihir Arjunwadkar
Thesis Advisor
University of Pune, Pune,
India.

Prof. D. G. Kanhere
Co-guide
University of Pune, Pune,
India.

To My Family.....

Contents

Acknowledgement	iv
Acronyms	v
Abstract	vi
List of Figures	xi
List of Tables	xvi
1. Introduction	1
1.1 Introduction to confined systems	1
1.2 Electronic structure of Graphene and <i>Graphane</i>	6
1.2.1 Basics of Graphene and <i>Graphane</i>	6
1.2.2 Lattice structure of Graphene.....	10
1.2.3 Graphene : Synthesis and Properties.....	13
1.3 Pure and hydrogenated GNR inside carbon nanotubes	17
1.3.1 Graphene nanoribbons	17
1.3.2 Carbon nanotubes.....	21
1.3.3 Functionalization of carbon nanotubes	25
1.4 Thermodynamics of small clusters	27
1.4.1 Introduction to clusters	28
1.4.2 Thermodynamics	30
1.4.3 Effect of doping	33
1.4.4 Experimental methods.....	35
1.5 Organization of thesis	37
2. Theoretical Framework	40
2.1 Early Approximations	40
2.1.1 Many body problem.....	41
2.1.2 Hartree and Hartree-Fock Theory	42
2.2 Density functional formalism	44
2.2.1 HK theorems and Kohn-Sham formalism.....	44
2.2.2 Exchange correlation functionals	48

2.2.3 Solving Kohn-Sham Equations	49
2.3 Pseudopotentials	51
2.4 Molecular dynamics	55
2.5 Tools and techniques	57
2.5.1 Geometry optimization	58
2.5.2 Ground state properties	60
2.5.3 Thermodynamic indicators.....	62
2.6 Error Analysis.....	67
3. Thermodynamics of carbon-doped Al and Ga clusters: Ab initio molecular dynamics simulations.....	73
3.1 Introduction.....	73
3.2 Computational Details.....	75
3.3 Results and Discussions	76
3.4 Summary and Conclusions.....	86
4. Stability of gold cages (Au₁₆ and Au₁₇) at finite temperature.....	88
4.1 Introduction.....	88
4.2 Computational Details	89
4.3 Results and Discussions.....	91
4.4 Summary and Conclusions	98
5. A systematic study of electronic structure from Graphene to <i>Graphane</i>...	100
5.1 Introduction.....	100
5.2 Computational Details	102
5.3 Results and Discussions.....	103
5.3.1 Magnetism	116
5.3.2 Tuning the electronic structure with hydrogenation.....	117
5.4 Summary and Conclusions	119
6. Electronic structure of GNR and H-GNR encapsulated in SWNT	121
6.1 Introduction.....	121
6.2 Computational Details	122
6.3 Results and Discussions.....	123

6.3.1 Pure GNR inside CNT	123
6.3.2 50%H GNR inside CNT	131
6.3.3 Fully hydrogenated GNR (H-GNR)	133
6.4 Summary and Conclusions	135
7. Outlook	136
References	138
List of Publications.....	154

Acknowledgement

For the past five years, I have experienced immense pleasure of learning, exploring and experimenting many aspects of theoretical physics. I express my sincere gratitude to my supervisor, Prof. Mihir Arjunwadkar who has been a guide, philosopher and friend. His constant encouragement and support has made this work possible. I am also thankful to my co-guide, Prof. D. G. Kanhere whose academic guidance has encouraged me to peruse my research work patiently. I am grateful to Prof B. Dey and Prof. Anjali Kshirsagar for their guidance.

I am very lucky to have extremely supportive and friendly seniors and colleagues in Advanced Computational Lab. Kavita and Shailaja are probably my early tutors when I was struggling with Linux coding. Bhalchandra and Soumyajyoti have been very helpful and supportive colleagues with whom I have thoroughly enjoyed lot of discussions especially during ‘graphene’ problem. My lab-mates Vaibhav, Mal-Soon, Shahab, Ghazi, Ideh, Dhani, Chacko, Ghazal and Aniruddha have always been very friendly and enthusiastic.

I would take up this opportunity to thank Head of the Physics Department, faculty members of CNC and CMS for infrastructure and computational facilities. I am also thankful to our collaborator, Prof. B. Sanyal for his contribution in the work. I am also grateful to Prof. (retd.) K. M. Kulkarni for sharing lots of secrets of networking with me.

Thanks to Linux, VASP and VMD package that have added flavors and colors to this work. Thanks to google and all those web pages too, I owe a lot to the creators of all these.

My parents are my first ‘Gurus’ and they have always been the source of encouragement and support throughout this journey. I have no words to express my feelings towards them. My husband, Avinash has always stood by my side firmly and boosted me all the time. Last, but no least, I am thankful to my dear son, Adit, who has been very understanding and cooperative. Without my family members, this work wouldn’t have been possible.

I dedicate this thesis to my family.

Prachi

Acronyms

Abbreviations	Meaning
CNT	Carbon nanotubes
GNR	Graphene nanoribbons
A-GNR	Armchair graphene nanoribbon
Z-GNR	Zigzag graphene nanoribbon
MWNT	Multiwalled carbon nanotube
SWNT	Single walled carbon nanotube
HOMO	Highest occupied molecular orbital
LUMO	Lowest unoccupied molecular orbital
DFT	Density functional theory
HK	Hohenberg Kohn
KS	Kohn Sham
LDA	Local density approximation
GGA	Generalized gradient approximation
C_v	Specific heat
COM	Center of mass
MSD	Mean square displacement
δ_{rms}	Root mean square bond length fluctuations
MD	Molecular dynamics
BOMD	Born-Oppenheimer molecular dynamics
ELF	Electron localization function
MH	Multiple histogram
PP	Pseudopotentials
PW	Plane Wave
USPP	Ultrasoft Pseudopotential

Abstract

The physics of low dimensional systems has attracted much attention during the past decade or so. These systems refer to the structures that extend to less than 3 dimensions. Clusters, thin films, quantum dots, nanotubes and nanowires are some well known examples of the systems with reduced dimensions. One of the interesting properties shared by these systems is ‘confinement effect’ in the sense that the entities are specially restricted. The clusters, for example are zero dimensional systems, which are formed by aggregation of few to hundreds of atoms. Their properties are very different from those of their bulk counterparts. During the past decade, atomic clusters have attracted much attention due to their importance in understanding nanoscale materials. One dimensional materials such as nanowires, nanotubes and nanoribbons show unique properties in terms of the conductivity. Carbon nanotubes (CNT) are well known to possess semiconducting or metallic behavior dependant on the diameter and chirality. Yet another recently synthesized (quasi) one dimensional structure called as graphene nanoribbon (GNR) shows width dependant band gap. These are unzipped carbon nanotubes having zigzag or armchair edge patterns. A recently synthesized ‘graphene’ is the most exciting discovery in this century.’ It is one atom thick two dimensional sheet of sp^2 bonded carbon atoms having zero band gap. All these systems noted above are confined because of their reduced dimensions. It is also possible to fabricate the confined systems by inserting the atoms, molecules or clusters inside nanotubes or buckyballs. This is the case of ‘physically confined system’. In general, the hollow space inside the nanotubes can be used as a natural confinement for inserting the atoms and molecules.

In the present work, we have studied the thermodynamics and electronic structure of few confined systems, namely, melting behavior of clusters and electronic structure calculations of graphene, hydrogenated graphene (*graphane*), graphene nanoribbons and carbon nanotubes. All the calculations are carried out using Density Functional Theory (DFT).

The first chapter is an introductory chapter. We have discussed the interesting properties, possible applications of the confined systems under study. We also take a brief review of related experimental and theoretical work pertaining to the topic. The melting in clusters has also been addressed elaborately.

In the second chapter, the detail discussion on density functional theory is carried out, as it is the key tool for all the calculations. It is followed by the discussion on molecular dynamics. Various data analysis tools are noted thereafter along with the error analysis.

In the first problem (chapter three) we have carried out extensive first principal thermodynamic simulations of carbon doped Al_{13} and Ga_{13} clusters. The doping with an impurity is an effective way to tune the melting temperature of the host cluster. In the present case, doping Al_{13} and Ga_{13} with a tetrahedral impurity like carbon, makes these 40 electron shell closed system under jellium approximation having enhanced stability. The host clusters are known to have distorted icosahedra and decahedral geometry respectively. Interestingly, the doped clusters Al_{12}C and Ga_{12}C exhibit a perfect icosahedral structure with carbon atom at the center. The bond length calculation between the surface and the central atom in all four clusters reveals that the presence of carbon shortens the bond lengths between central carbon and outer surface atoms. Examination of the various isosurfaces of total charge densities brings out the difference in the nature of bonding between the host and the doped clusters. Al_{13} shows a delocalized, well spread charge density while Ga_{13} shows typical covalent bonding. Upon doing, significant changes are seen. For both the doped clusters, most of the charge is around the central carbon atom and is spherically symmetric. Evidently there is a charge transfer from all surface atoms towards the central carbon. This establishes a partial ionic bond between central carbon and surface atoms and the size of cluster shrinks. This also results in weakening of the bonds on the surface atoms. As a result the melting temperature of the doped clusters is lowered than the host clusters. The calculated melting temperatures for Al_{13} and Ga_{13} are 1800 K and 1200 K respectively while the doped clusters melt at around 800-900 K. These results are supported by the mean square displacement and root mean square bond length fluctuation.

Next, we have investigated the finite temperature behavior of smallest gold cages namely Au_{16} and Au_{17} using *ab initio* method (chapter four). The nano-gold has wide applications as catalysis, medicine, electronic circuits etc. Gold clusters are known to exhibit caged structures for $n=16, 17$ as well as for higher number of atom clusters. The stability of these cages at finite temperature is an important issue for the application point of view. Here, we have examined the melting, geometry and various isomers of the smallest gold cages Au_{16} and Au_{17} . Au_{16} is known to be a flat cage

while Au₁₇ is a hollow one. We have analyzed almost 50 isomers for both the clusters even 0.4 eV above the ground state and we have demonstrated a close relation between the isomer energy distribution and melting of the cluster. Our results show that Au₁₆ shows rather a broad specific heat curve ranging from 600 K to 1000 K while Au₁₇ exhibits a noticeable peak at 900 K which is identified as a melting peak. The analysis of the ionic trajectories and other phase change indicators such as mean square displacement and radial distribution function, clearly indicate that Au₁₇ is very stable and retains the shape upto 1000 K. Au₁₆ on the other hand, distorts significantly. The diffusive motion of the atoms begins at 600 K resulting in isomerization and the open cages structures are seen above 1000 K. According to Bixon and Jortner, the continuous isomer energy distribution leads to a broad peak in specific heat curve while branch-like distribution gives a peak. Our results show that Au₁₆ has a continuous isomer energy distribution while that of Au₁₇ is step-like. This leads to variation in their behavior at finite temperature. Specific heat curve for Au₁₆ has a very broad peak ranging from 600 K to 1000 K whereas Au₁₇ has a relatively sharper peak.

The third problem (chapter five) deals with the electronic structure calculation of graphene and *graphane* via partial hydrogenation. Graphene is a 2D one atom thick sheet of sp² bonded carbon atoms with zero band gap. Although, graphene exhibits many novel properties such as ‘linear dispersion at Fermi level, anomalous quantum hall effect, Klein paradox etc.’, due to the absence of band gap, it has limitations in the use of semiconducting field. Amongst the various ways proposed to open the gap in graphene, complete hydrogenation is the effective way. The fully hydrogenated structure is called as ‘*graphane*’ and has a DFT predicted band gap of 3.5 eV. In this work, we have probed the transition from zero gap graphene to *graphane* via successive hydrogenation. We have analyzed about 18 systems from 2% hydrogenated graphene to 90%H via DFT simulations. The first interesting issue that is addressed is the minimum energy configuration of the hydrogen atoms to decorate the graphene lattice. Our extensive simulations for different configurations (namely random placement of H, 2 islands, different edge patterns etc) of hydrogenated graphene show that hydrogens prefer to form a single compact island. We carried out such calculations for systems upto 50%H and with 2-3 different unit cells. Next, the analysis of the density of states (DOS) close to Fermi level brings out interesting features. For low hydrogen concentration, the V-shape DOS in pure graphene is

disturbed slightly due to loss of symmetry. As the hydrogen coverage increases there is a significant increase in the value of DOS at the Fermi level. The hydrogenated carbon atoms are now moved out of the graphene plane, in turn the lattice is distorted and the symmetry is broken. As a consequence, more and more k points in the Brillouin zone contribute to the DOS near Fermi level. The region ranging from 30% coverage to about 70% coverage is characterized by the finite DOS of the order of 2.5 near the Fermi energy. Above 80% or so, there are too few bare carbon atoms available for the formation of delocalized π bonds. The value of DOS approaches zero and a gap is established with a few midgap states. It may be emphasized that the presence of states around the Fermi level giving finite DOS does not guarantee that the system is metallic unless we examine the nature of localization of the individual states. Therefore we have examined the energy resolved charge densities of the states near the Fermi level. A particularly striking feature is the formation of two spatially separated regions. The hydrogenated carbon atoms do not contribute to the charge density giving rise to the insulating regions while the neighboring bare carbon atoms form conducting regions via π bonding. This feature is prominent in the region from 30%-70% hydrogenated cases giving rise to the channels of delocalized bare carbon atoms. Since above 75%H, there are insufficient number of bare carbon atoms to form contiguous channels, the mid gaps occur. To summarize, as the hydrogen coverage increases, graphene with a semi-metallic character turns first into a metal and then to an insulator. The metallic phase has some unusual characteristics: the sheet shows two distinct regions, a conducting region formed by bare carbon atoms and embedded into this region are the non-conducting islands formed by the hydrogenated carbon atoms. However it should be noted that hydrogenated systems chosen in this work are such that the energy is always minimum. These are the naturally preferred arrangements of the hydrogen atoms decorating graphene. The specially designed patterns of hydrogenated graphene can yield various band gaps. We have demonstrated such designed channels of hydrogenated graphene giving zigzag and armchair edge patterns and their effect on the band gap modulation.

In the last problem (chapter six), we have investigated the stability and confinement effects of graphene and H-graphene nanoribbon (GNR) encapsulating inside carbon nanotubes (CNT). GNR are of particular interest because they are known to exhibit width dependant band gaps. The recent calculations by two groups show that GNR can be stabilized by encapsulating in CNT. In the present work, we

have inserted the smallest (20 carbon atom unit cell) graphene and H-graphene ribbons inside the carbon nanotubes of diameters ranging from 8Å to 17Å. (The confinement effect on the geometry and the stability of the ribbons has been studied.) Firstly, the geometries of pure GNR are sensitive to the CNT radii. There is a tendency to break the vertical bonds as radius is increased. We observe the formation of 2 chains in the largest diameter CNT. The observed DOS for all the structures show that there is a substantial enhancement at Fermi energy in all the cases which mainly arises from p_z and p_y of GNR atoms. In the largest tube, the 2 chains exhibit delocalized charge density and solely contribute to Fermi level. These findings are confirmed by the analysis of site projected DOS and partial charge density counters. The structure and DOS pattern do not vary significantly for semiconducting CNT except for the states at Fermi occur in the gap of the tube. For hydrogenated GNR, we have studied 50%H and fully hydrogenated GNR encapsulated in CNT. For 50%H case, it has been observed that the geometries inside CNT are sensitive to the placement of the hydrogen atoms. The systematically placed hydrogens (on GNR) go over in-plane positions and resulting geometries are independent of the diameter considered. The structure is planer leading to hydrogen terminated GNR. On the other hand, the randomly placed hydrogens show diameter dependant structures retaining the tendency to form parallel chains by breaking the vertical bonds in large diameter tubes; however structures are modulated by strong C-H bond leading to displacements of carbons away from planer or linear shape. Lastly, we have examined fully hydrogenated GNR. Remarkably the optimized geometries are not sensitive to the diameter at all. The final structure remains the same, namely two parallel chains in all types of CNT. In the present case the carbon atoms show zigzag arrangement, as each atom is pulled by the attached hydrogen. The two chains are symmetrically placed with respect to the tube axis due to stronger confinement. The DOS for both types of tubes show enhancement at Fermi level. The isosurfaces of partial charges densities clearly show delocalized nature along the two chains which arises from the p_z orbitals of GNR carbons atoms. The contribution of both the chains is equal unlike in the case of pure GNR. In semiconducting tube, we get two stable conducting channels. Our results bring out the possibility of tuning the geometries of GNR and H-GNR inside CNT of different diameters to obtain one dimensional or two dimensional structures.

List of Figures

1.1	The DOS per volume and energy for free electron gas in 3D (blue curve), 2D (red curve), 1D (green curve) and zero dimensional system (black lines). (http://ecee.colorado.edu/~bart/book/welcome.htm) . . .	4
1.2	(a) Structure of graphene. The carbon atoms are in-plane and sp^2 -bonded in graphene. (b) <i>Graphane</i> in chair conformer. The hydrogen atoms are attached in an alternating manner to each carbon. The <i>graphane</i> structure is no more planer as hydrogens pull the carbon atoms.	7
1.3	The band structure and density of states of pure <i>graphane</i> . The band gap of 3.5 eV is seen at τ point while at K point the band gap is large. .	9
1.4	(a) The Graphene honeycomb lattice with two point basis. (b) The same lattice formed with two triangular sub lattices and corresponding reciprocal lattice [32].	11
1.5	Dispersion relation in graphene. Inset: energy bands close to Dirac points [32].	13
1.6	Single atom thick sheets of graphene obtained by adhesive tapes as shown in scanning electron micrographs. (Foundation of Fundamental Research on Matter, Netherlands).	15
1.7	(a) Zigzag GNR with atoms A and B alternately arranged along the edge (b) Armchair GNR with A-B dimer forming the edge pattern [71]. Note that the coordinate axis in (b) is rotated 90° , with respect to (a).	18
1.8	(a) SWNT and GNR (b) plasma etching of partially embedded CNT (c) longitudinal cutting of CNT by chemical attack (d) intercalation of alkali metal atoms followed by exfoliation of CNT and (e) metal particle catalyzed cutting of CNT (f) Final GNR. [77].	19
1.9	A representation of graphene sheet rolled to form a carbon nanotube. The chirality vector, zigzag and armchair vectors are shown. (Image courtesy: http://www.wikipedia.org).	21
1.10	Three types of carbon nanotubes formed by the way the graphene sheet is rolled. The numbers in the bracket indicate n,m parameters. .	22
1.11	(a) Band structure of graphene showing main high symmetry points (b) Allowed k vectors of CNT's mapped onto graphene Brillion zone [95]. .	23
1.12	DNA wrapped CNT (Image courtesy - A. Jagota)	26
1.13	A comparative picture of the shell closure in an atom and a cluster [156].	29

1.14	Heat capacity curves for Al_n^+ ($n= 49$ to 62) clusters [191]. The points are the experimental measurements, and the dashed lines are calculated heat capacities derived using a modified Debye.	32
1.15	The Ga_{30} and Ga_{31} clusters - geometry and heat capacity curves [193].	32
2.1	The all electron wavefunction and potential (blue color) and pseudo-wavefunctions and potential (red color). All the quantities are shown as a function of distance r from the atomic nucleus.	52
2.2	(a) A two dimensional graph explaining the concept of local and global minima (b) The saddle point in a 3D plot shown.	59
2.3	Isosurfaces of ELF for (a) Ga_{13} and (b) $Ga_{12}C$ at value 0.67.	62
2.4	Multiple Histograms for Au_{16} cluster. The temperatures range from 200 K to 2000 K and the histograms show a good overlap.	68
2.5	Multiple Histograms for Au_{16} cluster with 325 K and 850 K are omitted as compared to figure 2.4. The missing temperatures are evident by a gap after 250 K and 700 K.	69
2.6	The specific heat curves calculated using 'all' temperatures and 'omitted' temperatures for Au_{16}	69
2.7	The specific heat for Au_{16} plotted with different bin widths. It is clear that for all three bin widths C_v has converged.	70
2.8	The specific heat for Au_{16} plotted with different simulation time. The convergence is seen as the simulation time is increased upto 120ps. .	71
3.1	The ground state geometries of (a) Al_{13} - distorted icosahedra (b) $Al_{12}C$ - perfect icosahedra (c) Ga_{13} - decahedra and (d) $Ga_{12}C$ - perfect icosahedra.	77
3.2	Isosurfaces of total charge density at various values for all the clusters. The values of the maximum charge density for Al_{13} and Ga_{13} are 0.26 and 0.28, respectively, while for $Al_{12}C$ and $Ga_{12}C$ are 1.50 and 1.60, respectively.	79
3.3	Isosurfaces of charge density for the molecular orbital (HOMO -2) at about $1/4^{th}$ of the maximum value.	80
3.4	Eigenvalue spectra for all the systems. The topmost short line (blue) indicates LUMO.	80
3.5	Normalized specific heat for Al_{13} and $Al_{12}C$. Note that shapes of the specific-heat curves are similar, but the melting temperature is lowered by almost 800 K upon doping.	81
3.6	Normalized specific heat for Ga_{13} and $Ga_{12}C$. The $Ga_{12}C$ is a sharp peak as compared to Ga_{13}	82
3.7	Isosurfaces of ELF for Ga_{13} and $Ga_{12}C$ at the value of 0.67.	83

3.8	Mean square displacement for Ga ₁₃ and Ga ₁₂ C at 325K. The MSD are shown for individual atoms.	84
3.9	$\bar{\delta}_{\text{rms}}$ for surface atoms (filled circles, blue) and central atom (filled diamonds, red) for all the clusters averaged over 90ps.	86
4.1	The ground state geometries and various isomers of Au ₁₆ . The numbers correspond to the difference in the energy with respect to the ground state.	92
4.2	The ground state geometries and various isomers of Au ₁₇ . The numbers correspond to the difference in the energy with respect to the ground state.	93
4.3	Normalized specific heat for Au ₁₆ and Au ₁₇	94
4.4	Mean square displacements of Au ₁₆ over 120 ps.	96
4.5	Mean square displacements of Au ₁₇ over 120 ps.	96
4.6	Radial distribution function of Au ₁₇	97
4.7	The distribution of isomer energies for Au ₁₆ and Au ₁₇	98
5.1	Different hydrogen decorations for 50% concentration. In the figure, yellow (lightly shaded in print) balls are bare carbon atoms, turquoise (darker shades in print) balls are hydrogenated carbons and red (small dark in print) balls are hydrogen atoms.	105
5.2	The total DOS for hydrogenated graphene for various hydrogen concentrations below 90%. The zero of the energy is taken at the Fermi level and is marked by a vertical line. X axis denotes $E - E_f$. (a) Graphene; (b) 4% hydrogen; (c) 16% hydrogen; (d) 20% hydrogen; (e) 30% hydrogen; (f) 50% hydrogen; (g) 60% hydrogen; (h) 70% hydrogen; (i) 80% hydrogen; (j) 85% hydrogen.	109
5.3	The total DOS for hydrogenated graphene for various hydrogen concentrations above 90%. The zero of the energy is taken at the Fermi level and is marked by a vertical line. X axis denotes $E - E_f$. (a) 92% hydrogen; (b) 94% hydrogen; (c) 96% hydrogen; (d) 98% hydrogen; (e) <i>graphane</i>	110
5.4	Site projected DOS for hydrogenated carbon sites (dotted line) and bare carbon sites (continuous line) for hydrogen coverage of 40%. Almost all the contribution comes from the p _z which has been shown in the figure. Note that only bare carbon atoms contribute to the DOS at the Fermi level.	112
5.5	Variation of the value of DOS at the Fermi level as a function of hydrogen coverage.	113
5.6	Isosurfaces of charge densities of bands near the Fermi level (see text). For comparison, the charge density of graphene at the Dirac point is also shown. (a) Graphene (b)40% hydrogen; (c) 70% hydrogen; (d) 92% hydrogen.	115

5.7	ELF plots with two different isosurface values for 70% hydrogen concentration. (a) shows for isosurface value 0.75 and (b) shows for isosurface value 0.62.	116
5.8	(a) Spin density (b) total DOS (c) and (d) site projected (p_z only) DOS for two bare carbon atoms from two different sublattices. X axis of the plots denotes $E - E_f$. This figure is for 50% hydrogen coverage.	117
5.9	Decoration of hydrogen (a) along the diagonal of the unit cell and (b) along the edge of the unit cell. The yellow atoms are the bare carbon atoms. (c) DOS plots for the two cases. The lone atoms seen are from repeating super cells.	118
6.1	Free standing and optimized geometries of graphene ribbons in the metallic CNT. (a) Original GNR (b) Ring structure having 8 atoms is seen to sustain in the smallest tube. (c) Formation of a single oval shape is seen in larger diameter. (d) Well separated, curved 1-d chains in the largest tube are not placed symmetrically with respect to the axis. The average distance between the chains is 3.8Å.	124
6.2	Optimized geometries of graphene ribbons in the semiconducting smallest and largest CNT. (a) Ring structure is having 12 atoms in the smallest tube. (b) Well separated, almost linear 1-d chains in the largest tube indicate that the degree of confinement plays important role in determining the geometry. The average distance between the chains is 3.8Å.	125
6.3	(a) Total DOS for pure GNR in metallic tube S1. The zero of the energy is taken at the Fermi level and is marked by a vertical line. X axis denotes $E - E_f$. The DOS for pure tubes are also shown for reference. (b) Corresponding isosurfaces of charge densities at $1/10^{th}$ of the maximum value. These are the charge densities of the states very close to the Fermi level. At this value the contribution from tube carbon atoms is negligible. The enhancement seen at Fermi is purely from the end-carbon atoms of GNR as shown. (c) The contribution to the prefermi peak is from all the carbons atoms of GNR.	126
6.4	(a) Total DOS and (b) Corresponding isosurfaces of charge densities (close to Fermi) at $1/10^{th}$ of the maximum value in metallic CNT M2. Carbons atoms from one side of the oval GNR contribute more than the other. This contribution is seen in DOS at Fermi. (c) DOS and (d) Isosurfaces of charge densities (close to Fermi) at $1/10^{th}$ of the maximum value for M3. There is a clear enhancement seen at Fermi level retaining the nature of tube DOS. Chain A being close to the wall contributes more than other chain.	127
6.5	(a) Total DOS for pure GNR in S1. The zero of the energy is taken at the Fermi level and is marked by a vertical line. X axis denotes $E - E_f$. The DOS for pure tube is also shown for reference. The states occurring at Fermi level are due to the GNR atoms. (b) Corresponding isosurfaces of charge densities (close to Fermi) at $1/10^{th}$ of the maximum value.	128
6.6	(a) Total DOS for S2. The zero of the energy is taken at the Fermi level and is marked by a vertical line. X axis denotes $E - E_f$. The DOS	

	for pure tube is also shown for reference (red color).The states seen at Fermi are due to GNR atoms only. (b) Corresponding isosurfaces of charge densities (close to Fermi) at $1/10^{th}$ of the maximum value. (c) Isosurfaces near the prefermi peak depicting contribution only from the CNT atoms.	129
6.7	Total DOS for GNR in S3. The corresponding geometry is same as shown in figure 6.2-(b), i.e two parallel chains. The GNR atoms contribute to Fermi giving the midgap states.	129
6.8	Site projected DOS for graphene nanoribbon in the S1. The prominent contribution towards the peak before Fermi level is from the from the end carbon atoms of the ribbon.	130
6.9	Original geometries for 50%H-GNR – (a) Systematic and (b) random placement in CNT. (c) The SH structure becomes planer after optimization in all CNT (d) RH forms some intermediate shapes in the smaller diameter CNT (e) separated chains in the largest CNT. Note the effect of attached hydrogens leading to distortions.	132
6.10	Superimposed DOS for 50%H systematic placement. The zero of the energy is taken at the Fermi level and is marked by a vertical line. X axis denotes $E - E_f$	133
6.11	(a) Original H-GNR consisting of 20 carbon and 20 hydrogen atoms. (b) Optimized geometry is same in all CNT, namely parallel stripes with the separation distance varying from 2.58Å to 4Å as the diameter is varied (c) and (d) DOS of H-GNR in a metallic tube and semiconducting tube resp. showing added states at Fermi. (e) Partial charge density shown for semiconducting CNT. The delocalized nature is evident and is observed for H-GNR in all CNT. (f) Close view of the bonding in H-GNR.	134

List of Tables

3.1	The symmetry, bond lengths, HOMO-LUMO gap and melting peak for pure and doped clusters. The bond lengths are shown between the central and surrounding atoms.	77
5.1	Shifted binding energies (BE) for different configuration of 20% coverage (10H + 50C). The binding energy of the most stable structure is the reference (zero) level. The more negative binding energy means more negative structure.	103
5.2	Shifted binding energies (BE) for different configuration of 50% coverage as shown in figure 4.1. The binding energy of the most stable structure is the reference (zero) level. The more negative binding energy means more unstable structure.	106
5.3	Shifted binding energies (BE) (eV) and the magnetic moments (μ_B) of four hydrogen vacancies. The binding energy of the most stable structure is the reference (zero) level. The more negative binding energy means more unstable structure.	107
6.1	CNT of different diameters used and their short forms.	124
6.2	Binding energies for GNR and H-GNR in different nanotubes.	135

1. Introduction

1.1 INTRODUCTION TO CONFINED SYSTEMS

In the past decade the low dimensional systems have become the subject of immense research interest. These mainly refer to the structures that extend to less than three dimensions and belong to the class of materials intermediate to that of atomic and bulk scales. The typical length scale of these systems falls in nanoregim that is in the range of few to few hundred nanometers¹. In recent years some novel materials such as clusters, quantum dots, nanotubes, nanowires and two dimensional systems like graphene have been the focus of current research.

An interesting feature shared by all such systems is ‘confinement’; that is the atoms and consequently the electrons are restrained to move in less than 3 dimensions. For example, low dimensional systems such as carbon nanotubes (CNT), graphene nanoribbons (GNR) and graphene are confined in two and one dimensions respectively while clusters are confined in all the directions. One may view these examples as confinement imposed due to reduced dimensionality. The other way is to physically confine the systems such as encapsulation with nanotube where the confined systems are restricted due to the outer boundary of the tube. Indeed the effect of such confinements on the geometry, electrical, chemical and mechanical properties is a subject of immense research interest. The present thesis examines the properties of some confined systems – 1. Clusters (zero dimensional systems) 2. Graphene and *graphane* (two dimensional systems) and 3. GNR encapsulated in CNT.

Clusters are ‘self confined’ due to the interactions between the atoms, leading to various shapes and geometries and are considered as zero dimensional systems. The finite size of the clusters makes them distinct from the single ‘atom’ and infinite ‘solid’. During the past decade, atomic clusters have attracted much attention due to their importance in understanding nanoscale materials [1,2]. It is now well established that the physical and chemical properties of such finite size systems are

¹ One nanometer spans 3-5 atoms in a row.

1. Introduction

different from their bulk counterparts [3, 4, 5, 6, 7, 8, 9] in terms of the geometry, nature of bonding, electronic, magnetic and thermodynamic properties. The clusters have been largely investigated (via experiments and simulations) due to the possibility of building ‘superatom’ and ‘cluster assembled materials’ [10, 11]. We shall review some interesting properties of clusters in section 1.4 in details.

Next, the nanotubes, nanowires and nanoribbons are specially constructed one dimensional systems. Carbon nanotubes are the members of the fullerene structure family, which also includes the spherical buckyballs. The carbon nanotubes being conducting or semiconducting are extremely useful in nanotechnology, electronics, optics and other fields of material science. Graphene nanoribbons (GNR) are one of the recent findings belonging to one dimensional system. These are the unzipped carbon nanotubes having zigzag or armchair type of edge patterns. GNR fascinate the researchers because they show width dependant band gap mechanism which is the outcome of one dimensional confinement.

A recently synthesized ‘graphene’ is one of the most exciting discoveries in this century.’ It is one atom thick, two dimensional sheet of sp^2 bonded carbon atoms having unique properties. The Nobel Prize for the year 2010 was awarded to Andre K. Geim and Konstantin Novoselov for “the groundbreaking experiments regarding the two-dimensional material of graphene”. The single layered honeycomb structure of graphene makes it the “mother” of all carbon-based systems. The commonly found graphite is simply a stack of graphene layers bonded by weak Van der Waals interaction. Next, carbon nanotubes are made of rolled-up sheets of graphene while the buckyballs are nanometer size spheres of wrapped-up graphene. All these forms of carbon were isolated long before graphene and have been used in many applications, but their electric, magnetic and elastic properties originate from the peculiar structure of graphene. Graphene is a semimetal with zero band gap. It shows a linear dispersion relation at Fermi level. The low energy electrons in graphene behave like massless Dirac fermions and are governed by Dirac equation. This peculiar property enables the electrons to travel for large distance without scattering or in other words graphene possesses very high electron mobility. Undoubtly, graphene has been a potential candidate for the applications in many areas such as electrodes, solar cells, ultra capacitors etc. Graphene based nanomaterials form a class of novel two dimensional systems that are being explored for various applications in nanotechnology. Apart

1. Introduction

from the unique dispersion relation, graphene also possesses number of exotic properties that are discussed in section 1.2. However, due to the absence of the band gap graphene is not suitable for electronic applications like transistors and diodes. Number of methods have been proposed so as to open a gap in graphene; fluorination, hydrogenation, vacancies or defects being some of the noticeable examples. Amongst these a beautiful example is completely hydrogenated graphene, called as *graphane*. Importantly, it yields a band gap of 3.5 eV as predicted by density functional theory. As a result of hydrogenation, the original sp^2 bonding in graphene is modified to sp^3 -like in *graphane*. We shall have more discussion on *graphane* in section 1.2.

So far we noted the systems that are naturally confined. However it is possible to physically confine the systems by encapsulating the atoms, molecules or clusters inside a nanotube. The idea is to use the hollow space as a natural confinement for inserting the atoms and molecules. Such a confinement can be used as a chemical reactor [12]. The interactions of the confining material with the enclosed atoms may play a role in determining the properties of the system. Indeed the idea has been probed with clusters, chains of carbon atoms and water molecules being inserted inside carbon nanotubes via experiments and many via simulations. One of the reasons of such confinement is to achieve the stable nanostructures which are highly difficult in free space. Recently an experimental synthesis showed that stable graphene nanoribbons are possible by encapsulating in carbon nanotube [12].

Yet important another class not addressed in the present work is quantum dots (QD). A quantum dot is defined as a system of interacting electrons in external confining potential. These are zero dimensional systems experimentally realizable due to advances in the fabrication technology. Because of their similarities with the atomic structures, they are considered as the artificial atoms. The quantum dots, formed by confining two dimensional gases are highly tunable in terms of the number of electrons and size. Therefore they represent important paradigms for investigating various properties of interacting many body systems. Their applications vary from single electron transistor, spectral detectors, lasers to even quantum computing. For more details on the topic, the reader can refer [13, 14, 15, 16].

The key to understand and analyse many of the properties of such confined systems is the ‘electronic structure’. By this we mean the analysis of the nature of orbitals, density of states, eigenvalues, band gaps, HOMO-LUMO gaps etc. We

1. Introduction

illustrate this by showing the DOS for simple jellium model for bulk, two, one and zero dimensional systems in figure 1.1

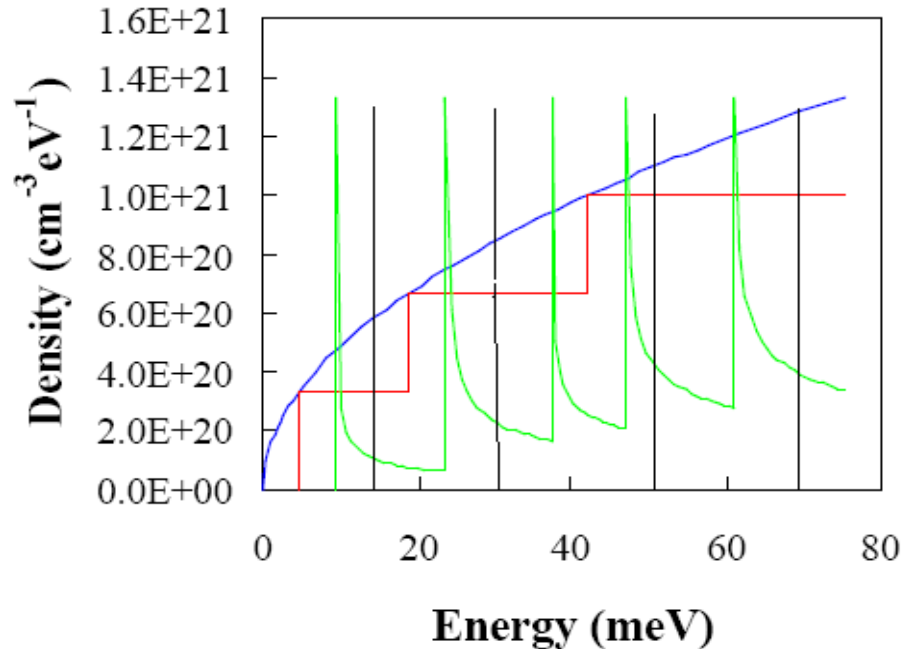


Figure 1.1 - The DOS per volume and energy for free electron gas in 3D (blue curve), 2D (red curve), 1D (green curve) and zero dimensional system (black lines). (<http://ecee.colorado.edu/~bart/book/welcome.htm>)

DOS are the number of accessible energy states in the small energy interval E to $E+dE$. In the simple free electron model the dramatic difference in DOS is seen as the dimensions are lowered. In 3D system, the DOS are proportional to the square root of total energy as shown by blue line in figure 1.1. The DOS in two dimensions is constant and does not depend on the energy. In zero dimensional case we expect a delta function. This example brings out the effect of dimensionality on the electronic structure properties. In short, the physics of low dimensional systems is different and interesting.

The theme of the present thesis is to explore the electronic structure of graphene, hydrogenated graphene (2D systems), GNR encapsulated carbon nanotubes (1D system) and the thermodynamic properties of clusters (0D systems). The specific problems we have investigated are:

1. Introduction

1. Thermodynamic for carbon doped Al_{13} and Ga_{13} clusters.
2. Melting transition in small gold cages namely Au_{16} and Au_{17} .
3. Electronic structure of graphene and *graphane*.
4. Graphene nanoribbons encapsulated inside carbon nanotubes.

In the first problem, we have investigated the role of carbon as a dopant on the melting of Al_{13} and Ga_{13} clusters. The 13 atom aluminum and gallium clusters are iso-electronic and are known to have different type of bonding. Their ground state geometries are symmetric and ordered ones, namely icosahedra and decahedra. The substitution of a single carbon makes both these clusters 40 electrons closed shell (in jellium sense) showing enhanced stability. Both the doped clusters exhibit perfect icosahedral symmetry. We have carried out ab-initio molecular dynamic simulations of pure Al_{13} , Ga_{13} and Al_{12}C , Ga_{12}C clusters to understand the melting phenomenon.

The second problem is the finite temperature analysis of the smallest cages of gold namely Au_{16} and Au_{17} . The gold nanoparticles are potential candidates in area of catalysis. The gold clusters undergo planer to non planer transition at $n=7-10$. There are experimental reports of the smallest cages of gold at $n=16, 17$. We have examined the ground state geometries, isomer distribution and melting features of both the clusters via simulations. It has been observed that there is a close association between the isomer energy distribution and the melting temperatures.

In the third problem, the electronic structure of two dimensional pure and hydrogenated graphene (*graphane*) has been investigated. Graphene is a zero gap semi metal while *graphane* is a semiconductor. The aim of the problem is to understand the way band gap opens upon hydrogenation. We have carried out series of extensive calculations for graphene system with concentration of hydrogen ranging from 0% to 100%. In addition, we also demonstrate that the designed channels of dehydrogenated *graphane* can be used to tune the band gap.

Pure and hydrogenated GNR encapsulated in CNT are investigated in the forth problem. Here, we examine the confinement effect of CNT with different radii on the geometry of pure and H-GNR. It is also observed that the placement of hydrogen plays an important role in stabilizing GNR inside CNT. The motivation for this work mainly comes from the recent experimental work by A. Talyzin *et.al.* [12]. They have explored very simple and efficient chemical synthesis method for preparation hydrogen terminated GNR encapsulated in single walled CNT. Formation of the GNR

1. Introduction

is possible due to confinement effects provided by the one-dimensional space inside nanotubes.

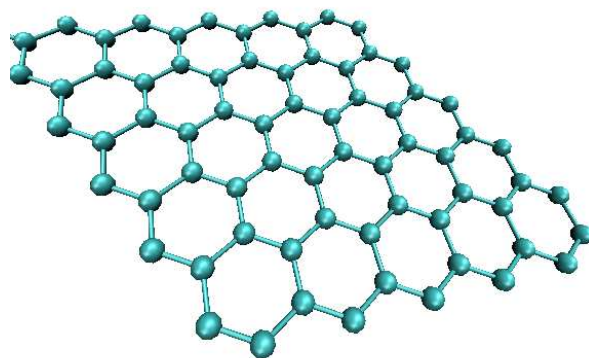
We close this section with some comments on the theoretical methods. Throughout this work we have used Density Functional Theory (DFT), a well established method to investigate the electronic structure of many body systems. For the thermodynamic data, Born Oppenheimer molecular dynamics is used. We have calculated the specific heat using multiple histogram technique. Additionally, standard phase change indicators such as ‘mean square displacements’ (MSD) and ‘root mean square bond length fluctuations’ (δ_{rms}) are also estimated. The detailed discussion on the above methods is given in Chapter 2.

1.2 ELECTRONIC STRUCTURE OF GRAPHENE AND GRAPHANE

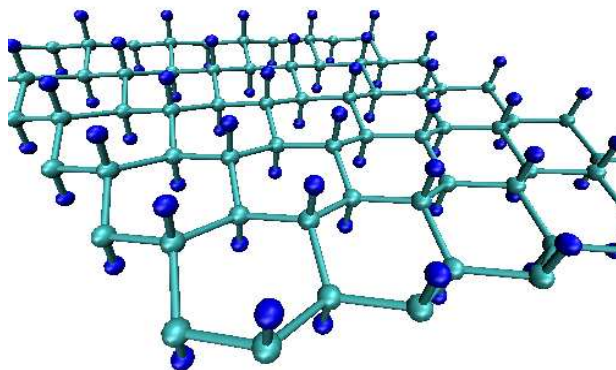
There has been a tremendous literature on graphene. Here we present the basic structure and few relevant properties of graphene followed by some interesting aspects of hydrogenated graphene that is *graphane*. At the end we will briefly review the methods of graphene synthesis.

1.2.1 Basics of Graphene and Graphane

Graphene is purely two dimensional material. It consists of one atom thick monolayer of the carbon atoms arranged in a hexagonal lattice as shown in figure 1.2-(a). The carbon atoms are sp^2 hybridized with the bond length of 1.42\AA . It can be also viewed as a single isolated sheet of graphite. Graphene was first isolated by Geim, Novoselov and group in series of experiments in 2004 [17, 18, 19]. The tight binding calculations show that it is a semimetal with zero band gap. The hexagonal Brillouin zone consists of two inequivalent \mathbf{k} points, namely K and K', called as Dirac points at which there is no gap. The conduction and valence bands meet at the Dirac points. Close to these crossing points, the electron energy $E(\mathbf{k})$ depends linearly on the wave vector \mathbf{k} obeying the relativistic Dirac equation. Thus electrons and holes in monolayer graphene are called Dirac fermions [18]. This peculiar property is an outcome of the triangular bipartite lattice as well as the typical sp^2 bonding of the carbon atoms. Section 1.2.2 covers the lattice structure of graphene in details.



(a)



(b)

Figure 1.2 - (a) Structure of graphene. The carbon atoms are in-plane and sp^2 -bonded in graphene. (b) *Graphane* in chair conformer. The hydrogen atoms are attached in an alternating manner to each carbon. The *graphane* structure is no more planar as hydrogens pull the carbon atoms.

Graphane, as stated earlier is completely hydrogenated graphene. It was first proposed by Sofo *et.al.* [20] and later experimentally synthesized by Elias *et.al.* [21]. In *graphane* the hydrogen atoms are attached in alternating manner to the carbon atoms with respect to the underlying plane. Since the underlying lattice is triangular bipartite, all hydrogens placed above the plane belong to one sublattice while those placed below the plane belong to different sublattice. This type of conformation is called as ‘chair-like conformer’ and is shown in figure 1.2-(b). *Graphane* exists in another type of conformation in which a pair of hydrogens is attached to the adjacent carbon atoms. Such an arrangement is called as ‘boat-like conformer’. Both the

1. Introduction

structures show a band gap of 3.5 eV and 3.7 eV as calculated by DFT², while GW method reports value of 5.4 eV for chair conformer [22]. Amongst these configurations, the chair conformer turns out to be energetically favored. In both types of configurations, the hydrogenation disturbs the planer geometry of graphene thereby pulling the carbon atoms above the plane.

We give the bird's eye view of the effect of hydrogenation on graphene. This subject is being intensely explored because of the possible applications. In pristine graphene, each carbon atom is sp^2 bonded with three neighboring carbon atoms leading to three planer σ bonds. These being filled form a deep valence band. The unpaired p_z orbital which is perpendicular to the plane binds covalently with neighboring carbon atom forming π band. Since each p_z orbital has one electron, π band is half-filled. A set of these π bonded orbitals gives rise to a peculiar conductivity in graphene. Upon complete hydrogenation, these unpaired π orbitals are bonded to hydrogens and are no more available for conduction. As a consequence the band gap opens up. The original sp^2 bonding is now modified into sp^3 -like with the calculated c-c bond lengths in chair conformer to be 1.52Å [20]. This bond length is close to that of 1.53Å in case of diamond. The band structure and density of states for *graphane* in chair conformer are shown in figure 1.3. It shows a direct band gap of 3.5 eV at τ point. This is interesting because graphene is gapless at K point while in *graphane* the gap at K point is as large as 12 eV. In the present work, we have examined the way this direct band gap opens as graphene is hydrogenated successively from low hydrogen concentration to full.

Graphane has been found to be the most stable amongst other hydrocarbons having C: H ratio 1:1. In the experimental study by Elias *et.al.*, *graphane* was seen to be stable at room temperature for many days and showed the same characteristics during repeated measurements [21]. In the same experiment, it was reported that insulating *graphane* returned to its original metallic state (graphene) upon the removal of hydrogens by annealing. Because of its high volumetric hydrogen density it is a promising candidate for hydrogen storage devices. There are few reports on the partial hydrogenation of graphene which explore many other interesting aspects of hydrogenated graphene. DFT calculations carried out by Boukhvalov [23] and Casolo

² As of now there are no experimental reports on the band gap and available theoretical values also differ.

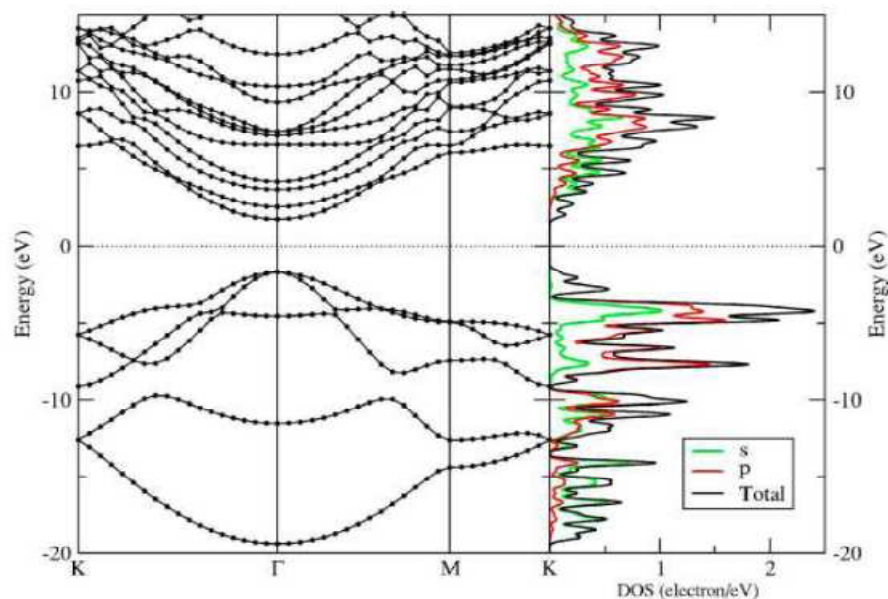


Figure 1.3 - The band structure and density of states of pure *graphane*. The band gap of 3.5 eV is seen at T point while at K point the band gap is large.

[24] show that single or double hydrogens chemisorbed on graphene sheet give rise to small magnetic states. These results also confirm that the arrangement of hydrogens which minimizes the lattice imbalance is favored. Decorating graphene lattice with triangular arrays of hydrogens is studied by Wu *et.al.* [25]. They show that each carbon triangle possesses notable magnetic moment on the edges. Further, the band gap calculation in partially hydrogenated graphene is shown to be sensitive to the edge patterns [26]. Based on these findings, the graphene quantum dots and heterojunctions have been proposed. A DFT work by Zhou and co-workers report the one sided de-hydrogenation of *graphane* resulting in an ordered ferromagnetic state [27]. For low hydrogen concentrations (upto 10%H), the calculations by Bang show that the conductance through low energy propagating channels decay exponentially with sample size [28]. Apart from the above reports, there are few recent calculations examining the effect of hydrogenation on the band gap. The surface doping and band gap tunability in hydrogenated graphene has been studied by Matis *et.al.* [29]. With photoemission spectroscopy, Haberer and group demonstrate that a tunable gap in quasi-free-standing monolayer graphene on gold can be induced by hydrogenation [30]. The size of the gap can be controlled via hydrogen addition and reaches ~ 1.0 eV for hydrogen coverage of 8%. Recently, Pujari and co-workers [31] showed that

1. Introduction

single-side-hydrogenated graphene is a semiconductor with an indirect band gap of 1.35 eV, which is in between the gapless graphene and wide band-gap *graphane*.

Although hydrogenation of graphene has been under a series of investigations, two important issues are not addressed so far. First, as of now there are no findings on the minimum energy configuration for hydrogen atoms to decorate the graphene lattice. Second, the evolution of the band gap as one goes from pure graphene to *graphane* via hydrogenation is still unexplored. These problems are examined in the present work. We have carried out DFT work to compute the electronic structure of graphene, *graphane* and partially hydrogenated graphene from 0% to 100% hydrogen. The objective of our work is to obtain the insight of the way gap opens. Additionally, we have also calculated the patterned hydrogenated graphene sheet to study the band gap modulation.

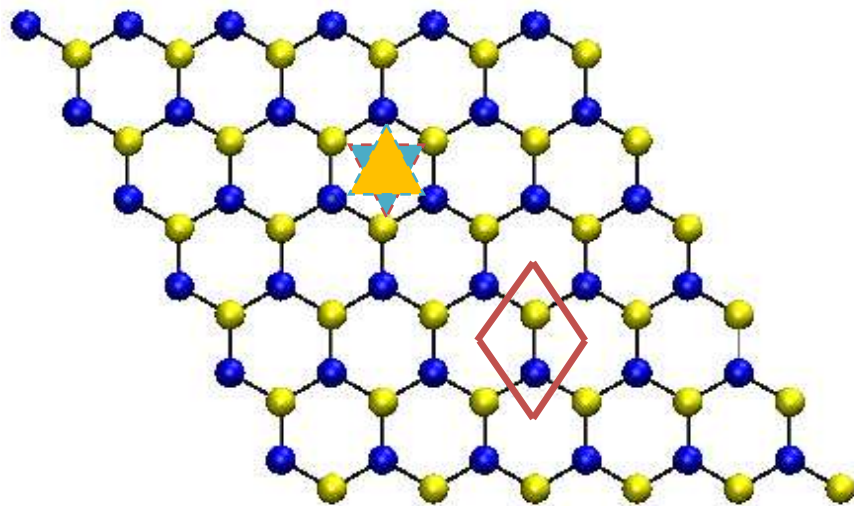
1.2.2 Lattice structure of graphene

The basic underlying structure for graphene, *graphane*, graphene nanoribbons and carbon nanotubes is two dimensional hexagonal lattice of carbon atoms. The unique properties exhibited by these materials arise from the collective behavior of electrons. In the present section, we will review some interesting features of this 2D structure.

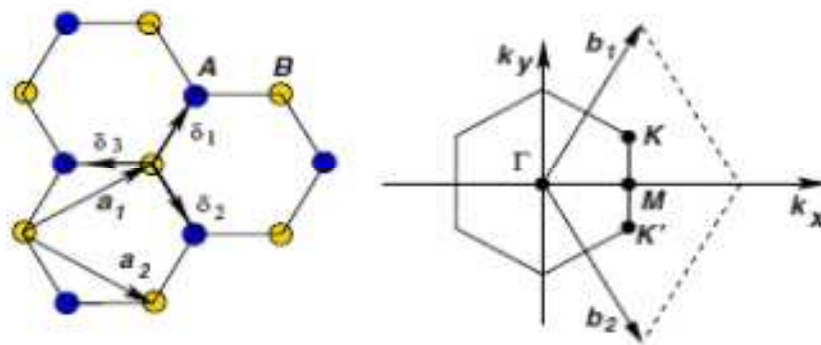
The hexagonal lattice of graphene can be considered as square Bravais lattice with two point basis. The primitive cell is denoted in figure 1.4-(a) by red square, enclosing two carbon atoms. The other commonly adopted way is to construct two triangular lattices interpenetrated with each other as shown in figure 1.4-(a) by blue and yellow triangle. Figure 1.4-(b) shows a closer view of atoms A and B belonging to the different sub lattices. The lattice vectors are given by

$$\begin{aligned}\mathbf{a}_1 &= \frac{a}{2}(3, \sqrt{3}) \\ \mathbf{a}_2 &= \frac{a}{2}(3, -\sqrt{3})\end{aligned}\tag{1.1}$$

where 'a' = 1.42Å is the carbon-carbon distance.



(a)



(b)

Figure 1.4 – (a) The Graphene honeycomb lattice with two point basis. (b) The same lattice formed with two triangular sub lattices and corresponding reciprocal lattice [32]

Using translational vector $\mathbf{R} = n_1\mathbf{a}_1 + n_2\mathbf{a}_2$, the entire hexagonal lattice is generated. The corresponding reciprocal lattice having hexagonal symmetry is shown in figure 1.4-(b), with \mathbf{b}_1 and \mathbf{b}_2 as reciprocal lattice vectors, given by

$$\mathbf{b}_1 = \frac{2\pi}{3a}(1, \sqrt{3}) \tag{1.2}$$

$$\mathbf{b}_2 = \frac{2\pi}{3a}(1, -\sqrt{3})$$

1. Introduction

The Wigner-Seitz cell of the reciprocal lattice (first Brillion zone) shown in the figure has two symmetry points K and K' which are of particular importance. These are called as Dirac points and their coordinates in reciprocal space are given by

$$K = \left(\frac{2\pi}{3a}, \frac{2\pi}{3\sqrt{3}a} \right) \quad (1.3)$$

$$K' = \left(\frac{2\pi}{3a}, -\frac{2\pi}{3\sqrt{3}a} \right)$$

The tight binding Hamiltonian for graphene considering the hopping to nearest and next-nearest neighbors is

$$H = -t \sum_{\langle i,j \rangle, \sigma} (a_{\sigma,i}^\dagger b_{\sigma,j} + \text{h.c.}) - t' \sum_{\langle\langle i,j \rangle\rangle, \sigma} (a_{\sigma,i}^\dagger a_{\sigma,j} + b_{\sigma,i}^\dagger b_{\sigma,j} + \text{h.c.}) \quad (1.4)$$

Where $a_{i,\sigma}$ ($a_{i,\sigma}^\dagger$) annihilates (creates) an electron with spin σ ($\sigma = \uparrow, \downarrow$) on site \mathbf{R}_i on sublattice A, t is the near neighbor hopping energy (hopping in different sublattice), t' is the next nearest neighbor hopping energy (hopping in the same sublattice). The energy bands derived from this Hamiltonian have the form,

$$E_{\pm}(\mathbf{k}) = \pm t \sqrt{3 + f(\mathbf{k})} - t' f(\mathbf{k}), \quad (1.5)$$

$$f(\mathbf{k}) = 2 \cos(\sqrt{3} k_y a) + 4 \cos\left(\frac{\sqrt{3}}{2} k_y a\right) \cos\left(\frac{3}{2} k_x a\right)$$

The + sign applies to upper (π) and – sign applies to lower (π^*) band. The above dispersion relation gives rise to the peculiar conical shape at Fermi energy as shown in figure 1.5. Note that the valence band and conduction band meet only at two points, K and K' (Dirac points) making graphene a zero gap semimetal.

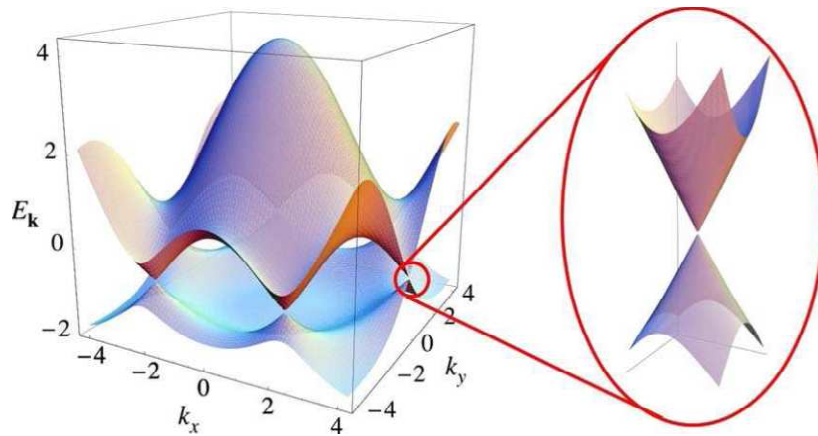


Figure 1.5 – Dispersion relation in graphene. Inset: energy bands close to Dirac points. [32]

The inset figure zooms the band structure near one of the Dirac points. Actually there are two sets of three Dirac points, two of which are inequivalent, denoted by K and K' . The upper half of the energy dispersion are anti-bonding orbitals (π^*) while lower half represents the bonding (π) orbitals. The obvious reason for the existence of this π - π^* complexity is the partially occupied p_z orbitals of the carbon atoms. The upper π^* band and lower π band are degenerate only at K point at Fermi level and the energy E in the equation 1.5 is linear with momentum \mathbf{k} , given as $E(\mathbf{k}) = \pm \hbar v |\mathbf{k}|$ [32, 33], where v is the velocity of the electron. Electrons in the neighborhood of Fermi points K and K' have a linear dispersion relation and are well-described by the Dirac equation for massless fermions. That is, the effective mass of the charge carriers in this region is zero. Since this is similar to the relativistic particle, the low energy physics in graphene is well described by Dirac equation.

1.2.3 Graphene : Synthesis and Properties

The experimental synthesis of graphene is carried out by different ways. We shall quote some of the important methods here. Graphite oxide reduction was probably historically the first method of graphene synthesis that was reported by P. Boehm in 1962 [34, 35]. In this early work existence of monolayer reduced graphene oxide flakes was demonstrated. Graphite oxide exfoliation is achieved by rapidly heating

1. Introduction

and gives highly dispersed carbon powder with some graphene flakes. Today graphene synthesis is carried out with much sophisticated ways.

1. Mechanical exfoliation - In 2004, the Manchester group led by Novoselov and Geim [17] first isolated graphene planes using adhesive tapes. The graphitic crystals are repeatedly split into thinner pieces. The tape along with the attached optically transparent flakes, is dissolved in acetone and after a few further steps, the flakes including mono layers are sedimented on a silicon wafer. Individual atomic planes of graphite are then hunted in an optical microscope. Using this technique single layer graphene flakes with dimensions of up to 10 μm could be generated. The technique is then refined and dry depositions are now used where eventually up to 1 mm graphene sheets are obtained. It is referred as Scotch tape or drawing method. However, the process is limited to small sizes and cannot be scaled for industrial production. (See figure 1.6)
2. Epitaxial growth on silicon carbide– In another method silicon carbide (SiC) is heated to high temperature ($> 1100\text{C}$) [36]. The face of the SiC used for graphene formation, silicon or carbon terminated highly influences the thickness, mobility and carrier density of the graphene. Many important properties of graphene have been identified via this method. Epitaxial graphene on SiC can be patterned using standard microelectronics methods. The possibility of large integrated electronics on SiC epitaxial graphene was first proposed in 2004, [37] and a patent for graphene-based electronics was filed provisionally in 2003 and issued in 2006. Since then, important advances have been made. In 2008, researchers at MIT Lincoln Lab produced hundreds of transistors on a single chip and in 2009, very high frequency transistors were produced at the Hughes Research Laboratories on monolayer graphene on SiC.
3. Chemical vapor deposition - In contrast to the thermal decomposition of SiC, where carbon is already present in the substrate, in chemical vapor deposition (CVD), carbon is supplied in gas form and a metal is used as both catalyst and substrate to grow the graphene layer.



Figure 1.6 – Single atom thick sheets of graphene obtained by adhesive tapes as shown in scanning electron micrographs. (Foundation of Fundamental Research on Matter, Netherlands)

There are other methods such as growth from metal carbon melts, growing graphene on metal substrate, from carbon nanotubes. The various important methods of graphene synthesis alongwith the discussion on band structure is discussed in detail in a review article ‘experimental review of graphene’ by Cooper and group [38].

We shall now turn to look at few important properties of graphene although it is simply impossible to cover all of these in details. We shall begin by noting the electronic properties first. As stated earlier, one of the most interesting aspects of graphene is its low-energy excitations are massless, Dirac fermions. This particular behavior mimics the physics of massless fermions, except for in graphene, the electrons move with the speed of Fermi velocity which is 300 times smaller than the speed of light. There are number of excellent reviews [17, 18, 39, 40] discussing the electronic structure of graphene including a well cited article by Castro Neto *et.al.* [32].

Turning towards the transport mechanism, the experimentally measured electron mobility in graphene is remarkably high [17], up to $15,000 \text{ cm}^2/\text{V.s}$ at room temperature. The quantum transport theory in graphene is elaborated in review article by Young and Kim [41]. The unique properties of graphene are highlighted by

1. Introduction

comparing the carrier transport in graphene and in two-dimensional semiconductor systems by Sarma and co-workers [42].

Graphene also shows remarkable optical properties. For example, it can be optically visible despite being only a single atom thick. The optical as well as electronic properties and their utilization in electronic and optoelectronic devices in graphene is well addressed in few reviews [43, 44]. The high electrical conductivity and high optical transparency promote graphene as a candidate for transparent conducting electrodes, required for applications in touch-screens, liquid crystal displays, organic photovoltaic cells and organic light-emitting diodes (OLEDs) [45].

Graphene is known to be the strongest material ever tested with the strength more than 200 times than steel [46]. It should thus be possible to make an almost invisible hammock out of graphene and if it was 1m^2 large it would hold approximately 4 kg heavy burden though its own weight would be less than mg. Its entire volume is exposed to the surrounding due to its 2D structure, making it very efficient to detect adsorbed molecules.

The recent review article by Balandin covers the various aspects of thermal properties of carbon based materials including graphene [47]. The thermal conductivity of graphene has also been measured with different graphene samples by various groups and is found to be in between 3080-5000 W/mK [48, 49, 50, 51] which is 10 times better than that of copper. These number are dependent on the graphene sample, that is for supported graphene and GNR these numbers are found to be smaller.

The story of graphene further continues to bring up few spectacular effects such as chirality, Klein paradox and anomalous quantum Hall Effect. The detail discussion on these is out of the scope of this work. The reader is referred to some good reviews for the details of these phenomena [17, 18, 19, 52].

In spite of all this excitement, the absence of band gap puts a limit on the use of graphene in semiconducting devices. Intense work is going on so as to retain most of the properties of graphene but still open a band gap. This leads to hydrogenation [53, 54], graphene nanoribbons, substrate doping [55, 56, 57, 58, 59], symmetry induced gap [60] etc.

We close this section by noting other 2D material, boron-nitride sheet (BN sheet) which is known to be wide gap semiconductor. It shares the same honeycomb

lattice structure as graphene. Its electronic properties can be tuned by various methods.

1.3 PURE AND HYDROGENATED GNR INSIDE CARBON NANOTUBES

Yet another promising graphene based materials are carbon nanotubes (CNT) and graphene nanoribbons (GNR). The properties of these one dimensional novel system are being analyzed extensively due to their ability to modify the band gap with various parameters like width, edge patterns and encapsulation with impurity. In this section, we shall take the review of GNR and CNT and understand the ways to functionalize CNT.

1.3.1 Graphene nanoribbons

A class of quasi one dimensional nanomaterials of recent research interest is graphene nanoribbons (GNR). These are thin, elongated strips of graphene which were first introduced as a theoretical model by Fujita and co-workers [61, 62, 63] to study the edge effects in graphene. There are two types of edge patterns observed in GNR, zigzag and armchair arising from the termination of graphene and they show very different electronic properties arising from their contrasting boundary conditions. Figure 1.7 shows the zigzag (Z-GNR) and armchair (A-GNR) with distinctly different edge patterns. Note that in zigzag GNR, the atoms at the edge belong to same sub lattice and the unit cell (shown in an enclosed rectangle) contains ‘A’ type of atoms alternating with B type. The width of Z-GNR is approximately given by $W = \frac{N}{4}\sqrt{3}a$, N being the number of atoms in unit cell and a being the lattice constant. In an armchair GNR, the edge atoms contain a dimer ‘A-B’ with width $W = \frac{N}{4}a$. The dangling σ -bonds at the edge are generally passivated by hydrogen atoms. The tight binding calculations show that Z-GNR is always metallic while A-GNR can be metallic or semiconducting. An interesting feature seen in GNR is ‘width dependant band gap’.

We shall briefly note some important work on the GNR. The first principal calculations by Louie’s group [64] confirm the occurrence of band gap in both types of GNR and is variable as the width is changed. The comparison with the tight

1. Introduction

binding calculations is also discussed in their work. The electronic states of narrow GNR are studied by Brey and Fertig using Dirac equations [65]. Their results confirm that the armchair GNR can be metallic or insulating depending on the width. A recent experiment by Kim's group demonstrates the band gap modulation by lithographic processes [66]. The defects that occur in lithographic technique are eliminated in GNR fabricated by high-temperature hydrogen annealing of unzipped carbon nanotubes. The GNR are of width ~ 100 nm and show a large intrinsic energy bandgap of ~ 50 meV [67]. There are few other techniques and methods in which the band gap modulation has been demonstrated [68, 69]. Barone *et.al.* present a DFT analysis of bare and hydrogen-terminated ribbons with different edge nature and widths up to 3 nm [70]. Their results predict that in order to produce materials with band gaps similar to Ge or InN, the width of the ribbons must be between 2 and 3 nm. If larger bang gap ribbons are needed (like Si, InP, or GaAs), their width must be reduced to 1-2 nm. There are good review articles covering the basic theoretical aspects of electronic and magnetic structure of GNR [71, 72] while few novel properties are reviewed by Dutta and Pati [73].

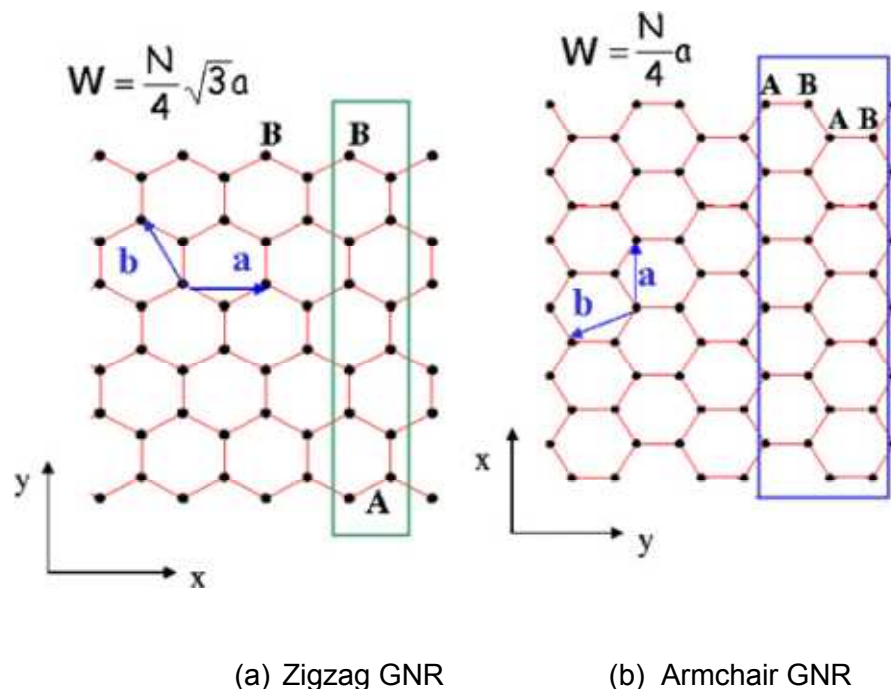


Figure 1.7 – (a) Zigzag GNR with atoms A and B alternately arranged along the edge (b) Armchair GNR with A-B dimer forming the edge pattern [71]. Note that the coordinate axis in (b) is rotated 90° , with respect to (a).

1. Introduction

The production of high quality GNR with smooth edges and well-defined widths is a crucial point in GNR synthesis. Several routes have been proposed for the same; For instance, Dai and co-workers [74] have obtained GNR by unzipping multiwalled carbon nanotubes (MWNT) by plasma etching of nanotubes partly embedded in a polymer film. In another work, Dai's group notice that few layer nanoribbons can be produced by unzipping mildly gas-phase oxidized MWNT using mechanical sonication in an organic solvent [75]. The GNR so obtained have smooth edges and a narrow width distribution. Tour and co-workers synthesized GNR by lengthwise cutting of MWCNT by a simple, efficient, and scalable oxidation method [76]. Figure 1.8 shows a pictorial representation of few of the methods for GNR synthesis employed using CNT.

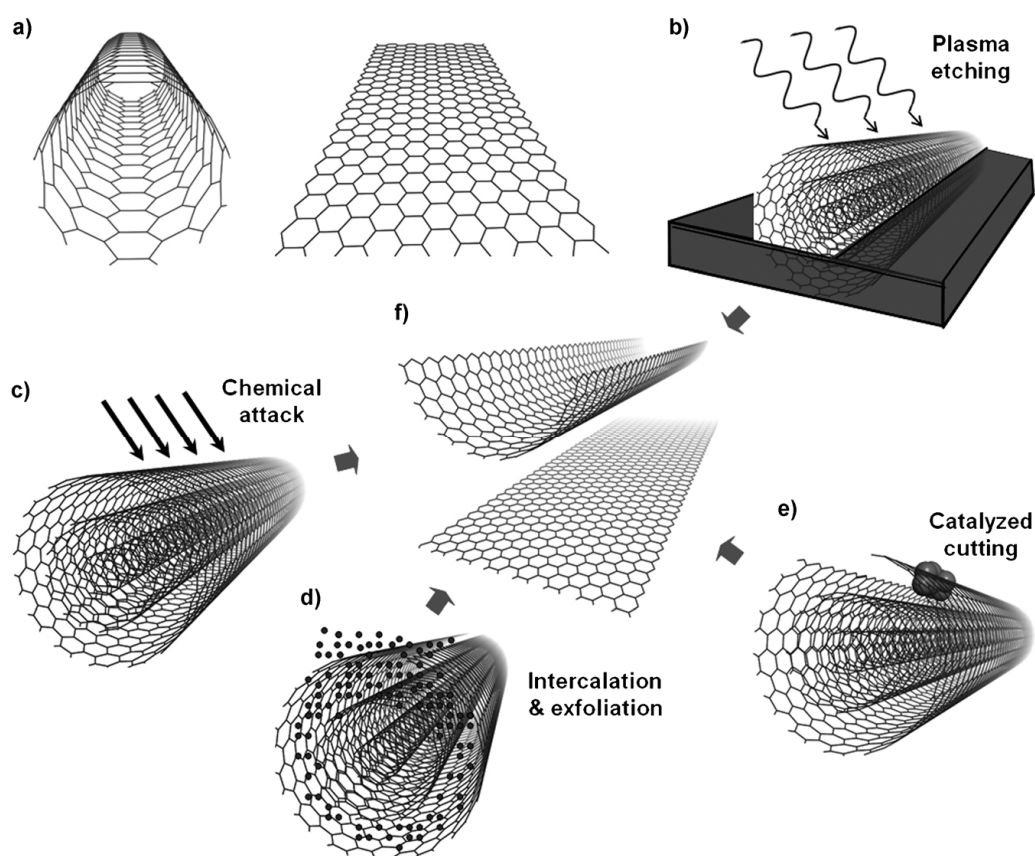


Figure 1.8 – (a) SWNT and GNR (b) plasma etching of partially embedded CNT (c) longitudinal cutting of CNT by chemical attack (d) intercalation of alkali metal atoms followed by exfoliation of CNT and (e) metal particle catalyzed cutting of CNT (f) Final GNR [77].

1. Introduction

Next, the lithographic techniques are commonly used to produce GNR with controlled edge orientations [66, 78]. Cai *et.al.* demonstrate the fabrication of GNR by surface assisted coupling of molecular precursors [79]. The topology, width and edge periphery of the GNR are defined by the structure of the precursor monomers. There are number of methods investigated using the chemically fabricated GNR through various methods [80, 81, 82, 83, 84, 85, 86, 87]. The termination of GNR with oxygen, carbon dioxide, water and ammonia is carried out in a DFT work by Seitsonen and group [88]. Their results predict that neutral GNR in oxygen-rich atmosphere should preferentially be along the armchair direction while water-saturated GNR should present zigzag edges. GNR are also produced by cutting graphene sheet [89, 90]. A very recent fabrication technique for graphene nanoribbons (GNR) employs copper oxide nanowires as the etch masks [91]. The various methods of GNR synthesis with advantages and disadvantages are addressed in a mini review by Ma and co-workers [77].

One of the simple ways to obtain the stable GNR is encapsulation inside carbon nanotubes. Recently, two experimental groups by Talyzin *et.al.* [12] and Chuvilin *et.al.* [92] have independently demonstrated the formation of such stable structures. Talyzin and co-workers [12] propose an experimental technique for the synthesis of H-terminated GNR inside SWNT using thermally induced fusion of coronene and perylene molecules. Carbon nanotubes in this reaction provide one-dimensional alignment of molecules required for the fusion reaction into graphene nanoribbons. The other work by Chuvilin *et.al.* demonstrates that GNR can be self-assembled from a random mixture of molecular precursors within a single-walled carbon nanotube. The sulphur terminated GNR are otherwise unstable in free state.

Motivated from these recent findings, we employ the DFT study of pure as well as hydrogenated GNR inside CNT. We wish to examine the effect of confinement on the geometry of pure GNR and H-GNR as a function of CNT radii. Our results suggest that the encapsulated structures are sensitive to the placement and concentration of hydrogen in GNR.

1.3.2 Carbon nanotubes

CNT are ‘graphene sheets seamlessly wrapped’ to form cylindrical one dimensional tube. They have typical diameters in nanometer range and can extend up to few millimeters long. They were first synthesized by Iijima [93] in 1991. These tubular nanostructures are metallic or semiconducting and have wide applications in the field of nanotechnology, electronics and optics. There are mainly two types of CNT – single walled carbon nanotubes (SWNT) and multiwalled carbon nanotubes (MWNT). SWNT are formed by rolling a single graphene sheet into a cylinder while MWNT have more than one SWNT arranged like concentric rings. The open ends of CNT are normally passivated by hydrogen atoms. The original carbon nanotubes produced in 1991 were in fact MWNT having outer diameter range of 4-30 nm and length up to 1 μm [93]. A schematic picture shown in figure 1.9 represents the way graphene sheet is rolled to form a CNT. Imagine the graphene sheet to be cut along a dotted line indicated by ‘T, tube axes. The armchair line is drawn such that it cuts each hexagon into 2 halves.

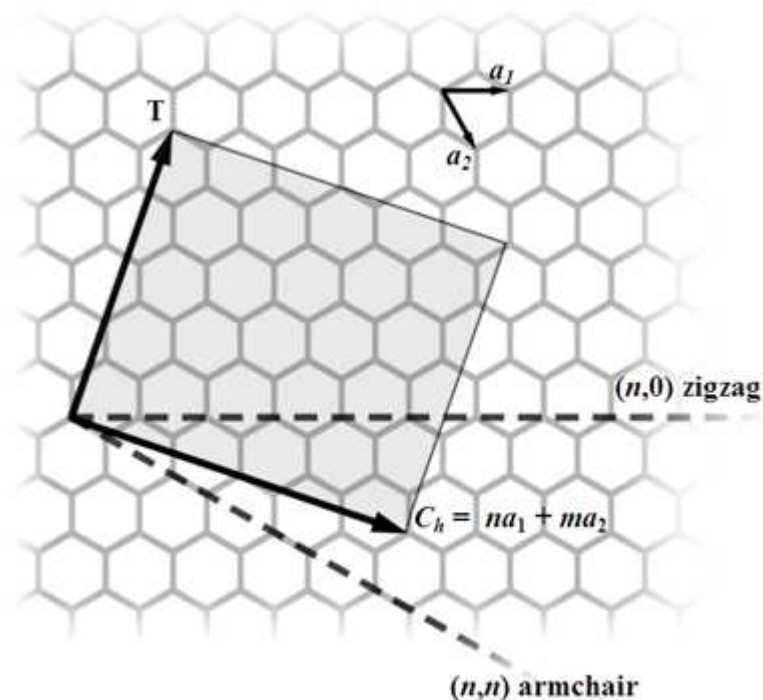


Figure 1.9 – A representation of graphene sheet rolled to form a carbon nanotube. The chirality vector, zigzag and armchair vectors are shown. (Image courtesy: <http://www.wikipedia.org>)

1. Introduction

C_h represents the chiral vector given by $C_h = n\mathbf{a}_1 + m\mathbf{a}_2$, where \mathbf{a}_1 and \mathbf{a}_2 are unit vectors of graphene, the angle φ between C_h and armchair line determines the way sheet is rolled to form a tube. If $0 < \varphi < 30^\circ$, then CNT is called chiral. The values of n and m determine the chirality or twist which in turn affects the conductivity of nanotubes. For $m=0$, all the nanotubes are of 'zigzag' type. If $n=m$, then the nanotubes are called as 'armchair'. For all the other values of n and m , the tubes are called as 'chiral'. The following simple rule determines the conducting nature of the CNT.

$$\text{If } \frac{n-m}{3} = \text{integer, then the CNT is metallic}$$
$$\neq \text{integer, then CNT is semiconducting.}$$

All armchair tubes are metallic. Theoretically, metallic nanotubes can carry an electric current density of $4 \times 10^9 \text{ A/cm}^2$, which is 1,000 times greater than that of metals such as copper. The three types of nanotubes discussed above are shown in figure 1.10. Their names are consistent with the pattern formed along their edge. The diameter of CNT is dependent of the values of n , m and the lattice constant of graphene. It is calculated as:

$$d = \frac{a}{\pi} \sqrt{n^2 + m^2 + nm}$$

where a is the lattice constant of graphene = 2.46 \AA .

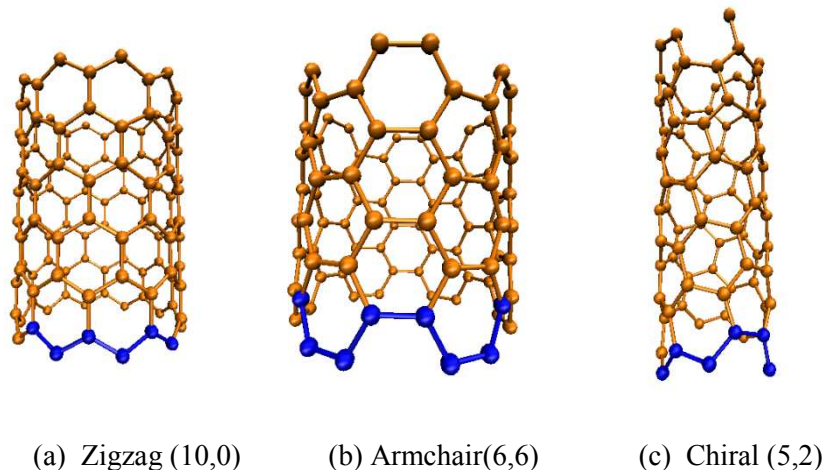


Figure 1.10 - Three types of carbon nanotubes formed by the way the graphene sheet is rolled. The numbers in the bracket indicate n, m parameters.

1. Introduction

Theoretical calculations show that the electronic properties of the CNT are very sensitive to their geometric structure [94]. Although graphene is a zero-gap semimetal, CNT can be metallic or semiconducting with varying energy gaps, depending on the diameter and helicity of the tubes, i.e. on the indices (n,m) . The physics behind such sensitive nature can be understood within a band-folding picture. We know that the electronic structure of graphene near the Fermi energy is given by an occupied π band and an empty π^* band. These two bands meet at 'K' point as shown in figure 1.11-(a). When forming a tube, owing to the periodic boundary conditions imposed in the circumferential direction, only a certain set of \mathbf{k} states of the planar graphene sheet are allowed. The set of allowed \mathbf{k} values indicated by the lines in figure 1.11-(b) depend upon the diameter and helicity. When the point 'K' is not included, the system is a semiconductor with different sized energy gaps. CNT has a finite circumference C which quantizes the momentum around the tube. It is conducting if the quantized momentum matches a Dirac point.

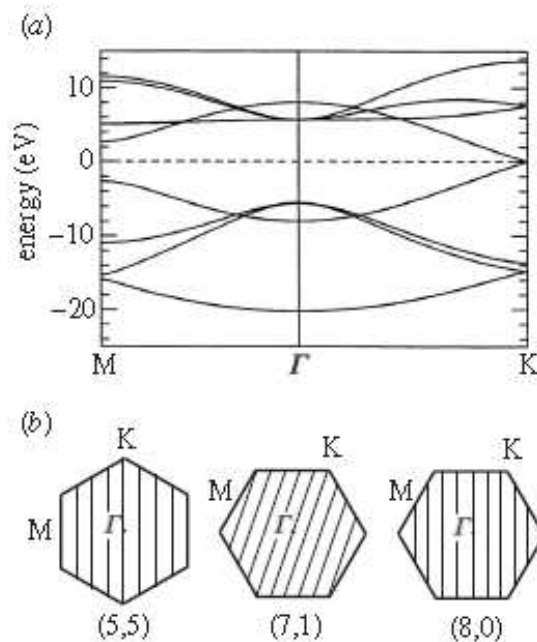


Figure 1.11 – (a) Band structure of graphene showing main high symmetry points (b) Allowed \mathbf{k} vectors of CNT mapped onto graphene Brillouin zone. [95]

CNT Synthesis

The various methods of CNT synthesis include arc discharge, laser ablation, chemical vapor deposition (CVD) or high pressure carbon monoxide (HiPCO). The nanotubes were first observed in 1991 [93] in the carbon soot of graphite electrodes during an arc discharge, by using a current of 100 amperes. During this process, the carbon contained at the negative electrode sublimates because of the high discharge temperature. In the laser ablation process, a pulsed laser vaporizes a graphite target in a high temperature reactor while an inert gas is bled into the chamber. Nanotubes are developed on the cooler surface of the reactor as the vaporized carbon condenses. A water-cooled surface may be included in the system to collect the nanotubes. The laser ablation method yields around 70% and produces primarily single walled carbon nanotubes with a controllable diameter determined by the reaction temperature. However, it is more expensive than either arc discharge or chemical vapor deposition. CVD synthesis is done by putting a carbon source in the gas phase and using an energy source, such as plasma or a resistively heated coil, to transfer energy to a gaseous carbon molecule. Commonly used gaseous carbon sources include methane, carbon monoxide and acetylene. CVD is the most convenient method, in terms of purity as well as commercial production.

SWNT and MWNT possess a wide range of applications based on the remarkably different properties they exhibit. The electron transport in metallic CNT occurs without any scattering over long tube lengths which enable them to carry high currents [96]. These are known to be the excellent conductors of heat, with thermal conductivity more than that of isotropically pure diamond. SWNT are quite stiff, exceptionally strong with Young's modulus 1000GPa and high tensile strength. A single wall nanotube can be up to 100 times stronger than that of steel with the same weight. Such high strength emerges from the sp^2 bonding of the carbon atoms. A reader can refer to number of reviews [95, 97, 98, 99, 100, 101, 102] for the various properties and applications of CNT. Although, SWNT are quite expensive to synthesize and manufacture in terms of purity, they can easily interact with different atoms, molecules and chemicals groups. This property is useful to create a new set of nanomaterials with modified properties. The next section deals with such functionalization of CNT.

1.3.3 Functionalization of carbon nanotubes

One of the various ways to modulate the properties of CNT for the application purpose is the ‘functionalization of CNT’. Functionalization is modifying the properties of CNT by some external molecular fragments attached either covalently or by non-covalent way. It is also possible to insert the atomic species, molecules or clusters inside the CNT or wrapping various functional groups around it. Here, we shall take the review of some experimental and theoretical work related to different types of functionalization and their applications.

CNT have been functionalized widely for the hydrogen storage purpose. A first principal calculation by O. Gülseren and co-workers [103] shows that the electronic and atomic structure of carbon nanotubes undergoes dramatic changes with hydrogen chemisorptions. It was experimentally demonstrated that the maximum degree of hydrogenation of CNT depends on the diameter. CNT with the diameters around 2nm yield almost 100% hydrogenation [104]. Calcium decorated nanotubes, pure and with defects can also be used for the hydrogen storage [105]. First principal calculations by Yildirim and Ciraci report titanium decorated CNT can adsorb upto 8% hydrogen [106]. The study was generalized further to investigate hydrogen storage by light transition metals [107]. CNT are also doped with light metals in the interior channel which enhances the binding strength of atomic hydrogen [108]. The hydrogenated nanotubes are found to be stable upto 400 °C [109].

Apart from the hydrogen storage CNT are also experimented and used for various other purposes. The tetra and hexa vacancies in metallic CNT trigger the transport properties [110]. Liang *et.al.* [111] dissolved SWNT, lithium and alkyl halides in liquid ammonia, yielding sidewall functionalized nanotubes. A recent interesting work by J. Guo demonstrates the sulfur impregnated disordered carbon nanotubes synthesized as cathode material in lithium-sulphur battery [112]. CNT based electrodes are possible due to their high surface to mass ratio and good conductivity. Few other research works also bring up the use of CNT as electrodes for lithium ion batteries [113, 114]. Lately the noncovalent interaction between the CNT and the biomolecules, like DNA, has been the subject of immense interest. There are reports [115, 116, 117] in which the DNA assisted dispersion and separation of

1. Introduction

carbon nanotubes is studied. The DNA can bind the π stacking of CNT resulting in helical wrapping of CNT as shown in figure 1.12.

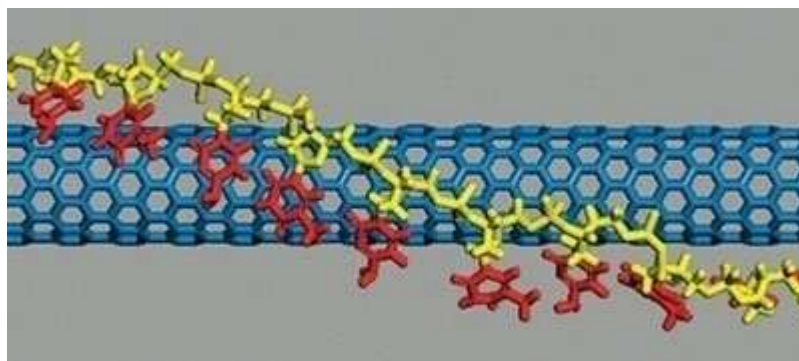


Figure 1.12 – DNA wrapped CNT (Image courtesy - A. Jagota)

A work by Y. Liu and co-workers demonstrates that CNT coated with alginic acid functionalization can overcome the solubility issue of the tubes [118]. Aromatic organic molecules and conjugated polymers can interact with the surface of CNT to give low contact resistance when CNT are used as the electrodes in organic field effect transistors [119]. The development of glucose biosensors based on carbon nanotube-nanoelectrode ensembles for the selective detection of glucose has been studied [120]. Many studies are dedicated to use of CNT in electronics. These have potential applications in nanoscale transistors and sensors. SWNT are used in the development of the first intermolecular field effect transistors (FET) [121, 122] and first nanotube based logic gates using [123].

The unique tubular morphology of nanotube provides a well defined, hollow space for inserting the atoms and molecules inside it. Due to the confinement, the size of the particles inserted is restricted to nanometer scale. There is also a possibility to develop the bonding interactions between carbon atoms and guest atoms. Among a variety of materials used to fill inside CNT, fullerenes [124, 125], linear chains, liquids and biomolecules are of prominent interest. Encapsulation of CNT with various atomic species has been vastly studied [126, 127, 128, 129, 130, 131]. The encapsulation of Fe_4 cluster in CNT shows a change in geometry from D_{2d} to a low-symmetry tetrahedral or a planar chain structure depending on the diameter of CNT. The strong Fe-C sp hybridization suppresses the sp spin polarization of Fe atoms [132]. The structure and electronic structure of Fe_3C in SWNT has been indicated to

1. Introduction

be useful in spintronics studies [133]. The reactivity of CNT has been studied by lithium doping [134]. Lithium has been an active reagent to improve the solubility and reactivity of nanotubes. The other ingredient which is extensively used for endohedral functionalization is water [135, 136]. The formation of ordered polygonal ‘ice-nanotubes’ are predicted by MD simulations [137]. An interesting MD study by G. Zhuo *et al.* shows the confined water chains inside carbon nanotubes can self adjust into regular oscillations with lower entropy [138].

Substantial amount of work has been done experimentally as well as theoretically on the encapsulation of carbon species. In an experiment with the C_{60} molecule inside the nanotube [139], it was found that iodine atoms can be doped at the intratubular positions in the C_{60} peapods and when the system is heated to $550\text{ }^{\circ}\text{C}$ the C_{60} are transformed into a tubular structure. The stability of number of carbon structures such as carbon chains, rings, graphitic sheets and cages inside CNT has been studied using DFT calculations by Y. Lui and co-workers [140]. Their work showed that CNT with diameters larger than 1.0 nm can incorporate rings, graphitic sheets, smaller nanotubes, or cages. Species with dangling bonds can interact with the CNT wall or form other stable structures, depending on the distance from the CNT wall. The MWNT also have been experimentally used to stabilize the long wires of carbons [141]. The encapsulation of carbon species in SWNT and MWNT has been reported with various techniques [142, 143, 144, 145, 146]. To summarize, nanotubes can be very useful to examine the confinement effects as well as to form the stable nanostructures which are otherwise difficult in free space. For detail reviews the reader is advised to go through the articles related to CNT [147, 148, 149, 150, 151, 152]. The focus of our work is to monitor the effect of confinement on the geometry of GNR through encapsulation by CNT.

After nanoribbons the next fascinating problem we will investigate is ‘thermodynamics of clusters’.

1.4 THERMODYNAMICS OF SMALL CLUSTERS

Atomic clusters are considered as the building blocks of nanomaterials. As a thumb rule, any system with 3 to 10^{23} atoms is considered as a ‘cluster’. These form a special class of materials in which the limited size leads to unusual combinations of physical and chemical properties. These are the prototypes for understanding the nanosystems.

1. Introduction

Clusters have been extensively studied for last thirty years for analyzing the ground state geometry, binding energy, HOMO-LUMO gaps, magnetism, thermal properties etc. A great deal of work has been reported on homogeneous clusters to understand the ground state properties. Lately, few experimental works on the impurity doped clusters seek the attention of the researchers. Apart from the ground state properties, the finite temperature properties of clusters are equally fascinating. In this section, we give a brief review of the properties of clusters, followed by the reviews on thermodynamics of pure and doped clusters. For the sake of completeness we shall briefly describe the experimental methods for melting of small clusters towards the end.

1.4.1 Introduction to clusters

One of the most significant findings about the clusters is the existence of the ‘magic numbered clusters’. These were first reported experimentally by Knight [153] for sodium clusters. It was found that the clusters with the number of valence electrons 8, 20, 40, 58,.... are abundant and stable and were called as magic clusters. Later, such stability was also reported for aluminum clusters [154, 155]. The abundance and stability of these magic clusters is well explained by electronic shell closing under jellium model, which is still used in understanding the metallic clusters. However for more detail understanding, sophisticated techniques such as density functional theory are used. In the spherical jellium model we assume that electrons move in a uniform background of positive charge, where they are subjected to an external potential. The solution of the single electron Schrödinger equation for the spherical well gives a series of magic numbers: 2, 8, 18, 20, 34, 40, 58,,..... and leads to 1s, 1p, 1d, 2s... electronic shells similar to the shell model of nuclei. (figure 1.13) Such clusters particularly can be used as building blocks to generate the cluster assembled materials as suggested by Khanna and Jena [11].

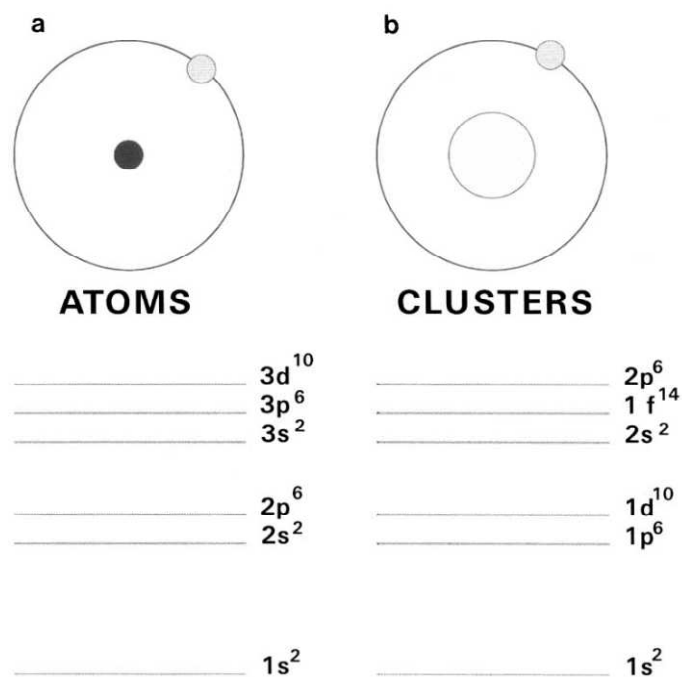


Figure 1.13 – A comparative picture of the shell closure in an atom and a cluster. [156]

Often the clusters are categorized on the basis of nature of bonding. It is also noted that the geometries of the clusters depend on the bonding type. For example, clusters of free electron metals and alkali metals like Na normally adopt an electronic shell structure [157]. Approximation such as the jellium model describes large number of alkali metal properties quite well. Typically, simple metallic clusters possess s-p type of bonding orbitals while transition metals like Au, Ag have d-electrons participating in the bonding. On the other hand clusters of group IV show prolate shapes in the evolution due to the covalent bonding. Structural transition towards prolate shapes has been demonstrated experimentally in small clusters of Si [158, 159], Ge [160] and Sn [161]. The clusters of gas molecules like argon and neon are bonded by Van-der-Walls forces. Oxides clusters such as MgO belong to class of ionic clusters and are held together by strong forces of attraction between oppositely charged ions. Carbon shows surprisingly different geometries and shapes ranging from 0D clusters, linear chains, polycyclic rings and 3D graphite. The discovery of stable caged fullerene C₆₀ by Kroto *et.al.* [162] is one of the important discoveries in the cluster physics.

The properties of clusters are different from their bulk not only in terms of geometry but in many aspects. For example, bulk sodium is bcc while small clusters of sodium in range of few 100 atoms show ample variation in the geometry, Na₅₅

1. Introduction

being the icosahedral structure. The photoelectron spectroscopy of size-selected aluminum (neutral and negative) clusters with size range 1 to 162 confirms the shell closing property [163]. Another notable example is of gold clusters which are quite reactive compared to the noble gold in bulk. They show a transition from 2D to 3D at $n=7$ [164, 165, 166]. There are reports on the magnetic clusters such as that of Rn and Pa [167]. Magnetism in clusters itself is very interesting subject. Advances in the experimental techniques as well as tremendous growth in the computational power made it feasible to study the clusters from magic numbered to superatoms with great details. The properties of clusters are well discussed in many useful reviews and books as well as large number of research papers [4, 6, 9, 168, 169].

1.4.2 Thermodynamics

There are large number of reports focusing on the ground state properties of various types of clusters but the ‘thermodynamics’ is still much less probed. Unlike bulk, in case of clusters, the specific heat curves are typically broad and range over few degrees of temperature. The small clusters co-exist in solid-liquid phase within this temperature range. Many times they show premelting features like a small peak or a shoulder in addition to the main peak. These premelting features are due to different processes such as isomerization or surface melting. The finite temperature properties of clusters are well discussed in number of review articles [156, 170, 171, 172, 173] and papers [174, 175].

There are some notable findings, few from our own group, which bring out many interesting aspects of the ‘melting’ behavior in clusters. Based on these earlier reports, it is known that the shape of the heat capacity curve depends on number of factors such as the size, ground state geometry, symmetry, defects or impurity in the clusters. Still, the existing data is insufficient to predict the melting behavior of the given system.

Normally, most of the clusters show the depression in the melting temperature compared to the bulk. This is caused by the fact that the fraction of surface atoms is large in the cluster. Surface atoms have fewer neighbors; therefore, they are loosely bound and their thermal motion is less restricted than in bulk matter. However an interesting experimental observation for the gallium clusters namely, ‘higher than

1. Introduction

bulk melting' was noted by Jarrold's group [176]. The gallium clusters of size 17, 39 and 40 atoms show melting temperature well above the bulk gallium (303 K). The experimental work by the same group brought out the extreme size sensitivity in the nature of the heat capacity for gallium clusters in the size range of 30–55 atoms [177] which was confirmed by DFT calculations by S. Chacko *et.al.* [178]. This behavior was attributed to the covalent bonding in contrast to covalent-metallic bonding in bulk. The Sn clusters in range of 10 to 30 atoms were also found to remain stable at temperatures higher than bulk melting [179]. This was explained by the covalent bonding and very stable tricapped trigonal prism unit of Sn₁₀ within a DFT work by Joshi *et al.* [180]. In series of experimental and simulated work by Haberland and co-workers the size sensitive melting in case of the sodium clusters in size 55 to 300 is rigorously studied [175, 181, 182, 183, 184, 185]. Such irregular variation observed in these clusters was a puzzle and many attempts were made to understand this on basis of *ab-initio* simulations. Few DFT calculations from our own group on the sodium clusters [186, 187] reveal number of interesting features. The clusters in size range of 8-55 show irregular melting temperatures. Na₅₈ being a closed shell shows the highest melting temperature. These results also reveal that there is a strong correlation between the ground state geometry and the finite temperature behavior of the cluster. The ground state geometry plays a significant role in determining the shape of the specific heat curve. The ordered ground state yields a higher melting temperature. These findings have been confirmed by various other groups also [188, 189]. The experimentally observed heat capacities for Na₅₅, Na₉₂ and Na₁₄₂ clusters (by Haberland group) [181] are understood with DFT calculations by S. Chacko *et.al.* [190]. Their results reveal the interplay between geometric electronic shell effects. A similar size sensitive feature is detected in the experimental work by Breaux *et.al.* [191] on aluminum clusters. Their results are shown in figure 1.14. The figure clearly brings out the size sensitive nature where an addition of a single atom significantly changes the melting temperature as well as the nature of the heat capacity curve. The few MD simulations from our group [192, 193] involve thermodynamics of Ga⁺₁₇, Ga⁺₁₉ and Ga₃₀ and Ga₃₁ clusters. The melting behavior for Ga₃₀ and Ga₃₁ is shown in figure 1.15 where the addition of single gallium atom in Ga₃₀, changes the specific heat curve dramatically. To conclude, clusters show ample variation in the specific heat curves which is dependent on any factors.

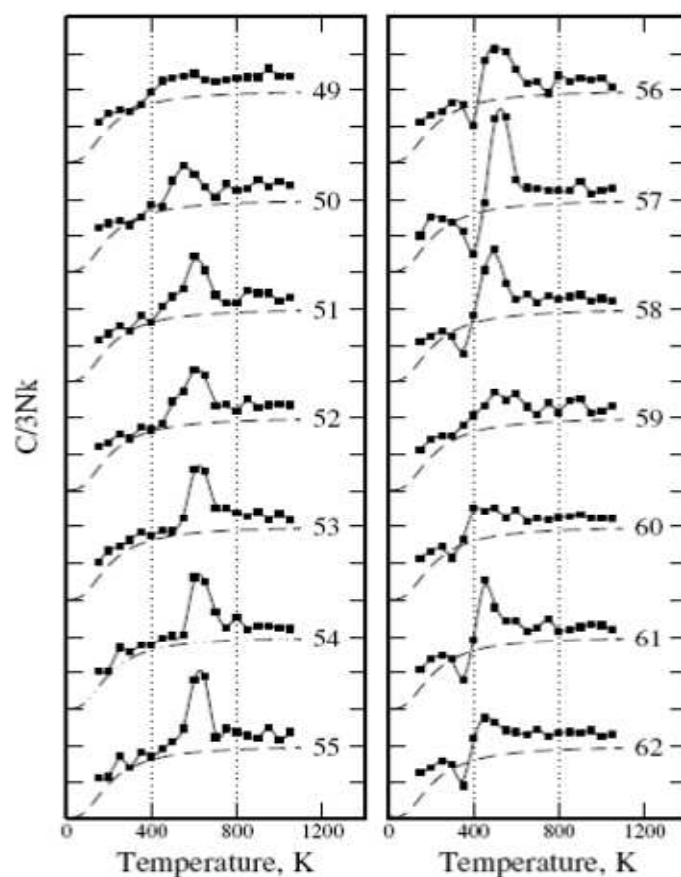


Figure 1.14 - Heat capacity curves for Al_n^+ ($n=49$ to 62) clusters [191]. The points are the experimental measurements, and the dashed lines are calculated heat capacities derived using a modified Debye.

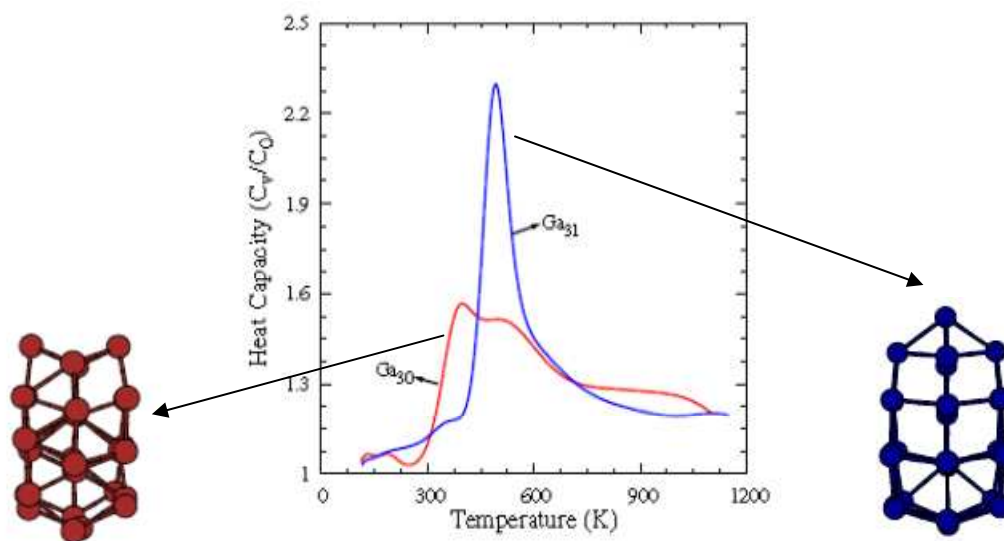


Figure 1.15 - The Ga_{30} and Ga_{31} clusters - geometry and heat capacity curves [193].

In last few years, the atomic gold shows structural dependence on the number of atoms. The geometry and binding energies of small gold clusters have been studied by number of groups [194, 195, 196, 197]. 20 atom cluster of gold possesses an ordered tetrahedral geometry and high stability amongst the other small gold clusters [198]. S. Krishnamurty and co-workers demonstrated that this Au_{20} shows a sharp melting peak while a removal of one vertex atom causes Au_{19} cluster to melt over a broad range of temperature [199]. The first hollow golden cages for Au_n^- ($n=16$ to 18) were detected experimentally and theoretically by S. Busula *et.al.* [166]. Further a DFT work for 15 to 19 atoms gold clusters by the same author reports a transition from flat to hollow cages occurring at Au_{17} . The gold cages have been observed even for $n=72$, termed as gold fullerene [200]. Such cages have potential applications in encapsulating an atom, molecule and are known to be used in the ‘targeted drug delivery’. In a joint experimental-theoretical study by Wang’s group the gold cages are doped with group IV atoms with dopants Si, Ge, Sn [201]. It was shown that the nature of the local interactions between Au and dopant atom is a critical factor in determining whether an impurity atom can be used to dope inside the golden cages. The hollow and space filling medium sized Au clusters are analyzed by Jellinek’s group [202]. A hollow cage configuration of Au_{50} is more stable than its alternative space-filling isomeric forms.

To the best of our knowledge, the stability of these cages at high temperature is not explored. In the present work, we have carried out the thermodynamics for the smallest gold cages, Au_{16} and Au_{17} cages along with the isomer distribution analysis.

At the end of this section we would like to note few important terminologies about the ‘phase change’ in clusters. Normally, the melting in bulk is characterized by a sharp peak in specific heat curve. In finite sized systems, it is well known that there is no definite phase transition. We will continue to use the terminology ‘melting’ in a broad sense and it indicates the phase change from solid-like to liquid-like.

1.4.3 Effect of doping

Doping in the bulk is a common practice used to modify the relevant property. Commonly used steel is obtained by doping iron with appropriate amount of carbon. Bronze is another alloy which is formed by doping copper with tin or zinc. In case of

1. Introduction

clusters also, the addition of impurity atom or atoms sometimes change the melting behavior significantly. The properties of the doped clusters are dependent on electronegativity, nature of bonding, ionic radii and many other factors. There is indeed extensive work on different clusters doped with various impurities exploring geometry, bonding and finite temperature properties [203, 204, 205, 206, 207, 208, 209, 210, 211]. A DFT calculation by Lee *et.al* demonstrated that Li_{10} when doped with two aluminum atoms results in a substantial structural change, triggers surface melting while the addition of one aluminum impurity causes a rearrangement of atoms [212]. Li_7 doped with single Si impurity are studied by Joshi and Kanhere [213]. Their results show that the doped cluster melts earlier than the host lithium cluster. The same group has also studied Li_nSn , ($1 < n < 9$) clusters and their results bring out the change in the nature of bonding from ionic to delocalized metallic like, after $n=6$ [214]. It is shown that the Ti impurity suppresses the fragmentation of Si_{16} cluster and melts at higher temperature [215]. The magnetic properties in transition-metal-doped gold clusters are studied by X.Li. *et.al.* using photoelectron spectroscopy and DFT [216]. The caged cluster of Au_{16} is doped with Ag, Zn and In to show that electronic properties of golden buckyballs can be tuned by doping [217]. In another work, Au_{16} is doped with Fe, Co and Ni and the $4s$ electrons are observed to transfer to Au_{16} cage, whereas atomic-like magnetism due to the unpaired $3d$ electrons is retained for all the doped clusters [218]. A recent result on titanium doped nickel clusters TiNi_n ($n=1-12$) [219] show that Ti brings substantial structural reconstruction from 3D to layer one. There are few more reports on gold clusters doped with different impurities [220, 221, 222].

The 13 atom aluminum cluster which is one electron short for the shell closure when doped with different tetravalent impurities leads to significant changes in BE, geometry, bonding and stability [223, 224, 225, 226]. It is found that the most stable dopant turns out to be carbon atom. The carbon occupies the central position in an icosahedral geometry of Al_{13} . *Ab-initio* simulations by A. Seitsonen [227] report the finite temperature studies on Al_{12}C but using only single temperature. Moreover, Al_{13} and Ga_{13} both are isoelectronic, that is having same number of valence electrons, but different ground state geometries. After substituting with a single carbon, both the doped systems become 40 atom closed shell with enhanced stability. Therefore there were few unresolved issues at time of beginning of this work such as the effect of

1. Introduction

carbon doping on the melting of both these clusters in terms of the change in C_v , bonding and geometry. In order to resolve these issues we have carried out extensive *ab-initio* thermodynamics of the pure and carbon doped Al_{13} and Ga_{13} clusters.

It is gratifying that activities in clusters physics are still being carried out for probing variety of different properties. The experimental melting transition of finite two-dimensional dust clusters in dusty plasma is analyzed using the method of instantaneous normal modes [228]. The full vibrational spectrum of Ni_n and Cu_n clusters with n from 2 to 150 has been determined. The obtained heat capacity shows clear cluster-size effects [229]. In a theoretical investigation using global optimization and path-integral simulation, melting and freezing of fullerene doped helium clusters is investigated. Up to 32 atoms, the fullerene ion traps the helium atoms on the faces above which the geometric frustration takes over and the clusters grow as a thin but homogeneous liquid layer. As their size reaches 60 atoms, corrugation barriers are suppressed and the cluster is again rigid like [230]. The structure and stability of Au_n clusters (where $n = 1, 5, 6, 19$ and 39) supported on the perfect and defective graphene sheets were investigated using a periodic DFT model by Paulo *et.al.* [231]. They observed stronger interaction between a gold atom and the graphene sheet with a defective structure. In another DFT work the equilibrium geometries, stabilities and electronic properties of the bimetallic M_2 -doped Au_n ($\text{M} = \text{Ag}, \text{Cu}; n = 1-10$) clusters are studied using effective core potentials [232]. Gao *et.al.* performed comprehensive *ab-initio* study of catalytic activities on sub nanometer gold clusters particularly in the size range of 16 to 35 using CO oxidation as a chemical probe [233]. Their calculations support the notion that CO and O_2 adsorption energies on the gold clusters can be an effective indicator to assess catalytic activities of sub nanometer gold clusters.

1.4.4 Experimental Methods

The early work in the finite temperature of clusters was initiated by the experiments. With the development in the computer technology, it was possible to simulate the problems thereby reducing the time and efforts. The primary motivation of the simulations comes from the fact that they have predictive power. Also, one can directly compare the results of the simulations with the experimental data. Here we

1. Introduction

briefly go through important experimental methods used in calculating the melting of clusters. Most of the methods are based on measuring the heat capacity as a function of temperature.

The overall procedure follows the generation of size-selective clusters, which is done by mass spectrometer. The cluster ions are thermalized by passing them through a temperature regulated region containing a buffer gas. Collisions with the buffer gas bring the clusters to the temperature of the walls. Once thermalized, they are in a canonical ensemble. They are then removed to a high vacuum environment, where they are mass selected and then probed to determine their internal energy content.

In the method by Haberland and collaborators, [175, 181] the mass selected cluster ions at temperature T_1 are irradiated with photon of energy $h\nu$. They undergo multiphoton absorption, and subsequently dissociate. This approach has been applied mainly to study sodium clusters. The dissociation energies of the sodium clusters are around 1 eV, three to four times smaller than the photon energy. In the multiphoton absorption step, enough energy is absorbed to reach the dissociation threshold, and then every additional photon leads to the loss of an extra three to four sodium atoms. Thus the fragmented ion mass spectrum shows oscillations with peaks separated by three to four atoms. If more energy is added to the dissociating clusters, either by raising their initial temperature or by changing the photon energy, the peaks in the fragmented mass spectrum shift toward smaller product ions. The heat capacity is deduced by tracking the shift in the fragmented mass spectrum as the initial temperature is changed. A drawback of this approach is that the photon energy needs to be much larger than the cluster dissociation energy (which so far has limited this method to weakly bound clusters).

The method of Jarrold and collaborators [176, 234] uses multicollision induced dissociation. The method is carried out as follows: The clusters are dissociated by shooting them into a high pressure helium buffer gas where they are heated by collisions until their kinetic energy is thermalized. The fraction of the ions' initial kinetic energy that is converted into internal energy is small. By using mass spectrometry, it is possible to determine the number of atoms present in the cluster and ensure that the cluster is not contaminated. The cluster ions are size selected with the spectrometer and then focused into the collision cell which contains helium buffer

1. Introduction

gas at a pressure 1.00 Torr. As the ions enter the cell they undergo numerous collisions with the helium buffer gas, and may be heated to the point where they dissociate. Undissociated ions and fragment ions travel across the collision cell under the influence of a weak electric field and then exit through a small aperture. They are subsequently focused into another spectrometer where they are mass analyzed and then detected. Ion mobility measurement [235] is another technique in which the rapidly traveling ions through an inert buffer gas under the influence of a weak electric field, provides a measure of the average collision cross section of the ion. The collision cross section is geometry dependant so the change in the geometry of the clusters which occurs due to phase transition is detected.

1.5 ORGANIZATION OF THESIS

The chapters in the thesis are organized as follows.

Chapter 2: In this chapter we describe the theoretical and computational techniques that are used in the thesis. The chapter begins with the concepts of many body theory and some early techniques to solve it. Next, we discuss the Density Functional Theory (DFT) followed by pseudopotential formalism with plane wave basis set. The Molecular Dynamics (MD) technique to extract the ionic trajectories is discussed thereafter. At the end along with the data analysis tools, we also give the description of the traditional ‘melting’ indicators. We close the chapter with the error analysis.

Chapter 3: After discussing the basic computational methods, we move on to the first problem of thermodynamics of Al_{13} and Ga_{13} clusters doped with carbon. The chapter begins with the important reports on the doped clusters and the effect of impurity on the melting temperature. Then we present our results of thermodynamic simulations for Al_{13} , Ga_{13} , Al_{12}C and Ga_{12}C . We have calculated the heat capacity curves (C_v) for all four clusters. Our results state that the doping with single tetrahedral carbon impurity brings out significant changes in the melting temperature of the host clusters. Both the doped clusters show reduction in the melting by about 400-500K. This can be explained on account of the charge transfer from the surface atoms towards the central carbon atom in both the clusters. This weakens the surface bonds and clusters melt earlier. In case of gallium, Ga_{13} changes from decahedra to perfect icosahedra on

1. Introduction

doping. This change in the geometry is responsible to the sharp peak in heat capacity curve in case of Ga_{12}C as compared to Ga_{13} .

Chapter 4: In this chapter we have studied the stability of the smallest gold cages namely Au_{16} and Au_{17} at finite temperature. We present few known results on gold clusters addressing the geometry, transition from planer to 3D and its application as catalysis. Next, via *ab-initio* simulations, we have obtained the ground state along with almost 50 distinct isomers for each cluster. This is followed by the finite temperature study of these clusters. It is observed that the cages are stable at least up to 850 K. Although both clusters melt around the same temperature, i.e. around 900 K, Au_{17} shows a peak in the heat capacity curve in contrast to the broad peak seen for Au_{16} . The small peak in Au_{17} is well discussed by the isomer energy analysis.

Chapter 5: A well known two dimensional material ‘graphene’ has become the focus of current research. This one atom thick, sp^2 bonded sheet of carbon atoms is a zero gap semimetal. On the other hand, a fully hydrogenated graphene termed as *graphane* shows a band gap of 3.5 eV by DFT calculations. We have probed this metal insulator transition via successive hydrogenation for 18 systems, right from 0%H to 100%H. The effect of hydrogenation has been explored by many authors but with small hydrogen percentage. After reviewing the relevant work, we move to present our extensive DFT calculations. First, our results show that the hydrogens prefer to decorate graphene in form of a compact, single island which is energetically favored. This is inferred by carrying out 7-8 various configurations for few hydrogenated systems. Next, the analysis of density of states and charge density for each of the 18 systems under consideration bring our surprisingly novel features. As hydrogen coverage increases, the semi-metal turns into a metal, showing a delocalized charge density and then transforms into an insulator. The metallic phase is spatially inhomogeneous in the sense it contains islands of insulating regions formed by hydrogenated carbon atoms and metallic channels formed by contiguous bare carbon atoms. It turns out that it is possible to pattern the graphene sheet to tune the electronic structure. For example, removal of hydrogen atoms along the diagonal of the unit cell, yielding an armchair pattern at the edge, gives rise to a bandgap of 1.4 eV.

Chapter 6: The electronic structure of pure and hydrogenated graphene nanoribbons (GNR) encapsulated in carbon nanotube (CNT) is explored within DFT framework. We have encapsulated the smallest, one atom wide GNR inside CNT of different diameters. The effect of CNT confinement as well as the hydrogenation on GNR structure is studied. Our results show that the pure GNR are sensitive to diameter and undergo structural changes as the diameter is changed. The geometries are sensitive to the placement and concentration of hydrogen with respect to the change in the diameter. For systematically placed 50% hydrogenated GNR, there is no change in the geometry while random placement of hydrogens on GNR turns out to be diameter sensitive. Remarkably, the geometries of the fully hydrogenated ribbon turn out to be insensitive to the diameter, the final structure being two separated linear chains. Both these chains show delocalized charge density on the Fermi level.

2. Theoretical Framework

In this chapter, we will discuss the basic theoretical formalism, different aspects of its implementation and the other tools used throughout this thesis. There are three main ingredients; first, numerically tractable and accurate method for ‘many electron system’. The problem is addressed via density functional theory (DFT) [236]. This is followed by a brief introduction to pseudopotentials and plane wave method. The second ingredient is molecular dynamics (MD), which is a powerful tool for calculating thermodynamic quantities. We have used Born Oppenheimer molecular dynamics (BOMD) for all the calculations. The specific heat is calculated using multiple histogram technique (MH). The third ingredient is the tools to analyze the data. We shall review various indicators such as root mean square bond length fluctuations (δ_{rms}), mean square displacements, radial distribution function etc. to analyze the melting while the ground state properties (electronic and structural) are studied using density of states, analysis of bonding, charge density isosurfaces, isomer energy distribution, band gaps etc.

We shall begin the question of handling many interacting electron problem.

2.1 EARLIER APPROXIMATIONS

Most of the physical problems of interest consist of a large number of interacting electrons and ions. The total number of ions and electrons is usually so large that an exact solution cannot be found. For the past thirty years density functional theory (DFT) has been a dominant method for the quantum mechanical simulation. Before getting into the details of DFT, it is essential to take the review of some earlier approximations used to solve the ‘many body problem’.

2.1.1 Many body problem

Consider a system of atoms with N electrons and M ions. The time independent Schrödinger equation (SE) for these N interacting electrons in an ionic potential of M ions is³

$$\left\{ \begin{aligned} & -\frac{1}{2} \sum_{i=1}^N \nabla_i^2 - \sum_{i=1}^N \sum_{A=1}^M \frac{Z_A}{|\mathbf{r}_i - \mathbf{R}_A|} + \frac{1}{2} \sum_{i \neq j} \frac{1}{|\mathbf{r}_i - \mathbf{r}_j|} - \frac{1}{2M_A} \sum_{A=1}^M \nabla_A^2 \\ & + \frac{1}{2} \sum_{A \neq B} \frac{Z_A Z_B}{|\mathbf{R}_A - \mathbf{R}_B|} \end{aligned} \right\} \Psi = E \Psi \quad (2.1)$$

Note that $\Psi = \Psi(\mathbf{r}_1, \mathbf{r}_2, \dots, \mathbf{r}_N; \mathbf{R}_1, \mathbf{R}_2, \dots, \mathbf{R}_M)$ is a function of electronic and ionic coordinates. Indices A, B run over M nuclei and i, j denote N electrons. Z_A, Z_B represent the charge on ions A and B while \mathbf{R} and \mathbf{r} are ionic and electronic coordinates. The first term denotes the kinetic energy of the electrons, second term is ion-electron interaction, the third term indicates the electron-electron interaction and last two terms are kinetic energy of ions and ion-ion interaction respectively. Such a complex equation is practically impossible to solve for large value of N .

There are several approximations introduced to solve (2.1). A very common and reasonable approximation is Born-Oppenheimer (BO) approximation. Since the mass of nuclei is much larger than the mass of the electrons, they move much slower than electrons. Thus motion of electrons and ions is decoupled and essentially the electronic problem is solved while the coordinates of ions are fixed. So, the motion of ions is ignored while calculating electronic wavefunctions and we decouple ionic and electronic dynamics. Hence equation (2.1) reduces to

$$\left\{ -\frac{1}{2} \sum_{i=1}^N \nabla_i^2 - \sum_{i=1}^N \sum_{A=1}^M \frac{Z_A}{|\mathbf{r}_i - \mathbf{R}_A|} + \frac{1}{2} \sum_{i \neq j} \frac{1}{|\mathbf{r}_i - \mathbf{r}_j|} \right\} \Psi = E \Psi \quad (2.2)$$

³ All the quantities are expressed in atomic units, *i.e.* $\hbar = m_e = e^2 = a_0 = 1$.

Note that only electronic SE is written here. The wavefunction now is a function of electronic coordinates only. One of the simplest solutions for (2.2) was proposed by Hartree which is discussed below.

2.1.2 Hartree and Hartree-Fock Theory

In Hartree theory, the total wavefunction is written as the product of one-electron wavefunction which is given by,

$$\Psi(\mathbf{r}_1, \mathbf{r}_2, \dots, \mathbf{r}_N) = \psi_1(\mathbf{r}_1), \psi_2(\mathbf{r}_2), \dots, \psi_N(\mathbf{r}_N) \quad (2.3)$$

where $\psi_i(\mathbf{r}_i)$ are one electron wavefunctions. Substituting (2.3) in (2.2) and using variational principal, we get Hartree equations,

$$\left(-\frac{1}{2}\nabla^2 - \sum_R \frac{Z}{|\mathbf{r}-\mathbf{R}|} + \sum_{i \neq j} \int \frac{|\psi_j(\mathbf{r}_j)|^2}{|\mathbf{r}_i - \mathbf{r}_j|} d\mathbf{r}_j \right) \psi_i(\mathbf{r}_i) = \epsilon_i \psi_i(\mathbf{r}_i) \quad (2.4)$$

These set of equations (there is one each for each occupied one electron level $\psi_i(\mathbf{r}_i)$) are solved by self consistent way. The term $-Z \sum_R \frac{1}{|\mathbf{r}-\mathbf{R}|} = U^{ion}$ is the external potential and $\int \frac{|\psi_j(\mathbf{r}_j)|^2}{|\mathbf{r}_i - \mathbf{r}_j|} d\mathbf{r}_j = U^{elec}$, the electronic contribution. Each electron experiences a field due to all other electrons. If the remaining electrons are treated as the smooth distribution of negative charge with density $\rho_j(\mathbf{r}_j) = |\psi_j(\mathbf{r}_j)|^2$, then the potential energy of given electron i would be given by U^{elec} . Effectively, this term is the average coulomb potential experienced by i^{th} electron due to N-1 electrons. What has been missed out is Pauli's exclusion principal that is the wavefunction ψ should be antisymmetric under the exchange of two electrons. This antisymmetric condition is satisfied if Ψ is chosen as

$$\Psi = \frac{1}{N!} \begin{bmatrix} \psi_1(\mathbf{r}_1) & \psi_2(\mathbf{r}_1) & \dots & \psi_N(\mathbf{r}_1) \\ \psi_1(\mathbf{r}_2) & \psi_2(\mathbf{r}_2) & \dots & \psi_N(\mathbf{r}_2) \\ \vdots & \vdots & \dots & \vdots \\ \psi_1(\mathbf{r}_N) & \psi_2(\mathbf{r}_N) & \dots & \psi_N(\mathbf{r}_N) \end{bmatrix} \quad (2.5)$$

Such a determinant formed out of one electron orbitals is called Slater determinant. Hartree-Fock (HF) is the method in which the orthogonal orbitals ψ_i are found variationally so as to minimize the total energy. The total energy is given by,

$$E_{HF} = \langle H_\psi \rangle = \sum_i H_i + \frac{1}{2} \sum_{i,j} (J_{ii} - K_{ij}) \quad (2.6)$$

Where

$$H_i = \int \psi_i^*(\mathbf{r}) \left(-\frac{1}{2} \nabla^2 + U^{ion}(r) \right) \psi_i(\mathbf{r}) d\mathbf{r} \quad (2.7)$$

H_i is one electron operator and it describes an electron moving in the field of nucleus.

$$J_{ii} = \int \frac{1}{|\mathbf{r} - \mathbf{r}'|} |\psi_i(\mathbf{r})|^2 |\psi_j(\mathbf{r}')|^2 d\mathbf{r} d\mathbf{r}' \quad (2.8)$$

$$K_{ij} = \int \frac{1}{|\mathbf{r} - \mathbf{r}'|} \psi_i^*(\mathbf{r}) \psi_j(\mathbf{r}) \psi_i(\mathbf{r}') \psi_j^*(\mathbf{r}') d\mathbf{r} d\mathbf{r}' \quad (2.9)$$

J_{ii} and K_{ij} are called as Coulomb and Exchange integrals respectively. Minimization of (2.6) with respect to ψ_i^* gives Hartree-Fock equations.

$$\left(-\frac{1}{2} \nabla^2 + U^{ion}(\mathbf{r}) + U^{ele}(\mathbf{r}) \right) \psi_i(\mathbf{r}) - \sum_j \int \int \frac{1}{|\mathbf{r} - \mathbf{r}'|} \psi_j^*(\mathbf{r}') \psi_i(\mathbf{r}') \psi_j(\mathbf{r}) d\mathbf{r} d\mathbf{r}' = \epsilon_i \psi_i(\mathbf{r}_i) \quad (2.10)$$

The terms $U^{ion}(\mathbf{r})$ and $U^{ele}(\mathbf{r})$ are same as appeared in Hartree equation. The last term is an additional energy term called as exchange term. This term is non-local, represents exchange interaction between same spins and operative only when the spin

of the electrons in i^{th} and j^{th} orbitals are same. (The spin indices are suppressed here) Hartree-Fock equations are also to be solved by self consistent method.

HF is a mean field theory that generates single particle wavefunctions which include the effect of correlations between like-spin electrons. But the correlations between anti parallel spins are missed. In HF, only one Slater determinant formed out of N lowest single particle wavefunctions is chosen as the basis set. The other drawback is, for large systems, it is practically very difficult to solve HF equations and adds lot of computational cost.

There are few methods to solve the many body problem such as configuration interactions (CI), GW method based on Green's function etc. All these methods demand high computational power as number of atoms become large. A realistic many body calculation using full CI or GW for a hundred or more electrons is virtually impossible.

The density functional theory offers a practical and computationally tractable way of computing electronic structure of large systems with high accuracy (at least for a class of problems). Since our calculations are based on DFT, we will discuss it in details.

2.2 DENSITY FUNCTIONAL FORMALISM

DFT is a powerful yet simple formalism which has been successfully applied for calculating the ground state properties and electronic structure of many systems. The key feature of DFT is that it treats the charge density $\rho(x,y,z)$ as the central parameter. There is an extensive literature available on the DFT including excellent books by Parr and Yang [236], Martin [237] and Kohanoff [238]. The formalism of DFT is based on following two theorems, known as Hohenberg Kohn theorems (HK) [239].

2.2.1 Hohenberg Kohn theorems and Kohn- Sham formalism

The first Hohenberg Kohn (HK) theorem was proved by Hohenberg and Kohn in 1964 [239]. It states that '***The electron charge density $\rho(\mathbf{r})$ uniquely determines the external potential***'. Since the external potential fixes the Hamiltonian, effectively all the ground state properties of many-electron system are determined by the charge

density, $\rho(\mathbf{r})$. In other words, the energy is a functional⁴ of charge density and is represented as $E[\rho(\mathbf{r})]$. We begin by writing down the energy terms

$$\begin{aligned} E[\rho(\mathbf{r})] &= \underline{T[\rho(\mathbf{r})] + E_{ee}[\rho(\mathbf{r})]} + E_{ext}[\rho(\mathbf{r})] \\ &= \underline{F_{HK}[\rho(\mathbf{r})]} + E_{ext}[\rho(\mathbf{r})] \end{aligned} \tag{2.11}$$

$$F_{HK}[\rho(\mathbf{r})] = T[\rho(\mathbf{r})] + E_{ee}[\rho(\mathbf{r})]$$

The term $E_{ext}[\rho(\mathbf{r})]$ in (2.11) is due to the external potential which is simply ion-electron interaction and is expressed as

$$E_{ext}[\rho(\mathbf{r})] = \int U^{ion}(r) \rho(\mathbf{r}) d\mathbf{r} \tag{2.12}$$

$F_{HK}[\rho(\mathbf{r})]$ is the contribution from kinetic energy and electron-electron interaction. The real complexity in solving (2.11) is $F_{HK}[\rho(\mathbf{r})]$ as its exact form is not known. $F_{HK}[\rho(\mathbf{r})]$ is called as a universal functional as it is independent of the system at hand. It applies well to all the systems irrespective of the entities. Thus first theorem is an existence theorem. The second HK theorem states that ‘**The charge density, $\rho(r)$, which minimizes the energy functional $E[\rho(r)]$, is the exact ground state charge density**’. This establishes the variational nature of the total energy with respect to the charge density.

However the practical realization of these theorems was provided by Kohn and Sham [240]. They provided an approximate method to solve for the unknown terms in (2.11). Within KS formalism, the system of N interacting electrons is mapped onto a fictitious system of N non-interacting electrons having the same charge density and moving in an effective potential. Now the energy functional is rewritten as

$$E[\rho(\mathbf{r})] = T_s[\rho(\mathbf{r})] + E_{ext}[\rho(\mathbf{r})] + E_H[\rho(\mathbf{r})] + E_{XC}[\rho(\mathbf{r})] \tag{2.13}$$

Where $T_s[\rho(\mathbf{r})]$ is the kinetic energy of non interacting system which produces same ground state charge density and is calculated exactly from the one-electron orbitals

⁴ A functional is a map for going from function to a number.

$$T_s[\rho(\mathbf{r})] = -\frac{1}{2} \int \psi_i^*(\mathbf{r}) \nabla^2 \psi_i(\mathbf{r}) d\mathbf{r} \quad (2.14)$$

$E_{ext}[\rho(\mathbf{r})]$ is given by (2.12). Next, $E_H[\rho(\mathbf{r})]$ is the Hartree energy which is nothing but classical Coulomb interaction between the electrons.

$$E_H[\rho(\mathbf{r})] = \frac{1}{2} \iint \frac{\rho(\mathbf{r})\rho(\mathbf{r}')}{|\mathbf{r} - \mathbf{r}'|} d\mathbf{r}d\mathbf{r}' \quad (2.15)$$

The last term $E_{XC}[\rho(\mathbf{r})] = (T - T_s) + (E_{ee} - E_H)$ is called as exchange-correlation energy which includes the quantum terms like the difference in kinetic energy of interacting and non-interacting system and the difference in actual electron-electron interaction and Hartree term. This $E_{XC}[\rho(\mathbf{r})]$ incorporates all the exchange and correlation effects. However the exact form of this functional is not known and needs approximate methods to calculate it. The commonly used approximations are local density approximation (LDA) and generalized gradient approximation (GGA). We will discuss these in details little later.

Next, the minimum of the energy functional (2.13) yields the exact ground state charge density. We minimize (2.13) with respect to the density $\rho(\mathbf{r})$, subjected to the constraint that total number of electrons must be N . The Lagrange multiplier of this constraint is the electronic chemical potential μ .

$$\delta[E(\rho)] - \mu \left(\int \rho(\mathbf{r}) d\mathbf{r} - N \right) = 0 \quad (2.16)$$

Using (2.16) and (2.13), the minimization condition gives a set of non linear equations known as Kohn-Sham equations and are given as

$$\left(\frac{-\nabla^2}{2} + V_{KS}(\mathbf{r}) \right) \psi_i(\mathbf{r}) = \epsilon_i \psi_i(\mathbf{r}) \quad (2.17)$$

$$\rho(\mathbf{r}) = \int |\psi_i(\mathbf{r})|^2 d\mathbf{r}$$

The effective potential V_{KS} is the sum of external (ionic) potential, Hartree or Coulombic potential and exchange correlation potential.

$$V_{KS}(\mathbf{r}) = V_{\text{ext}}(\mathbf{r}) + V_H(\mathbf{r}) + V_{XC}(\mathbf{r}) \quad (2.18)$$

V_{KS} is a local potential and is actually a functional of $\rho(\mathbf{r})$ and has the form,

$$V_{KS}(\mathbf{r}) = V_{\text{ext}}(\mathbf{r}) + \int \frac{\rho(\mathbf{r}') d\mathbf{r}'}{|\mathbf{r} - \mathbf{r}'|} + \frac{\delta E_{XC}}{\delta \rho(\mathbf{r})} \quad (2.19)$$

The equations (2.17) describe the behavior of non-interacting electrons in an effective potential $V_{KS}(\mathbf{r})$. Evidently, these equations are coupled. It is very important to realize that if the exact forms of E_{XC} and V_{XC} were known, the Kohn-Sham strategy would lead to the exact energy!!

DFT thus cleverly maps an interacting many body problem to non-interacting electrons having same charge density. This allows working with single particle equation with an effective potential. The solution to (2.17) gives total energy and electronic charge density of the ground state. All other quantities can be derived from these. The KS equations need to be solved self-consistently as the form of V_{KS} and ψ are unknown. The starting point for solving the KS equation is the external potential and a trial, random wavefunction (and trial charge density of course!). The new set of wavefunctions having new charge density is obtained by solving (2.17). This in turn yields new effective potential, which is plugged into the equation. The process continues till the initial and final charge densities match. Thus within DFT formalism the real many body problem which is intractable is reduced to one electron equation in an effective potential. The charge density $\rho(\mathbf{r})$ is a non-negative function of only three spatial variables. It vanishes at infinity (for finite sized systems) and integrates to the total number of electrons.

It is worth noting that formally there is no physical interpretation of the single-particle Kohn-Sham eigenvalues and orbitals; they are merely introduced to facilitate the determination of charge density. The exception is the highest occupied state, for

which it can be shown that the eigenvalue corresponding to the highest occupied state yields the ionization energy of the system (as shown by Janak theorem).

2.2.2 Exchange correlation functionals

It turns out that the accuracy of DFT to predict the properties is crucially dependant on the choice of exchange correlation functional. In fact we note that because of use of exchange correlation potential, the Kohn-Sham energy is not strictly variational! There are now many different flavours of functionals available. The simplest and widely used approximation is the local density approximation (LDA) [236, 239, 241]. It is based on interacting electron gas model. In LDA, it is assumed that the density varies slowly, each small volume looks like a homogeneous and uniform electron gas and the exchange correlation functional is constructed as

$$E_{XC}^{LDA} = \int \rho(\mathbf{r}) \epsilon_{xc}(\rho) d\mathbf{r} \quad (2.20)$$

Where $\epsilon_{xc}(\rho)$ is the exchange correlation energy per particle of a uniform electron gas of density ρ . For practical purposes, E_{XC}^{LDA} is split into exchange and correlation separately, $E_{XC}^{LDA} = E_X^{LDA} + E_C^{LDA}$ Out of this the exchange term is known analytically from homogeneous electron gas as

$$E_X^{LDA} = \frac{-3}{4} \left(\frac{3}{4}\right)^{1/3} \int \rho(\mathbf{r})^{4/3} d\mathbf{r} \quad (2.21)$$

The correlations E_C^{LDA} are estimated from detailed many body calculations on interacting electron gas such as quantum Monte Carlo methods.

LDA has been proven to be a good approximation for estimating properties like structure, vibrational frequencies, elastic modulus and phase stability. It is often surprisingly accurate and for systems with slowly varying charge densities it generally gives good results. However it overestimates the binding energies. In weakly bound systems these errors are exaggerated and bond lengths are too short. LDA is not suitable for highly non-homogenous systems where the charge density varies rapidly.

It also fails to describe the strongly correlated systems. In addition, Van der Waals bonding and hydrogen bonding are very poorly described by LDA.

The failures of LDA are well recognized and there have been many sustained efforts to improve upon the functional. GGA, generalized gradient approximation [242] is used for the systems having non-homogeneous charge density. GGA takes into account the gradient of the charge density at a particular location.

$$E_{XC}^{GGA} = \int \rho(\mathbf{r}) \epsilon(\rho(\mathbf{r}), \nabla\rho(\mathbf{r})) d\mathbf{r} \quad (2.22)$$

In most of our work we have used a well established form of GGA that is PBE [262]. Recently, a class of functionals have been introduced which are a step ahead of GGA. These are called as Hybrid functional. These include a fraction of exact Hartree Fock exchange energy calculated as a functional of the Kohn-Sham molecular orbitals. These appear to be promising ones. However it is still not possible to use ‘standard’ exchange correlations functional for all systems which will predict many properties with uniform and acceptable accuracy.

2.2.3 Solving Kohn-Sham equations

Now we turn towards the implementation of KS theory. Even if the formal KS solution still has to be solved for variety of systems, such as atoms, molecules, surfaces, they pose different boundary conditions; therefore accurate numerical solution is still a problem. Fortunately, during the last many years, a number of techniques have been developed for the practical implementation of KS. Depending on the nature of the problem, number of methods has been successfully implemented. One of the methods is to expand each of the Kohn-Sham orbitals in a suitable basis, converting the real space equation into a matrix equation. Typically all orbitals are expanded in terms of a suitable basis, that is $\psi_i(\mathbf{r}) = \sum_{j=0}^{\infty} c_j \phi_j(\mathbf{r})$, $\phi_j(\mathbf{r})$ being set of basis functions. The commonly used basis functions are plane waves, ion centered Gaussians, atomic orbitals etc. and the choice of basis set is indeed very much system dependant. We have used plane wave (PW) basis set for all the calculations as implemented in VASP code [261].

Plane wave method

The advantages of plane wave (PW) are ample. It is the simplest one to represent the electron wavefunctions. It is complete and has inbuilt periodicity. Here we briefly present PW implementation within KS.

According to the Bloch's theorem, in a periodic system, a wavefunction can be written as

$$\psi_i(\mathbf{r}) = e^{i\mathbf{k}\cdot\mathbf{r}} u_k(\mathbf{r}) \quad (2.23)$$

Where $u_k(\mathbf{r})$ is periodic.

$$u_k(\mathbf{r}) = \sum_G c_G e^{i\mathbf{G}\cdot\mathbf{r}} \quad (2.24)$$

Here \mathbf{G} are the lattice vectors in reciprocal space. Thus the electronic wavefunction $\psi_i(\mathbf{r})$ is written as linear combination of plane waves

$$\psi_i(\mathbf{r}) = \sum_G c_{\mathbf{k},\mathbf{G}} e^{i(\mathbf{k}+\mathbf{G})\cdot\mathbf{r}} \quad (2.25)$$

In principal, infinite number of plane waves are required to expand the wavefunction. However, in practice, the plane waves with kinetic energy less than certain cut off energy are used.

$$\frac{1}{2}(\mathbf{k} + \mathbf{G})^2 \leq E_{cut} \quad (2.26)$$

Apart from this, PW are site independent and hence free of superposition errors. They are computationally simple to operate and are controlled by single parameter that is cut-off energy. One of most important features of PW is that these are not dependant on the ionic positions. Hence the forces on the ions are easy to calculate by straightforward application of Hellmann Feynman theorem. Pulley forces are not required

The plane wave method is useful for the periodic systems, but for the systems like clusters, the calculations are performed within a large simulation box which is repeated periodically. The size of the box is so chosen that the interaction between clusters in neighboring boxes is negligible. This strategy allows the use of plane waves as the basis set. The wavefunctions vanish at the boundary of the box. The convergence of the results can be increased by increasing number of plane waves.

2.3 PSEUDOPOTENTIALS

For computationally tractable solution, we like to keep the number of plane waves minimal without losing the accuracy. However all electron calculations include core and valence electrons and it would still be expensive to use plane waves. This is because the tightly bound core orbitals demand high value of energy cut-off and effectively large number of plane waves to describe them. Quite clearly, most of physical properties are determined by the valence electrons while core wavefunctions by and large do not change from their atomic values. In the pseudopotential approach, only valence electrons are considered and the strong ionic potential due to core is replaced by replaced by a nodeless pseudopotential such that it is identical to the all electron (AE) potential beyond a certain cut-off radius (r_c). Within the core region, the pseudo wavefunction is constructed so as to remove all the nodes. In other words, the valence wavefunction must be identical to AE wavefunction beyond the cut off. This gives a lot of freedom of choosing the nature of valence wavefunction inside core region. This freedom is exploited for the construction of smooth potential as feasible. The obvious requirement is it should be nodeless inside.

This effectively reduces the computational cost thereby reducing the number of plane waves. The concept is pictorially demonstrated in figure 2.1

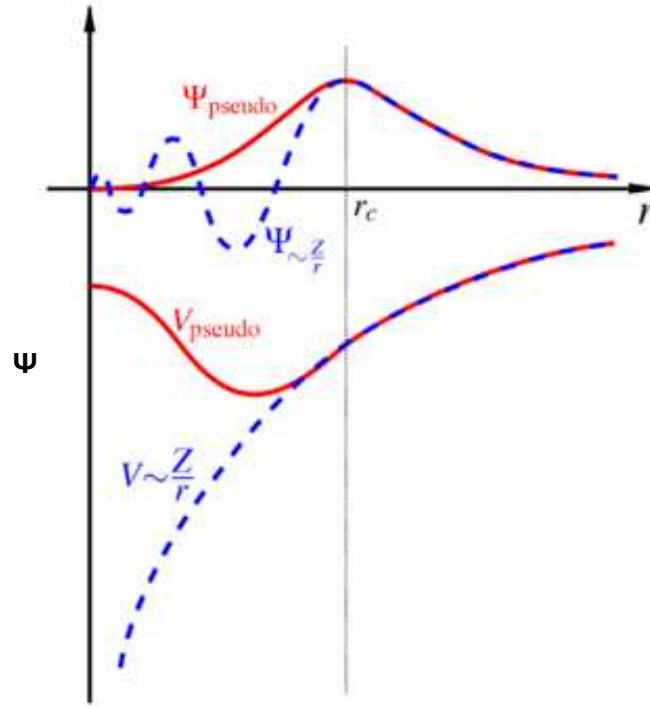


Figure 2.1 - The all electron wavefunction and potential (blue color) and pseudo wavefunctions and potential (red color). All the quantities are shown as a function of distance r from the atomic nucleus.

The usual method of pseudopotential generation is to determine the all electron eigenfunctions of an isolated atom using the KS equation within DFT with same exchange correlation potential.

$$\left(\frac{-\nabla^2}{2} + V_{KS}(\mathbf{r}) \right) \psi_i^{AE} = \epsilon_i \psi_i^{AE} \quad (2.27)$$

Where ψ^{AE} is the wavefunction for the all electron (AE) atomic system with angular momentum component l . This is replaced by a smooth and nodeless pseudo wavefunctions ψ^{ps} within the cut-off radius obeying certain criteria that are noted below. The pseudopotential is then constructed by directly inverting the Kohn-Sham equation with the pseudo wavefunction ψ^{ps} . A cut off radius is so chosen that the outside wavefunction can be smoothly extrapolated inside by number of ways.

Although various techniques are well established to construct PP, a good PP should obey certain criteria which are given below -

1. Real and pseudo valence eigenvalues are same. $\epsilon^{al} = \epsilon^{ps}$

2. Norm conservation –

$$\int_0^{r_c} |\psi_i^{AE}(\mathbf{r})|^2 d\mathbf{r} = \int_0^{r_c} |\psi_i^{PS}(\mathbf{r})|^2 d\mathbf{r} \quad (2.28)$$

3. Transferability - The pseudopotential when transferred to a different environment should retain the same energy variation up to the first order as that of the all-electron (AE) potential. This property is called as transferability.
4. Pseudo wavefunctions should be identical to all electron wave function outside the cut-off radius. The logarithmic derivatives of real and pseudo wave function and their first energy derivative agree beyond cut-off.

The first non empirical PP was constructed by Phillips and Kleinman [243] but the above conditions were not satisfied by these PP. The norm conservation and transferability conditions were satisfied by the pseudopotentials proposed by Hamann, Schlüder and Chiang [244]. The norm conserving PP are extremely expensive to apply for 3d transition metal atoms due to the requirement of large number of plane waves to represent the core states. They can be made softer by increasing the cut-off radius but there is an upper bound beyond which if the radius is increased, the transferability is affected. A solution to this problem was proposed by Vanderbilt who showed that it is possible to release the norm-conservation criteria, if one corrects for the resulting difference between the exact and the pseudo charge density using localized augmentation functions centered on each atom. Such PP are known as Vanderbilt's ultrasoft pseudopotentials (USPP) [245]. Many modern pseudopotential calculations use ultrasoft PP generated by Vanderbilt. As the name suggests these have much softer pseudo potentials and require considerably lesser number of plane waves. We have used USPP in two problems based on the thermodynamics of clusters. For more understanding on PP the reader can refer the books [246]. For the practical purpose, we use a separable form of PP given by Bylander and Kleinman [247].

Although the PP treatment has successfully worked for last many years, it still misses the effect of core states which could affect number of properties; therefore a method known as projected augmented wave method (PAW) was formulated to incorporate the effect of core. PAW method is used very often in *ab-initio* calculations due to its advantages over PP.

PAW

PAW bridges the pseudopotential approach with all electron method. PAW is developed by Blöchl [248] who proposed to reconstruct all-electron wavefunctions from the pseudo wavefunctions. The PAW method works directly with the full AE wave functions and AE potentials. In PAW approach, the space is divided into atom centered augmentation spheres inside which the wavefunctions are taken as atom like while outside the sphere, some envelope functions are defined. The central idea is as follows : In the core region the electronic wavefunction could be described more efficiently by atomic-like wavefunctions while in the region far away from nuclei, the electrons are more like ‘free’ and can be described by plane waves. At the boundaries, both the functions are matched. The PAW method is a linear transformation between smooth valence (and semi-core) pseudo (PS) wavefunctions, $\tilde{\psi}_n$ and all electron (AE) wavefunctions ψ_n . The core states of the atoms ϕ_i are fixed to the reference shape for the isolated atom. We follow Blöchl’s work and the mathematical formalism given by him:

Define a linear transformation operator \hat{T} which transforms an auxiliary (pseudo) smooth wave function $\tilde{\psi}_n(\mathbf{r})$ to the true all electron wave function $\psi_n(\mathbf{r})$, n is the label for one particle state

$$\psi_n(\mathbf{r}) = \hat{T}\tilde{\psi}_n(\mathbf{r}) \quad (2.29)$$

Express the total energy by auxiliary wavefunctions

$$E = E[\psi_n(\mathbf{r})] = E[\hat{T}\tilde{\psi}_n(\mathbf{r})] \quad (2.30)$$

Variational principal with respect to auxiliary wavefunctions yields

$$(T^\dagger HT - T^\dagger T \epsilon_n)\tilde{\psi}_n(\mathbf{r}) = 0 \quad (2.31)$$

Instead of normal KS, these are to be solved, but now the Hamilton operator has a different form, $T^\dagger HT$, an overlap operator $T^\dagger T$ occurs and the resulting auxiliary wave functions are smooth. When we evaluate physical quantities we need to evaluate expectation values of an operator A ,

$$\langle A \rangle = \sum_n \langle \psi_n | A | \psi_n \rangle = \sum_n \langle \tilde{\psi}_n | T^\dagger A T | \tilde{\psi}_n \rangle \quad (2.32)$$

The transformation operator T is defined as

$$\hat{T} = 1 + \sum_i (|\phi_i\rangle - |\tilde{\phi}_i\rangle) \langle \tilde{p}_i| \quad (2.33)$$

$|\phi_i\rangle$ are all electron atomic orbitals. These are constructed from real atomic potentials.

$|\tilde{\phi}_i\rangle$ pseudo atomic orbital. These are constructed from pseudopotentials.

$\langle \tilde{p}_i|$ is projector function

The operator transforms pseudo wavefunctions to all electron wavefunction.

$$|\psi_n\rangle = |\tilde{\psi}_n\rangle + \sum_i (|\phi_i\rangle - |\tilde{\phi}_i\rangle) \langle \tilde{p}_i | \tilde{\psi}_n \rangle \quad (2.34)$$

These projector functions are localized inside the augmented spheres that is $\tilde{p}_i(\mathbf{r}) = 0, \mathbf{r} > R_a$. Also the all electron orbitals and pseudo orbitals are same outside the augmented spheres. $\phi_i(\mathbf{r}) = \tilde{\phi}_i(\mathbf{r}), \mathbf{r} > R_a$. The projector functions are so chosen that they are orthogonal to pseudo orbitals $\langle \tilde{p}_i | \tilde{\phi}_j \rangle = \delta_{ij}$

2.4 MOLECULAR DYNAMICS

Molecular dynamics (MD) [249] is a powerful computational tool which calculates the classical trajectories of the ions in the system. MD in conjunction with a proper ensemble is used to calculate the finite temperature properties. In the present case, we have used canonical ensemble. In addition, we have also used a variant form of this technique to generate several equilibrium geometries. The crucial question is what is the form of inter-atomic potential from which the forces are derived. Traditionally, MD uses parameterized potentials where the parameters are generated using experimental data or a combination of *ab-initio* calculations. Obtaining the correct parameters is highly refined art. Indeed the results are dependent on the correctness of parameters. In fact more often parameters may turn out to be environment dependant.

An obvious remedy towards this problem is to calculate the forces on ions based on instantaneous electronic structure. Quite clearly, such calculation is computationally expensive and so usually limited to small sizes may be upto few hundred electrons. There are two different ways to carry out these calculations - Born Oppenheimer molecular dynamics (BOMD) and Car Parrinello MD [250]. In the former case, the electronic ground state is solved for each ionic configuration while in later electronic degrees of freedom are treated as a fictitious dynamical variables which leads to system of coupled equations of motion for both ions and electrons. All our calculations are based on BOMD simulations.

Implementation of BOMD simulations

As noted earlier, the electronic and ionic motions are decoupled in BO approximation. The electronic degrees of freedom are treated quantum mechanically while ionic motion is treated classically that is via Newton's laws. The electronic ground state is obtained by appropriate electronic structure methods (in the present case, density functional theory) keeping the ions stationary. The nuclear motion evolves on a potential energy surface. With advances in the computer technology, this ab-initio MD proves to be a very powerful and predictive tool for tracking the dynamics of ions. We will discuss the typical strategy combining the electronic structure with MD.

Consider a system consisting of M ions and N electrons. The first step is given positions $\mathbf{R}_1, \mathbf{R}_2, \dots, \mathbf{R}_N$, the ground state and its total energy is obtained via DFT that is by solution of KS. Then the force on ion at \mathbf{R}_I is calculated from Hellmann-Feynman theorem as

$$F_I = - \frac{\partial E(\mathbf{R})}{\partial \mathbf{R}_I} \quad (2.35)$$

Where $E(\mathbf{R})$ is the electronic energy. Having obtained the forces on ions, the trajectories are obtained by integrating Newton's equations. Several numerical methods are available to solve the above equation of motion. Here we present a velocity-verlet algorithm [251, 252] as an example. In this algorithm the position and velocities at time $(t + \delta t)$ is calculated as

$$\mathbf{r}(t + \delta t) = \mathbf{r}(t) + \mathbf{v}(t)\delta t + \frac{1}{2}\mathbf{a}(t)(\delta t)^2 \quad (2.36)$$

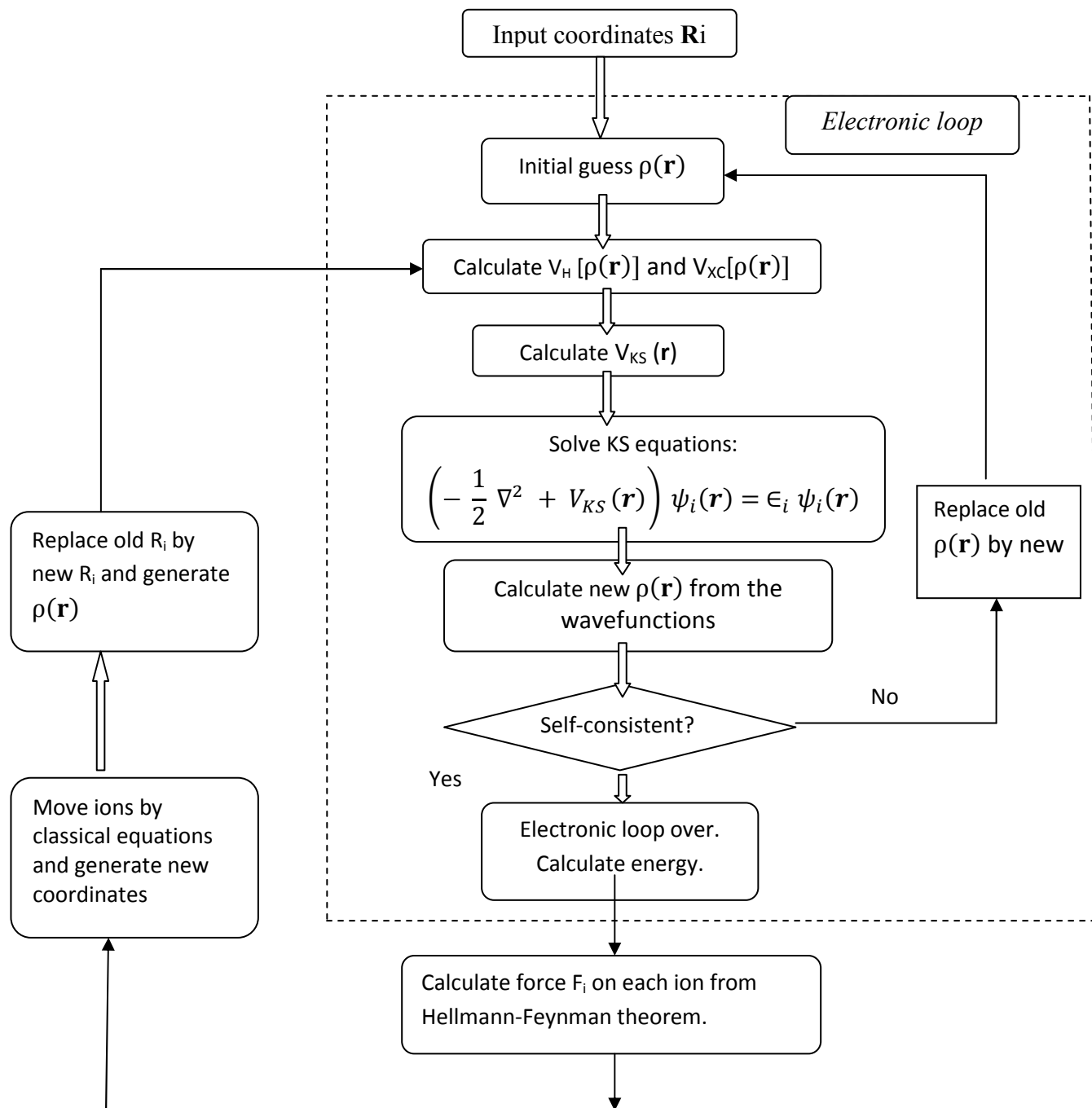
$$\mathbf{v}(t + \delta t) = \mathbf{v}(t) + \frac{1}{2}(\mathbf{a}(t) + \mathbf{a}(t + \delta t))(\delta t)$$

The calculated forces together with the set of velocities complete one step of MD, giving new set of positions for ions. At these new ionic positions, the KS equations are re-solved to get new electronic ground state. The process continues till sufficient data is generated which are ionic positions as a function of time at a given temperature. The entire process is schematically explained by the following flow chart.

Thus at end of typical MD run, we have huge data in terms of positions and velocities of all ions in system, for a few hundred- thousand steps and for few tens of temperatures. The task is to analyse this data and extract relevant thermodynamic quantities.

2.5 TOOLS AND TECHNIQUES

There are variety of tools and techniques that we have used to analyze the data. First, we shall discuss the few techniques to obtain the ground state geometry. In the next section, various other ground state properties such as bonding, density of states, isomer analyses etc. are studied. Lastly, we shall give the details of multiple histogram technique and few traditional thermodynamic indicators like Lindeman criteria and mean square displacement.



2.5.1 Geometry optimization

Obtaining the correct ground state (GS) of a given cluster is a difficult task. It is well known that number of minima grows as factorially with the number of atoms. Therefore in almost all the cases, we have obtained several (50-500, depending on the size of the system) local minima and picked up the lowest as our GS. In addition other

techniques, like simulated annealing are carried out to ensure the reliability of the obtained structure. Although, there are several methods, there is no definite way to prove that given structure is the global minimum.

We shall first understand the concept of global minimum which is associated with the optimized geometry. Generally the system could have number of potential barriers that should be overcome to reach for the global minimum. If the ions are instantaneously relaxed it is possible that system gets trapped into local minima. For a given potential energy surface there could be number of local minima. A simple illustration is shown in figure 2.2. In real systems, the nature of energy surface is quite complex. The total energy surface has to be spanned by overcoming the local potential barriers A, B to look for the global minima C.

Many a times a saddle point is mistaken as the lowest energy configuration. A typical saddle point in 3D looks exactly as its name suggests. (figure 2.2-(b)) In order to distinguish between the saddle point and global minimum, the vibrational frequencies are calculated. The saddle point will have negative values of vibration frequencies.

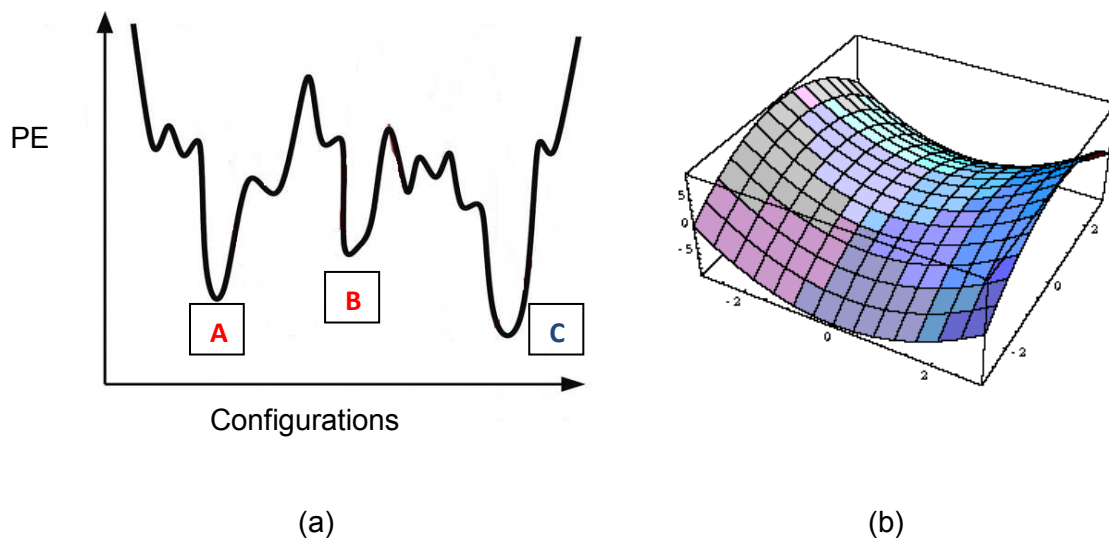


Figure 2.2 – (a) A two dimensional graph explaining the concept of local and global minima. (b) The saddle point in a 3D plot shown.

One of the useful techniques to locate the global minima is simulated annealing. It tries to mimic the natural process of solidification of liquids by slow cooling. The general concept can be understood as follows. Suppose we consider a

metal and heat it so that it melts and forms a liquid. At high temperatures in liquid state, all the atoms will move rapidly with respect to each other. As the liquid is slowly cooled, the atoms will move slower and slower. At certain temperature the liquid will solidify and if the cooling rate is slow enough, it may solidify in a crystalline state, which has the lowest state of energy. If one cools the liquid quickly or 'quench' it, the system may solidify in an amorphous or disordered state. In short, by slow cooling or 'annealing' one can reach the minimum energy state. This is the idea behind simulated annealing strategy. The strategy is applied typically in case of the clusters because a cluster can have number of local minima separated by energy barriers.

We have carried out simulated annealing for obtaining the ground state geometry of the clusters. Starting from an initial random configuration, the system is heated to definite temperature which is generally above melting. Then the system is maintained for a sufficiently long time. This enables the atoms to overcome all the potential barriers and span the entire configuration space. Now the system is cooled extremely slowly so that the atoms proceed to the lowest energy configurations corresponding to some local minima. This yields number of low energy structures. The lowest amongst these is the probably ground state. The rate of cooling is the most important factor in the whole process.

Now we describe another technique based on MD which has proved to be very useful. We use MD method to obtain the trajectories at three to four temperatures near and above melting. Then we select few hundreds of configurations either randomly or at regular intervals. These configurations are then quenched by several methods like steepest descent to obtain several minima. The lowest energy structure is then considered as GS.

2.5.2 Ground state properties

In previous sections we briefly introduced the theoretical framework in which the calculations are done. In what follows we will study different tools used to analyze the phase space data. The analysis of bonding is examined via electron localization function (ELF) [253] along with the total charge density. For a single determinantal wavefunction built from KS orbitals ψ , ELF is defined as

$$\chi_{ELF} = \left[1 + \left(\frac{D}{D_h} \right)^2 \right]^{-1} \quad (2.37)$$

Where

$$D_h = \left(\frac{3}{10} \right) (3\pi^2)^{5/3} \rho^{5/3} \quad (2.38)$$

$$D = \frac{1}{2} \sum_i |\nabla \psi_i|^2 - \left(\frac{1}{8} \right) |\nabla \rho|^2 / \rho$$

$\rho = \rho(\mathbf{r})$ is valence electron density. D is the excess local kinetic energy density due to Pauli repulsion and D_h is the Thomas-Fermi kinetic energy density. The numerical values of χ_{ELF} are conveniently normalized to a value between zero and unity. A value of 1 represents a perfect localization of the valence charge, while the value for the uniform electron gas is 0.5. Typically, the existence of an isosurface in the bonding region between two atoms at a high value of χ_{ELF} , say, 0.70, signifies a localized bond in that region. The ELF can be analyzed by plotting the isosurfaces which locate the localization domains. This is most conveniently done by examining the isosurfaces for successive values of ELF, starting with the highest. We show isosurfaces of ELF for Ga_{13} and Ga_{12}C clusters in figure 2.3. The locations of the maxima of ELF are called attractors and the set of all the points in space that can be connected to them by maximum gradient paths are called basins. Such basins are seen for few atom pairs in Ga_{13} while for Ga_{12}C ; all Ga atoms are connected with equal bonding strength. The detailed results are discussed in Chapter 3. In general, there are more than one attractor of an N -electron system, and hence, more than one basin.

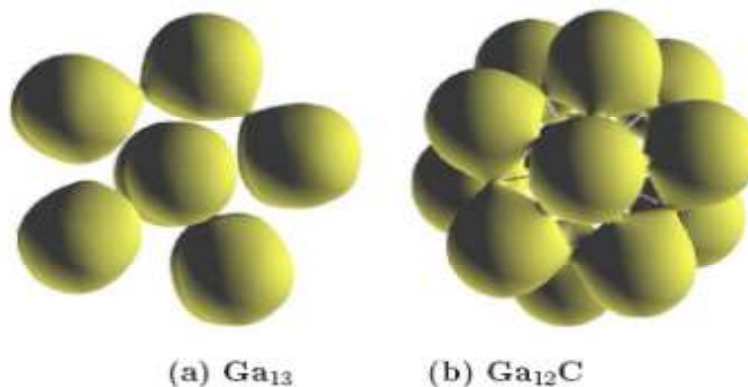


Figure 2.3 - Isosurfaces of ELF for (a) Ga_{13} and (b) Ga_{12}C at value 0.67.

The various other ground state properties are analyzed via calculation of bond lengths, distance from center of mass, eigenvalue spectrum and HOMO-LUMO gap. For graphene and GNR problems, the density of states (DOS) are particularly important in order to understand the band structure. The finite temperature properties of clusters are examined with few thermodynamic indicators which are discussed in the next section.

2.5.3 Thermodynamic indicators

In this section we present the traditional melting indicators - root mean square bond length fluctuation and mean square displacement. We have calculated the heat capacity as a measure of ‘melting’. However, unlike bulk materials, where the solid to liquid transition is a single step process defined by the melting temperature, the clusters normally show a broad heat capacity curves spread over the range of temperatures. One needs the density of states (DOS) to calculate different thermodynamic quantities. For this purpose it is required to have a set of simulations over a range of temperatures which are closely spaced. However, due to the high computational demand, we need a technique that allows us to reduce the number of temperatures being simulated and to reliably interpolate the behavior of the system at temperatures in between. A special technique called as multiple histogram (MH) provides a method to extract DOS from the simulation data and calculate specific heat.

Multiple histogram (MH) technique

A complete thermodynamic analysis of the simulation is possible using MH which treats ions as classical particles moving on a potential energy surface $V(\mathbf{R})$. The Hamiltonian $H(\mathbf{R},\mathbf{P}) = V(\mathbf{R}) + K(\mathbf{P})$, where \mathbf{R} is set of ionic coordinates and \mathbf{P} is set of ionic momenta. $K(\mathbf{P})$ is the kinetic energy given by,

$$K(\mathbf{P}) = \sum_I \frac{P_I^2}{2m_I} \quad (2.39)$$

The $V(\mathbf{R})$ is obtained by minimizing the potential energy functional with respect to the density ρ . Since the Hamiltonian is separable, we can express full density of states as convolution of configurational density of states and kinetic density of states. The kinetic density of states are known analytically. The idea of MH is to extract the classical density of states $\Omega_c(E)$ from the distribution of potential energy and then calculate the entropy, $S = k \ln \Omega_c(E)$. The separate treatment of the configurational and kinetic parts is desirable, because the kinetic part of the problem can be handled analytically. A numerical sampling of the phase space is only required for the configuration space. For this, first the system is treated as a canonical ensemble of N particles, where the energy is exchanged with the surrounding. Popular techniques to control the temperature include velocity scaling, N ose-Hoover thermostat. We have used N ose-Hoover thermostat [254] to raise the temperature of the system. Starting from low temperature, the system is maintained at different temperatures that normally vary by 100 K. The simulation data of potential energies is obtained by carrying out MD at each of the temperatures. The time step for MD plays a crucial role in determining the total simulation time. Generally, initial few iterations are discarded for thermalization.

We wish to interpolate the values over the range of temperatures including those for which simulations are not performed. The contribution of a point in the phase space of a system to the statistical quantity being observed is, in the canonical ensemble, proportional to the Boltzmann factor at that temperature. Hence, given a data point from the simulations of one temperature point, its contribution at another

temperature would be proportional to $e^{-\beta_i(E-E_0)}$. This observation is the basis of the approach proposed by Ferrenberg and Swendsen [255].

Next, the entire potential energy spectrum ranging from V_0 (corresponding to the lowest temperature) to maximum V_{\max} (corresponding to the maximum temperature) is divided into 'n' small bins of width $\delta V = (V_{\max} - V_0)/n$. V_j is the central value of potential energy in each bin. For every temperature the number of potential energies falling in each bin are noted. Let n_{ij} be the number of times the potential energy assumes a value laying in j^{th} bin at temperature i . Then the probability that the system takes a potential energy in j^{th} bin at inverse temperature $\beta = 1/K_B T_i$ is estimated from the simulations as

$$p_{ij}^{\text{sim}} = \frac{n_{ij}}{\sum_j n_{ij}} \quad (2.40)$$

The standard canonical probability for finding the system with potential energy V_{ij} is given by

$$P_{ij} = \frac{\Omega_c(V_j)e^{-\beta_i V_j}}{Z_c(\beta_i)} \quad (2.41)$$

$\Omega_c(V_j)$ are the density of states and $Z_c(\beta_i)$ is the partition function.

Equating and taking logarithm,

$$\frac{S_i}{k_B} + \alpha_i = \beta_i V_j + \ln n_{ij} \quad (2.42)$$

Where

$$S_j = [\ln \Omega_c(V_j)] \quad (2.43)$$

$$\alpha_i = \ln \left(\sum_j n_{ij} \right) - \ln Z_c(\beta_i)$$

2. Theoretical framework

This results into $N_\tau * N_V$ equations, where temperature index $1 \leq i \leq \tau$ and bin index $1 \leq j \leq V$. The equations are to be solved for S_j and $Z_c(\beta_i)$ by minimizing,

$$\sum_{i,j} n_{ij} \left[\frac{S_i}{k_B} + \ln \left(\sum_j n_{ij} \right) - \ln Z_c(\beta_i) - \beta_i V_j - \ln n_{ij} \right]^2 \quad (2.44)$$

The final expression for S_j , partition function and internal energy are

$$S_j = k_B \frac{\sum_{i=1}^{N_\tau} n_{ij} (\ln n_{ij} + \beta_i V_j - \alpha_i)}{\sum_{i=1}^{N_\tau} n_{ij}} \quad (2.45)$$

$$Z(T) = \sum_{j=1}^{N_V} \exp \left(S_j - \frac{V_j}{T} \right) \quad (2.46)$$

$$U(T) = \frac{3T(N-1)}{2} + \frac{1}{Z} \sum_{j=1}^{N_V} \exp \left(S_j - \frac{V_j}{T} \right) V_j \quad (2.47)$$

$$C_v = \frac{3(N-1)}{2} + \frac{1}{T^2} (\langle V^2 \rangle - \langle V \rangle^2) \quad (2.48)$$

Where $\langle V \rangle = U(T)$. In present thesis, we shall be concerned mainly with the canonical specific heat, defined as usual by

$$C = \frac{\partial U}{\partial T} \quad (2.49)$$

where $U = \langle V + K \rangle_T$ is the average total internal energy in a canonical ensemble at temperature T . Since we exclude the contribution of the center of mass (COM) motion to the ionic kinetic energy K ,

$$\langle K \rangle_T = \frac{1}{2} (3N - 3) k_B T \quad (2.50)$$

with N being the number of atoms in the cluster. At sufficiently low T , in addition, since the ions show simple harmonic motion, the potential energy contains only the vibrational degrees of freedom without rotational and COM contribution i.e. its degrees of freedom = $3N - 6$. Thus, at low T

$$\langle V \rangle_T \approx \frac{3}{2}(3N - 6)k_B T \quad (2.51)$$

Combining Eqns. 2.49, 2.50 and 2.51, one obtains the zero-temperature classical limit of the rotational plus vibrational specific heat such as

$$C_0 = (3N - 9/2)k_B \quad (2.52)$$

which is conveniently used to normalize our plots of canonical specific heat. There are few other traditional phase change indicators such as root mean square bond length fluctuations (RMS) and mean square displacements. These are applied to the bulk systems as the melting indicators.

Lindeman Criteria

One of the first indicators for identifying melting temperature in bulk was proposed by Lindeman, where the thermal vibrations of the atoms in crystal are used to explain melting. The average amplitude of vibrations increases with the temperature. At a point the amplitude becomes so large that the atoms exceed their nearest neighbor distances and a melting process initiates. A simple criteria given by Lindeman is when root mean vibration amplitude reaches at least 10% of near neighbor distance, a melting might be expected. We have calculated ‘root mean square bond length fluctuation’, δ_{rms} for every temperature and it indicates the average bond length fluctuations over complete time span.

$$\delta_{rms} = \frac{1}{N(N-1)} \sum_{i>j} \frac{\sqrt{\langle r_{ij}^2 \rangle_t - \langle r_{ij} \rangle_t^2}}{\langle r_{ij} \rangle_t} \quad (2.53)$$

Here, N is the total number of bonds. r_{ij} is the distance between atoms i and j , $\langle \dots \rangle$ represents a time average over entire trajectory.

Mean square displacements (MSD)

Another important indicator for phase change is MSD which is given by

$$\langle R^2(t) \rangle = \frac{1}{MN} \sum_{m=1}^M \sum_{l=1}^N [(\mathbf{R}_l(t_{0m} + t) - \mathbf{R}_l(t_{0m}))^2] \quad (2.54)$$

N is the number of atoms in the system and the average is carried out over M time origins spanning entire trajectory. MSD indicates the displacement of the ions with respect to their original position as a function of time. The MSD converge as the square of the radius of the cluster when system is in liquid state. In solid like region all the atoms perform small oscillatory motion about fixed point; hence the MSD are negligibly small. At higher temperature, the atoms perform diffusive motions, the MSD increase and eventually saturate to the value nearly equal to the diameter of the cluster. We have calculated the MSD for the individual atom.

Radial distribution function

The radial distribution function ($g(r)$) is defined as average number of atoms between the region r and $r+dr$. The radial distribution function for a symmetric cluster will exhibit distinct peaks at low temperatures corresponding to different shells. With increasing temperature these peaks are expected to broaden due to oscillatory motion of ions. Eventually, at high temperatures, there will be a merger of these peaks indicating the diffusive motion of ions.

2.6 ERROR ANALYSIS

The results of any numerical calculation deviate from the exact value due to various types of errors. The errors could be due to implementation, statistical or computational. One should try to minimize these for the accurate results. To this end, we illustrate few convergence criteria that are to be followed to reduce the errors in calculation of C_v . The temperatures that are selected for the simulation should be such

2. Theoretical framework

that the histograms have sufficient overlap. This is essential because the simulation data is interpolated over large range of temperatures. In figure 2.4 we illustrate histograms for Au₁₆ cluster which shows a good overlap for selected temperatures. It is interesting to observe the effect on specific heat curve if few temperatures are omitted resulting in a gap in histogram. The histograms for the same system with 2 temperatures less are shown in figure 2.5. The corresponding Cv curves with ‘all’ and ‘omitted’ temperatures are plotted together and shown in figure 2.6. It is clear from the figure that the resultant Cv curve varies and gives wrong interpretation if there is no good overlap of histograms.

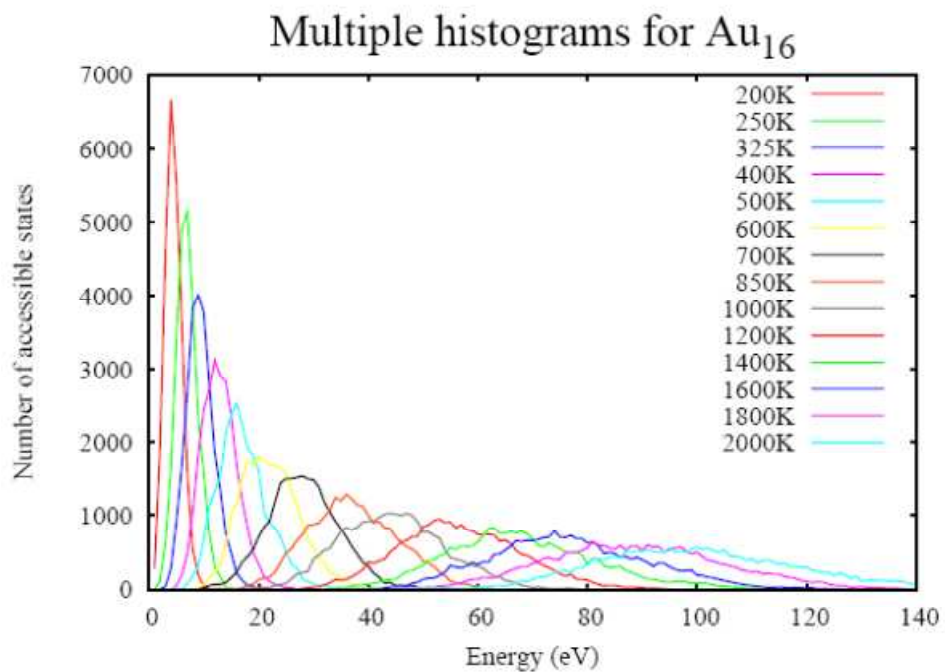


Figure 2.4 – Multiple Histograms for Au₁₆ cluster. The temperatures range from 200 K to 2000 K and the histograms show a good overlap.

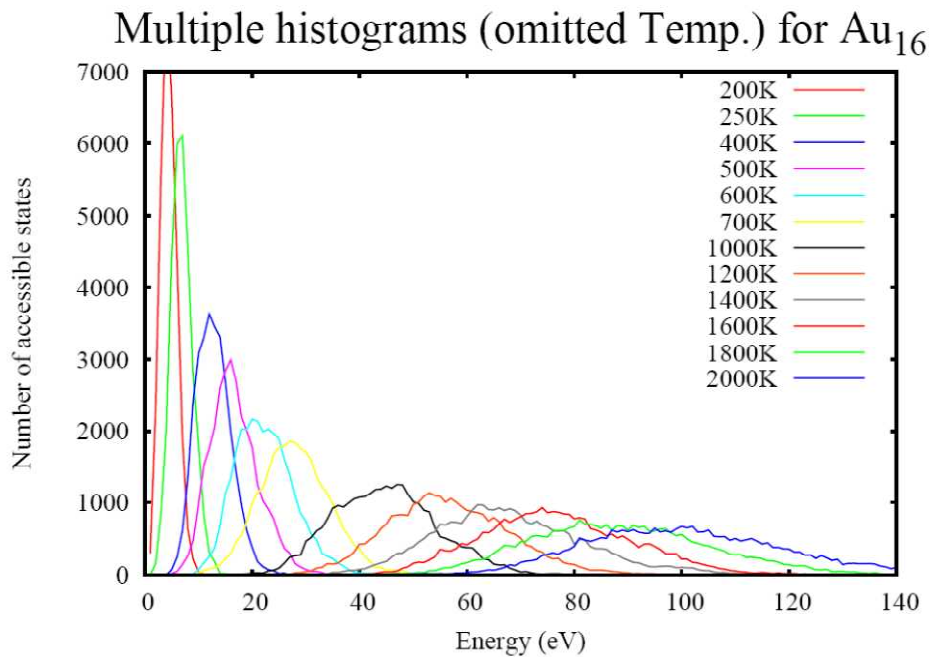


Figure 2.5 - Multiple Histograms for Au₁₆ cluster with 325 K and 850 K are omitted as compared to figure 2.4. The missing temperatures are evident by a gap after 250 K and 700 K.

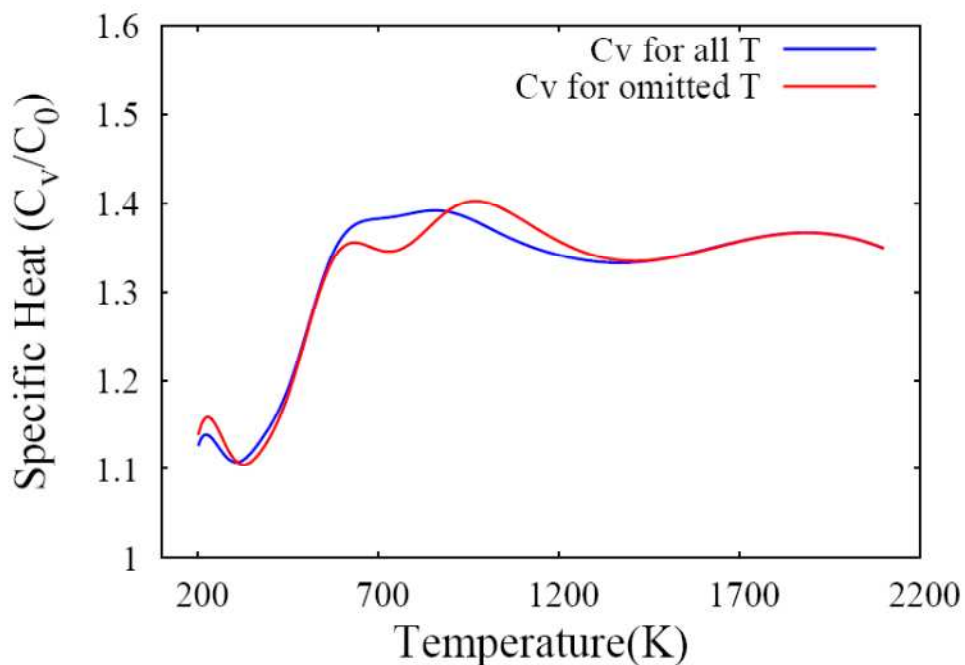


Figure 2.6 – The specific heat curves calculated using ‘all’ temperatures and ‘omitted’ temperatures for Au₁₆

Another important factor is the variation in the bin width. The C_v should be invariant under change of bin width atleast for appreciable range. We shall elaborate this point by plotting C_v for Au_{16} with bin widths 0.001, 0.002 and 0.004, in figure 2.7. It is clear from the figure that C_v curve is same for all the bin width indicating the convergence under change in the bin width.

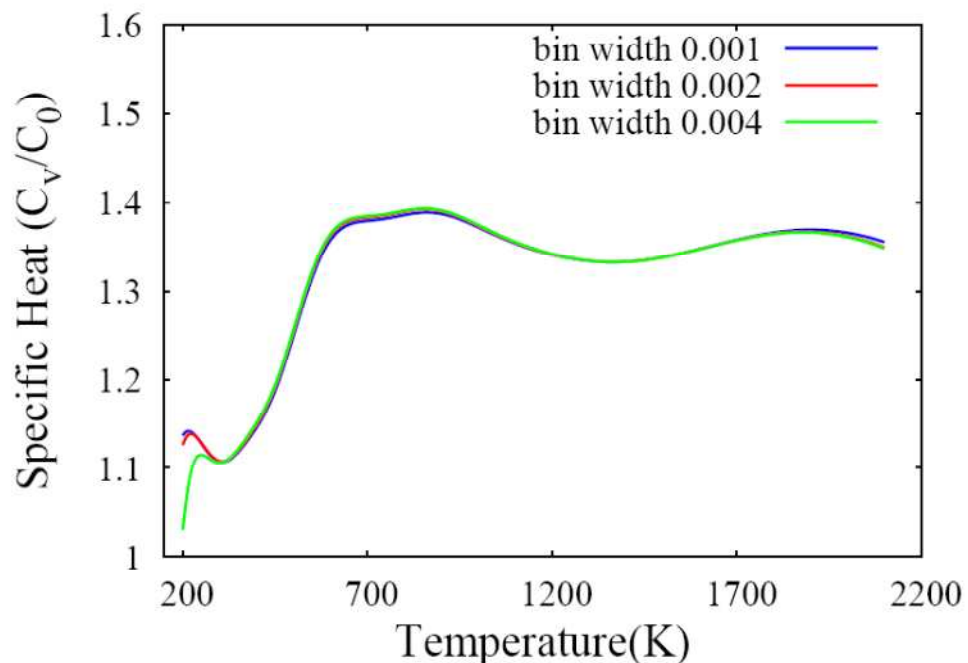


Figure 2.7 – The specific heat for Au_{16} plotted with different bin widths. It is clear that for all three bin widths C_v has converged.

Next, the statistical data leads to erroneous results and care should be taken to overcome errors due to these factors. The simulation time is an important factor for determining the statistical averages. As discussed earlier, during all the calculations, the first 30ps data is discarded for thermalization. The next question is how much data is sufficient for quantitatively correct trajectory averages. To decide this, the simplest way is to check for the convergence of C_v curve over different simulation time. We show specific heat curves for Au_{16} calculated over 60, 75, 90 and 120ps data in figure 2.8. From the figure it is clear that low statistics does not give correct results. The simulation time of 90 and 120ps is well converged and hence we have used 90ps data for all the calculations.

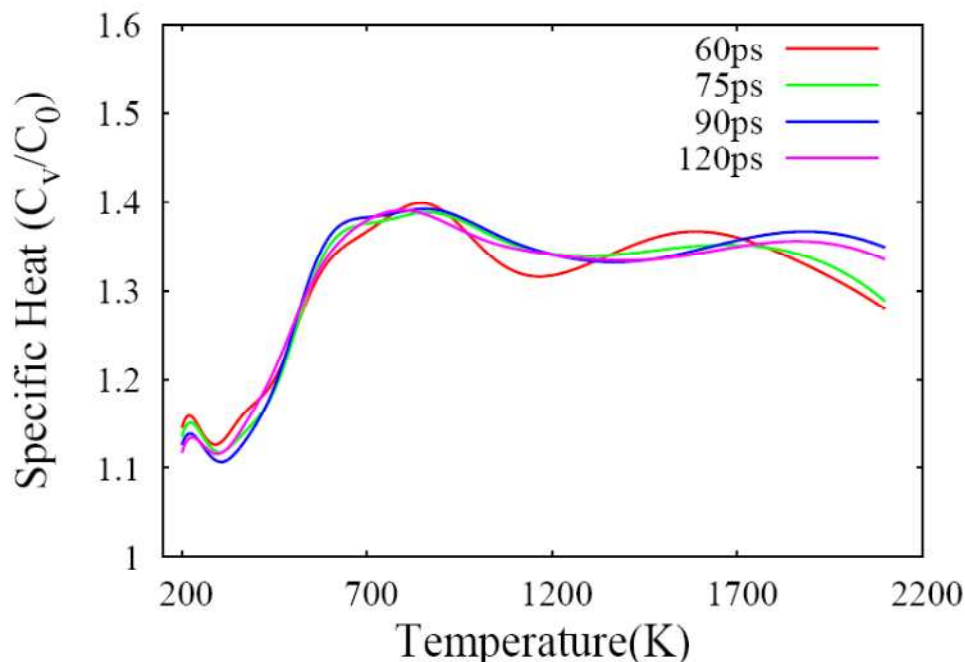


Figure 2.8 - The specific heat for Au_{16} plotted with different simulation time. The convergence is seen as the simulation time is increased upto 120ps.

We have tested all the systems using above convergence tests with respect to bin widths and temperatures during calculation of C_v and other indicators also.

Next, we make a brief note of few other sources of errors.

- ❖ Pseudopotential choice – We deal with the DFT based on pseudopotential approach. There are large number of PP available and one of the ways to choose an appropriate pseudopotential is by comparing the results of bond length and binding energies of dimer to an all electron calculation or to the experimental values.
- ❖ The errors can also occur due to the insufficient energy cutoff and small simulation box. We note that these errors can be controlled and minimized by a proper choice of the relevant parameters. For example, the size of the box is chosen in such a way that, the cluster is completely isolated from its images. We have performed the initial calculations with minimum of three different box sizes 15, 20 and 30 to ensure that the results do not deviate. Similarly, E_{cut} should be chosen such that the results are appreciably converged with respect to the further increase in the E_{cut} . We have always performed several

preliminary calculations to fix the size of the box and energy cutoff for every system of interest.

- ❖ The another source of error is number of k points, which are especially important in the calculation of graphene. To reproduce the peculiar band structure of graphene and obtain the correct V-shaped density of states, it was necessary to use $60 \times 60 \times 1$ k mesh for the unit cell of graphene. For large unit cells, the optimization is carried out with $11 \times 11 \times 1$ while the self consistency is obtained over $27 \times 27 \times 1$ mesh. We have repeated all these calculations for different sets of k points and used the optimum ones in all the calculations.
- ❖ Errors can also arise due to factors like the choice of convergence criteria in the total electronic energy and forces, time interval taken for MD simulation, thermalization time etc. These errors can be minimized by adjusting the energy and force convergence criteria, time interval properly. However, changing these parameters to minimize the error can slow down the computation. Hence, optimum values of these parameters should be selected so as to speed up the calculation but still to maintain the accuracy of the results.

The author empathetically notes that analysis and control of errors is a crucial component and must be paid adequate attention. This is especially important when we use readily available packages for our calculations.

3. Thermodynamics of carbon-doped Al and Ga clusters: Ab initio molecular dynamics simulations

3.1 INTRODUCTION

One of the effective ways of tuning the properties of the clusters is by adding an impurity which induces many changes in the ground state geometry, chemical bonding and the stability of the host cluster. Hence, it is of considerable interest to probe the finite temperature behavior of such heterogeneous clusters. The magnitude of the changes so induced depends on the nature of the impurity. In many of the cases, it has been observed that a single atom can bring out significant changes in the geometry as well as in the nature of the bonding of the host cluster. A notable example being that of metal encapsulated Si cages, where prolate geometries of small Si clusters have been transformed into small cages of Si [256]. A metallic like bonding observed in pure Li_n clusters gets modified into a combination of ionic and metallic bonding when doped with Sn atom [257]. Indeed, the idea of using an impurity to alter the properties of the small clusters has been exploited by a number of works. There have been some remarkable reports on finite temperature behavior of the mixed clusters [207, 212, 215, 258, 259]. An interesting example is that of icosahedral silver nanoclusters; where Mottet *et. al.* showed that a single impurity of Ni or Cu can considerably shift their melting temperature even for sizes of more than a hundred atoms [207]. Apart from altering the melting temperatures, an impurity can be used to suppress the fragmentation. For example, pure Si and Sn clusters in the size range of 15–20 atoms are known to fragment in the temperature range of 1200 K and 650 K respectively [260]. It has been shown that Si clusters could be stabilized by adding an appropriate impurity like Ti and the fragmentation could be avoided at least until 2600 K [215]. Doping small Li clusters with Al and Sn has been shown to change the shapes of the heat capacity curves of the host clusters significantly [212, 213]. Thus, clusters provide a playground for tuning up the properties with the help of an appropriate impurity.

3. Carbon doped Al₁₃ and Ga₁₃ clusters

A notable example of interest is that of Al₁₃, where the well known stability of close shell systems within jellium approximation (for a total number of valence electrons equal to 8, 20, 28, 40, 58,...) has been exploited to enhance the stability by substituting the central Al atom with tetravalent impurities [224, 225, 226]. These studies were motivated by the possibility of using such stable clusters as building blocks for designing the novel solids. These investigations also have brought out many interesting observations. Substitutional doping of an Al₁₃ cluster by a tetravalent atom results in a substantial gain in the binding energy. The maximum enhancement was seen for the carbon-doped cluster, Al₁₂C. Interestingly, its bulk modulus turns out to be smaller than the other dopants. It is also observed that the behavior of the central atom is more like that of a metallic one rather than the expected covalent type. Although the ground state properties of Al₁₃ and Al₁₂X have been extensively probed, their finite temperature properties remain virtually unexplored. To the best of our knowledge, the only investigations reported to probe the finite temperature behavior of Al₁₂C is that due to Seitsonen *et. al.*[227]. They found that the icosahedral structure is stable up to a temperature of the order of 930 K. Although they used *ab initio* molecular dynamics, their conclusion was based on simulations performed at only one temperature.

In this work, we have chosen to investigate the finite temperature properties of Al₁₃, Ga₁₃, Al₁₂C, and Ga₁₂C. Although Al₁₃ and Ga₁₃ are isoelectronic, they are known to exhibit very different bonding. Al clusters in this size range show delocalized charge density exhibiting metallic like bonding, whereas small clusters of gallium are known to be covalently bonded and melt at temperatures higher than their bulk melting point. In addition, Al₁₂C and Ga₁₂C are 40 electron systems showing enhanced stability. Therefore, it is of considerable interest to investigate their finite temperature properties. The focus of the present work is to see the effect of doping on the heat capacity curves and to explore the correlation between their shapes and the ground state geometry. Indeed, our first principle simulations show a rather significant effect on the shape and the peak of the heat capacity, especially for Ga₁₃. The chapter is divided into 3 sections. In section 3.2, we briefly note the computational details. Section 3.3 presents the results and discussions. First, we compare the zero temperature properties such as the ground state geometry and the nature of bonding of pure clusters to that of C-doped clusters, followed by a

presentation of the finite temperature results. The concluding section 3.4 ends with summary.

3.2 COMPUTATIONAL DETAILS

All the calculations are carried out using Born-Oppenheimer molecular dynamics. A DFT based simulation code, VASP [261] is used. The ion-electron interaction is described by Vanderbilt's ultra soft pseudopotentials. We have used generalized gradient approximation given by Perdew-Burke-Ernzerhof (PBE) [262]. For Al, the energy cutoff of 9.50 Ry is used. For Ga, it is 9.54 Ry, while for C, it is 21.08 Ry. The size of the simulation box is 15Å which is found to provide sufficient convergence in the total electronic energy. The larger box of 20Å has also been tested and there was no variation in the results. In order to calculate the ionic heat capacities, we sample the phase space at 26 various constant temperatures ranging from 200 to 2500K using a Noé thermostat [263]. For each temperature the system is maintained for 50,000 iterations. The simulation time for a single iteration is 3 femtosecond (fs); hence the total duration of each temperature is 150 picoseconds (ps). Next, we have discarded the initial 30ps data (that is first 10000 iterations) for each temperature for the thermalization. The remaining 120ps are utilized for the calculations. Since the results converge for 90ps data, we have performed all the calculations over 90ps data. The total simulation time is thus approximately 2.4 nanoseconds (ns). Following the finite temperature study, the ionic heat capacity of each cluster is computed using the multiple-histogram (MH) method [173, 255, 264]. The computation of the heat capacity using the MH technique is sensitive to the number of temperatures at which the thermodynamic behavior of the cluster is simulated. The range and the number of temperatures are chosen to ensure an adequate overlap in the potential energy distribution. The method extracts the classical ionic density of states $\ln \Omega_c(E)$ of the cluster, or equivalently, the classical ionic entropy $S(E) = k_B \ln \Omega_c(E)$ from the simulation data. With $S(E)$ in hand, one can evaluate thermodynamic averages in a variety of ensembles. The method has been already discussed in Chapter 2.

Among various traditional indicators of phase change, we have calculated the root mean square bond length fluctuations (δ_{rms}) and mean square displacement (MSD). δ_{rms} gives the average fluctuations in the bond lengths over the entire time span. In the present case, we have calculated separate δ_{rms} for bonds between surface

3. Carbon doped Al₁₃ and Ga₁₃ clusters

atoms and central atom and for bonds among surface atoms. MSD are calculated for individual atoms which differentiate between a disordered cluster and an ordered cluster. A disordered cluster at low temperatures will show a spread in the MSD of individual atoms, indicating a large variation in the displacements of different atoms in contrast to the bunching seen in MSD for an ordered cluster. We will elaborate this while discussing the finite temperature behavior of Ga₁₃ and Ga₁₂C. The nature of bonding between the atoms in a cluster is analyzed using the electron localization function (ELF) along with the total charge density and molecular orbitals.

3.3 RESULTS AND DISCUSSIONS

We begin our discussion by examining the ground state geometries of Al₁₃ and Al₁₂C, Ga₁₃ and Ga₁₂C, which are shown in figure 3.1. The ground state structure of Al₁₃ has already been studied and is known to be a Jahn-Teller distorted icosahedron. Our geometry (figure 3.1-(a)) is in agreement with the earlier results, in which the shortest bond between the central Al atom and the outer shell is 2.64Å. It has been reported that upon the substitution by carbon, the structure changes to a perfect icosahedron with all 12 Al atoms placed at 2.53Å from the central carbon atom. Thus, the most stable structure of Al₁₂C is an icosahedron with the carbon at the center (figure 3.1-(b)). The ground state geometry of Ga₁₃ is known to be a slightly distorted decahedron (figure. 3.1-(c)), in which the distance from the central atom to surface atoms ranges from 2.69Å to 2.81Å [265]. It is interesting to note that upon doping, this decahedral structure changes to an icosahedron with the carbon atom at the center as shown in figure 3.1-(d). For Ga₁₂C, the distance from the central carbon to the outer shell is 2.53Å. The presence of carbon shortens the bonds between the central atom and the atoms in the outer shell.

Further, analysis of the various bond lengths indicates that the nearest neighbor distance between the surface atoms shows opposite trends. For Al₁₂C, we observe a reduction by 0.08Å, while for Ga₁₂C; it increases by 0.09Å.

3. Carbon doped Al₁₃ and Ga₁₃ clusters

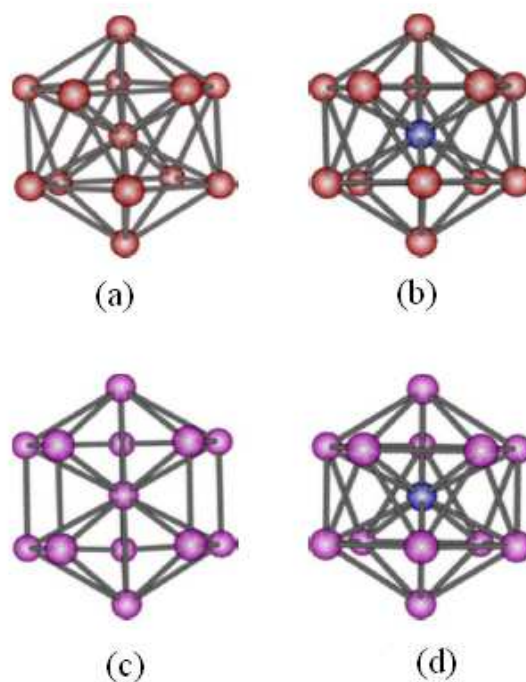


Figure 3.1 – The ground state geometries of (a) Al₁₃ - distorted icosahedra (b) Al₁₂C - perfect icosahedra (c) Ga₁₃ - decahedra and (d) Ga₁₂C - perfect icosahedra.

Table 3.1 shows relevant parameters such as the shortest bond lengths, the binding energy (BE), and the gap between the highest occupied molecular orbital and the lowest unoccupied molecular orbital (HOMO-LUMO). It can be seen that the introduction of carbon enhances the BE as well as the HOMO-LUMO gap in both clusters.

System	Al ₁₃	Al ₁₂ C	Ga ₁₃	Ga ₁₂ C
Symmetry	Icosahedra	Icosahedra	Decahedra	Icosahedra
Bond length(A)	2.64-2.69	2.53	2.6-2.8	2.53
BE(eV)	-37.10	-42.30	-32.03	-37.37
HOMO-LUMO gap(eV)	1.56	2.00	1.40	2.00
Melting peak (K)	1800	900	1200	800

Table 3.1 - The symmetry, bond lengths, HOMO-LUMO gap and melting peak for pure and doped clusters. The bond lengths are shown between the central and surrounding atoms.

3. Carbon doped Al₁₃ and Ga₁₃ clusters

The nature of the bonding in all the clusters can be understood by examining the total charge density and the molecular orbitals. Jena and co-workers have extensively investigated the evolutionary character of the bonding in small Al clusters ranging from 2 to 15 [266]. It has been clearly shown that the clusters with more than seven atoms show an *s-p* hybridized character. In contrast to this, small clusters of Ga even in the size range up to 40–45 atoms are known to be covalently bonded [267].

In figure 3.2, we show various isosurfaces of total charge density for all the clusters. It is interesting to note that for Al₁₃ (figure 3.2-(a)), the charge around the central aluminum is not spherically symmetric and, in fact, shows the formation of direct bonds with six nearest neighbor Al atoms. The overall charge density is, as expected, well spread and delocalized. In contrast to this, for Ga₁₃, the formation of localized bonds is evident (figure 3.2-(e)).

Significant changes are observed in the bonding due to substitution by carbon atom. For Al₁₂C, it can be seen that even up to 1/3rd value of the charge density (figure 3.2-(c)), most of the charge is around central carbon and is spherically symmetric, and indicating filling of carbon centered *p* orbitals. Evidently, there is charge transfer from all the surface atoms towards the central carbon atom. This establishes a partial ionic bond between the central carbon atom and the surface atoms. As a consequence, the size of the cluster shrinks. Such charge depletion also results in a weakening of the strength of the bonds between the surface atoms. The charge density in the case of Ga₁₂C shows a similar behavior. Most of the charge is around the carbon and is spherically symmetric (figure not shown). In order to understand the nature of bonding in this cluster, we show an isosurface of charge density at low value of 1/7th in figure 3.2-(f). This brings out the localized nature of the charge in contrast to the delocalized one as seen in Al₁₂C.

3. Carbon doped Al_{13} and Ga_{13} clusters

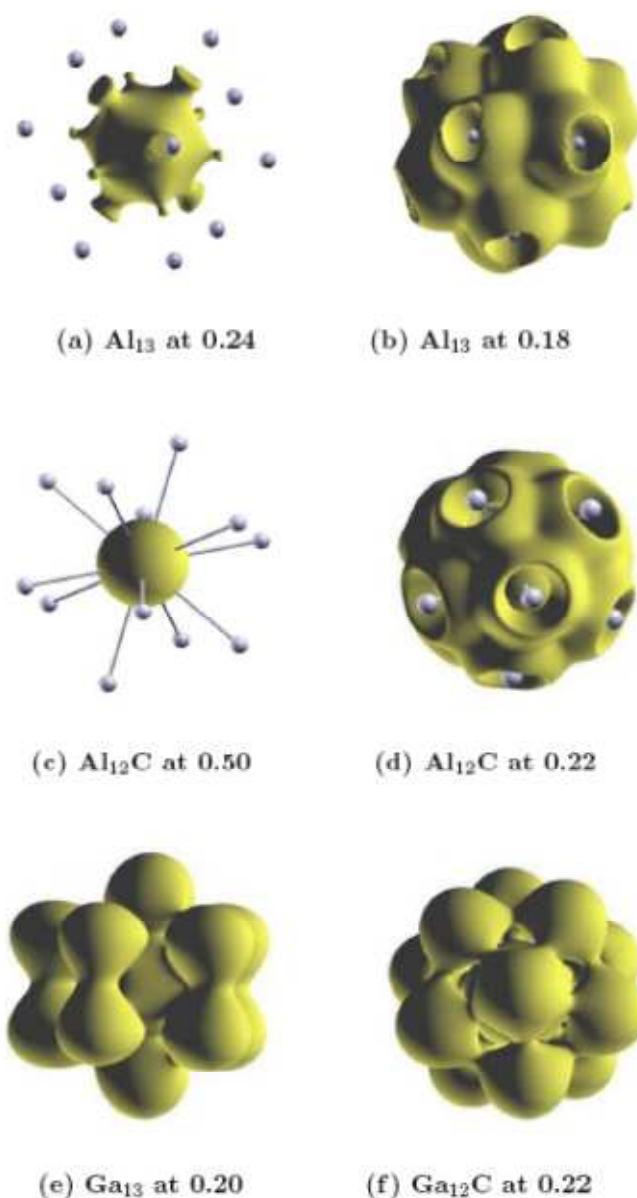


Figure 3.2 - Isosurfaces of total charge density at various values for all the clusters. The values of the maximum charge density for Al_{13} and Ga_{13} are 0.26 and 0.28, respectively, while for Al_{12}C and Ga_{12}C are 1.50 and 1.60, respectively.

It may be pointed out that there is a subtle difference in the molecular orbitals (MOs) participating in the bonding of the surface atoms. Figure 3.3 shows isosurfaces of the charge density corresponding to a typical MO, near HOMO for both the carbon-doped clusters. The participating orbitals in Al_{12}C are s - p hybridized, while in the case of Ga_{12}C , they are purely p type.

3. Carbon doped Al₁₃ and Ga₁₃ clusters

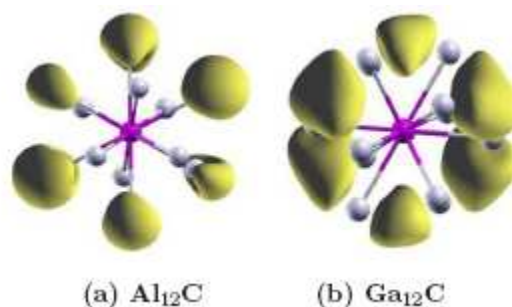


Figure 3.3 – Isosurfaces of charge density for the molecular orbital (HOMO-2) at about 1/4th of the maximum value.

The eigenvalue spectrum for all the clusters is shown in figure 3.4. The effect of introducing the impurity on the eigenvalue spectra is remarkable. In both cases, the spectra became highly degenerate, reflecting the higher symmetry of the icosahedral structure. In fact, both spectra show a jellium like degenerate eigenvalue structure. The lowest level is *s*-like centered around the carbon. It may be pointed out that although the spectra for both the clusters are nearly identical to that of the jellium model, there is a difference in the nature of eigenfunctions between these two clusters. In the case of Al₁₂C, all the eigenfunctions resemble corresponding jellium eigenfunctions of *s*, *p*, *s*, and *d* types. However, the eigenfunction of Ga₁₂C, especially near HOMO, is quite different and is dominantly formed by *p*-type orbitals centered on the surface Ga atoms.

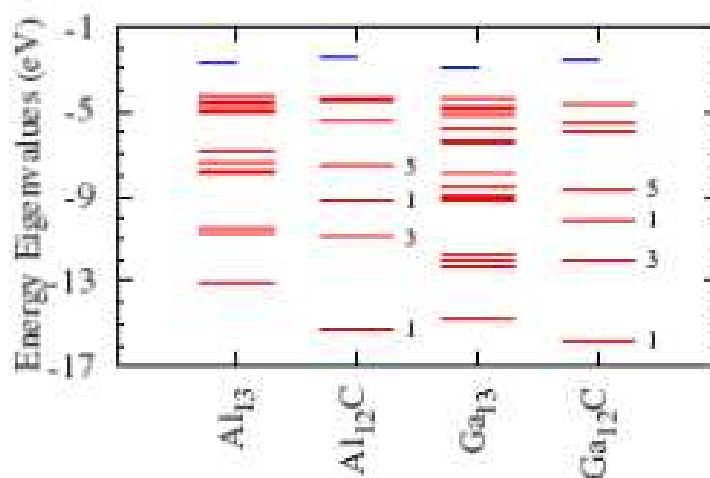


Figure 3.4 – Eigenvalue spectra for all the systems. The topmost short line (blue) indicates LUMO.

3. Carbon doped Al₁₃ and Ga₁₃ clusters

So far, we have investigated the zero temperature properties of these clusters. We have observed that substitutional doping by C results in a more symmetric structure, with increased BE and higher HOMO-LUMO gap. Now, we present the results of our finite temperature simulations for pure and carbon-doped clusters. In figures 3.5 and 3.6, we show the ionic heat capacities of Al₁₃ and Al₁₂C, Ga₁₃ and Ga₁₂C respectively. In finite size systems, the solidlike to liquidlike transition is spread over a range of temperatures. The melting temperature is identified with the peak in the heat capacity curve. Several observations can be made from figures 3.5 and 3.6. The observed peak for Al₁₃ is around 1800 K, and for Ga₁₃, it is around 1200 K. It is interesting to note that both clusters melt at substantially higher temperatures compared to their bulk counterparts, which are 933 K and 303 K for Al and Ga, respectively. The effect of carbon substitution is to decrease the melting temperature typically by 800 K for Al and by 400 K for Ga. Interestingly, both carbon-doped clusters melt in a similar temperature range, i.e., around 800–900 K. However, the most remarkable observation is the sharp nature of the specific heat curve in Ga₁₂C as compared to Ga₁₃.

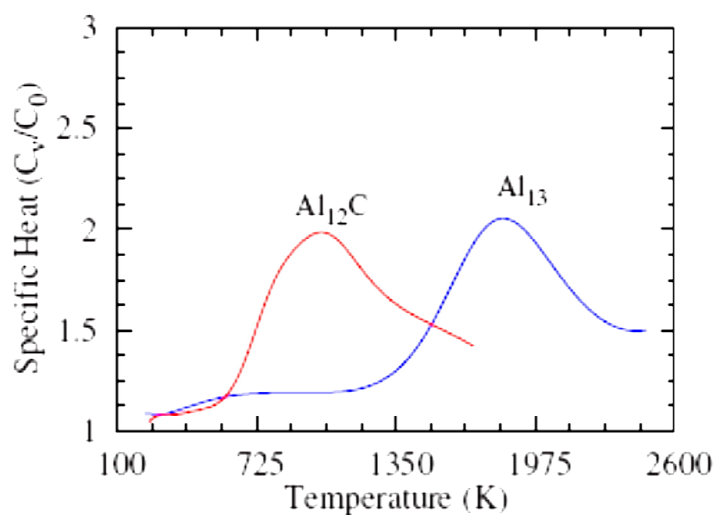


Figure 3.5 – Normalized specific heat for Al₁₃ and Al₁₂C. Note that shapes of the specific-heat curves are similar, but the melting temperature is lowered by almost 800 K upon doping.

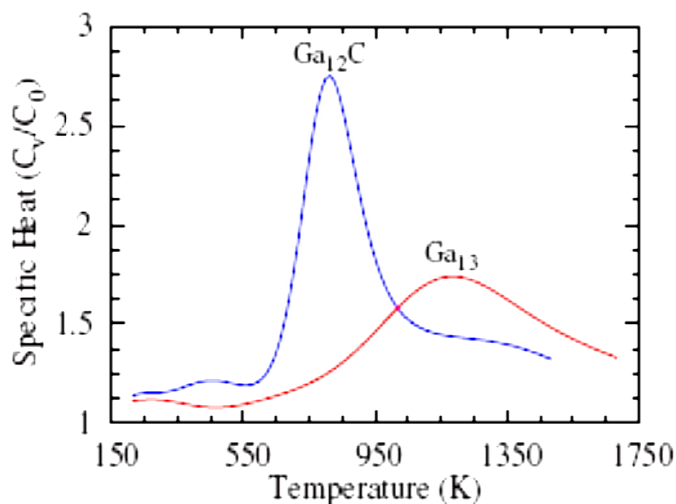


Figure 3.6 – Normalized specific heat for Ga₁₃ and Ga₁₂C. The Ga₁₂C is a sharp peak as compared to Ga₁₃

This feature can be understood in light of the change in the nature of the ground state geometry and the differences in the nature of bonding. Ga₁₂C is a well ordered structure, with all 12 Ga atoms placed at a spherical shell at 2.53Å from the center. In addition, all the nearest neighbor bond distances are the same. In contrast to this, Ga₁₃ is a distorted structure with the nearest neighbor bond lengths varying between 2.57 and 2.8Å. The manifestation of these differences can be seen in ELF as examined through their isosurfaces. We have examined the isosurfaces for these two clusters by continuously varying the isovalue, starting with the maximum of 0.9 down to 0.55. This enables us to locate the localized regions, locations of attractors, and the connectivity of these regions. There are 13 attractors centered on the atomic sites. In figure 3.7, we show the isosurface of ELF for both Ga₁₃ and Ga₁₂C at the value of 0.67. This is a critical value, at which the first merging of these regions takes place for Ga₁₂C. The most interesting aspect is that at this value, all the regions merge and contain all the atoms. This indicates that all the surface atoms experience a similar “environment” or bond with each other with similar strength, and hence, will “melt” together. In contrast to this, Ga₁₃ shows a fragmented structure (figure 3.7-(a)). The first merging of the regions establishing the connectivity is seen at a high value of ELF at 0.77. The process of merging continues as the ELF value is decreased. At a value of 0.72, we find five pairs of atoms connected to each other. This indicates that in Ga₁₃ a large number of pair of atoms are strongly bonded as compared to Ga₁₂C.

3. Carbon doped Al₁₃ and Ga₁₃ clusters

This is responsible for the higher melting temperature in this cluster. All the regions merge at a lower value of ELF 0.55. Figure 3.7 brings out this contrast and the fragmented nature of the regions. Thus, in Ga₁₃, most of the atoms experience a different environment and are bonded with the surrounding atoms with varying strength, which results in a broad transition region (or step by step bond breaking). A similar detailed analysis for Al₁₃ and Al₁₂C reveals that the contrast is not as significant since the symmetry remains the same in both clusters.

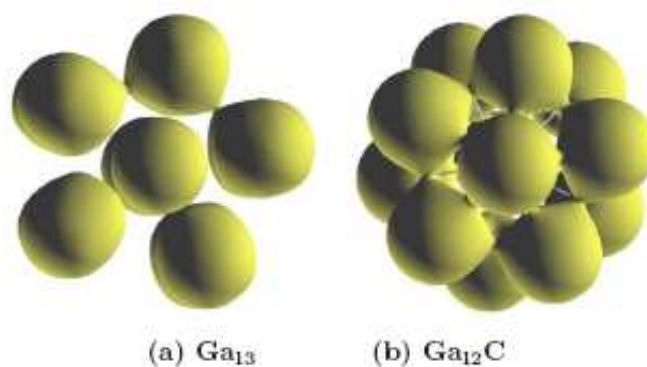


Figure 3.7 – Isosurfaces of ELF for Ga₁₃ and Ga₁₂C at the value of 0.67

The mean square displacements for the individual atoms bring out the difference between the Ga₁₃ and Ga₁₂C explicitly. Figure 3.8 shows MSD for both the clusters at 325 K. MSD at higher temperature show similar behavior. However, at lower temperatures, MSD prove to be a crucial indicator distinguishing the nature of the “motion” of atoms in these two clusters. It can be seen from figure that MSD for pure and doped clusters are significantly different at 325 K. At this temperature, there are a significant number of atoms in Ga₁₃ showing considerable displacements from their “original” positions, whereas in the case of Ga₁₂C, all the atoms have very small values. Remarkably, the atoms having large values of MSD in the case of Ga₁₃ belong to different basins.

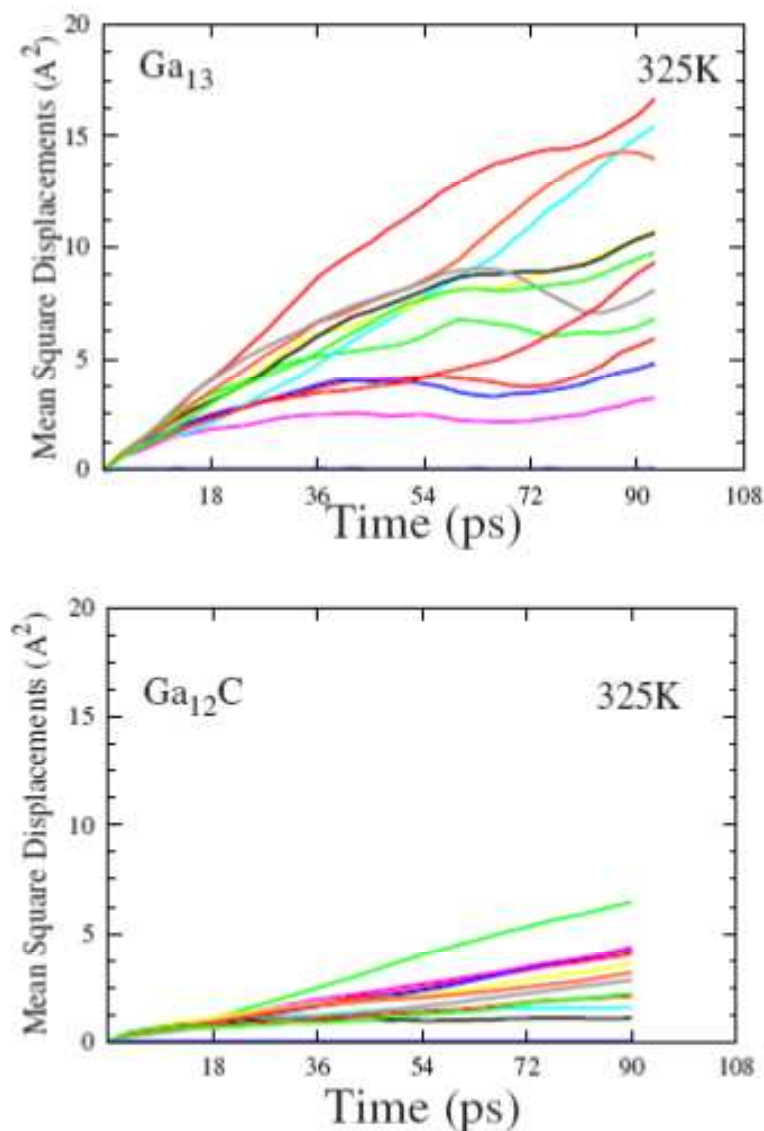


Figure 3.8 – Mean square displacement for Ga₁₃ and Ga₁₂C at 325 K. The MSD are shown for individual atoms.

The dynamics of the clusters can be described by examining the trajectories of atoms at various temperatures. It is observed that around 400 K, the Al₁₃ visits its first isomer, a decahedron, quite frequently. At 800 K, there is diffusive motion of the surface atoms. The central aluminum atom comes out at about 1200 K, but gets replaced by other aluminum atoms, retaining the shape of the cluster. This process continues up to 1800 K, where the shell structure is completely destroyed. The peak in the heat capacity curve is associated with the destruction of the icosahedron. Ga₁₃ also melts in a similar manner. It undergoes isomerization around 325 K from decahedron to icosahedron. At around 850 K, the central Ga atom comes out of the shell and gets replaced by another Ga atom. This process continues up to 1000 K. Around 1400 K,

3. Carbon doped Al₁₃ and Ga₁₃ clusters

the shell structure is completely destroyed and a peak occurs in the heat capacity curve. Thus, in pure clusters, the melting transition is a two step process. Isomerization is seen around 350 K, whereas the complete destruction of the shell structure is seen at a much higher temperature which is associated with the peak in the heat capacity curve. Impurity doped systems show a completely different behavior. In the case of Al₁₂C, there is no isomerization seen. Neither carbon atom nor surface atoms show any rigorous motion up to 700 K. Around 700 K, carbon is seen to diffuse on the surface, destroying the shell structure. Thus, the melting is a single step process. Unlike Al₁₂C, the surface atoms Ga₁₂C show significant motion around 325 K due to the isomerization from icosahedron to decahedron. The carbon atom, however, remains at the center up to 700 K. Melting is signified by carbon diffusing to the surface, followed by destruction of the shell. Again, melting is a single step process leading to a peak around 800 K. Thus, in both doped clusters, removal of the carbon from the center initiates the melting. The above observations are substantiated by the behavior of δ_{rms} of all these clusters. We have plotted the δ_{rms} for the central atom and the average for all the surface atoms in figure 3.9. The figure clearly brings out the difference in the motion of central atom and surface atoms. For all the clusters, the central atom does not show any appreciable rise in the value of δ_{rms} . Around 400K and above, all the clusters except for Al₁₂C show distinct movements of surface atoms, which are due to the isomerization observed around that temperature. Finally, we note an interesting aspect of our results. Although the carbon-doped clusters have higher BE (~5 eV), they melt at much lower temperatures. The enhanced BE is due to the complete filling of fivefold degenerate HOMO due to the addition of an extra electron, an effect observed not only for carbon but also for other tetravalent elements such as Si, Ge, Sn, etc. However, substitution of carbon at the center weakens the bonds between surface atoms. This initiates the melting process at much lower temperature. It may also be pointed out that BE is a measure of complete dissociation, while the process of melting does not change the number of electrons, retaining the close shell property.

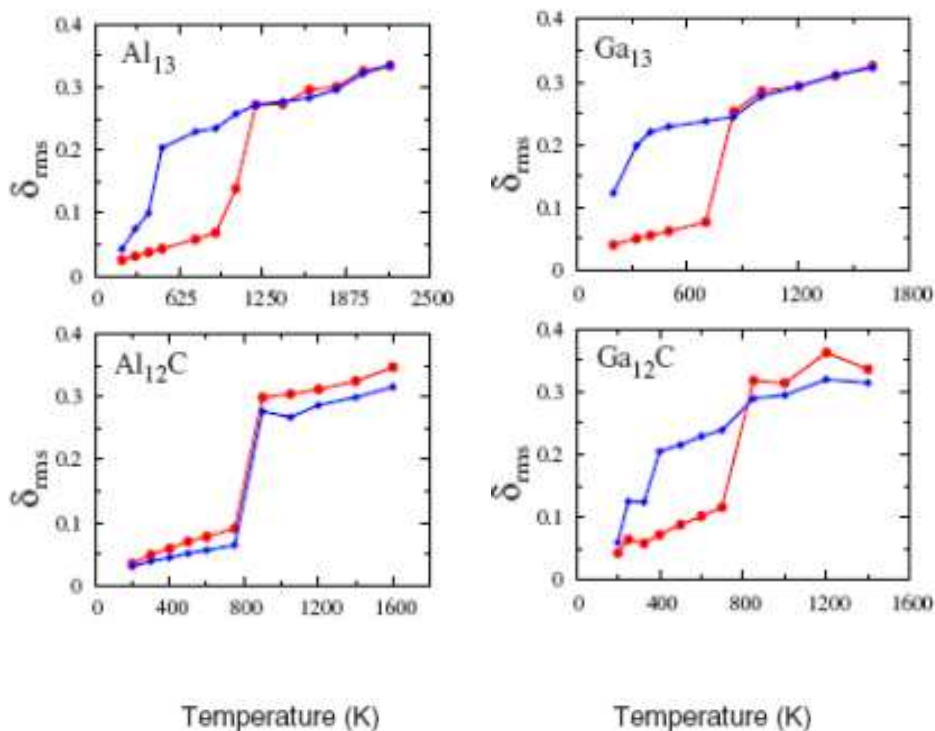


Figure 3.9 – δ_{rms} for surface atoms (filled circles, blue) and central atom (filled diamonds, red) for all the clusters averaged over 90ps.

3.4 SUMMARY AND CONCLUSIONS

We have carried out extensive first principle thermodynamics simulations for Al₁₃ and Ga₁₃ with and without substitution by single carbon impurity. Al₁₃ is known to be a distorted icosahedra with the al-al bond distance varying between 2.64-2.69Å. Upon doping, it changes to perfect icosahedra. Ga₁₃, on the other hand is a distorted decahedra with bond distance between 2.6-2.8Å. Interestingly, it also changes to perfect icosahedra upon doping. In both the doped clusters carbon occupies the central position at distance of 2.53Å from the surface atoms. The analysis of charge density and bonding shows that there is a partial charge transfer from the surface atoms to the central carbon in both the doped clusters. This results in weakening of the surface bonds and the size of the cluster shrinks. As a consequence there is a substantial reduction seen in the melting temperature of the doped clusters. Al₁₃ and Ga₁₃ melt at around 1800 K and 1200 K respectively while interestingly, both the doped clusters are seen to melt at around 800-900 K. Apart from the reduced in the melting temperature, carbon impurity is seen to induce a substantial change in the shape of the heat capacity curve in the case of Ga. The heat capacity curve for Ga₁₂C shows a

3. Carbon doped Al₁₃ and Ga₁₃ clusters

much sharper transition as compared to Ga₁₃. The origin of such sharp peak lies in the different bonding strengths of Ga₁₃ and Ga₁₂C. Our analysis of electron localization function clearly brings out this difference. In Ga₁₃, there are large number of pair of Ga atoms bonded to each other with similar bonding strength. As the clusters is heated, these pairs melt over range of temperature resulting in a broad specific heat curve. On the contrary, in Ga₁₂C is symmetric icosahedra with all 12 Ga atoms are bonded with same strength and hence melt together yielding a peak in specific heat curve. The examination of mean square displacements at low temperatures also show that in case of Ga₁₃, there are considerable number of atoms showing displacements from their mean position, while comparatively in Ga₁₂C, the value of MSD are less.

The close examination of the ionic trajectories and δ_{rms} show that both Al₁₃ and Ga₁₃ visit their isomers frequently at low temperature. Around 800 K the diffusive motion initiates and the central atoms comes out around 1200 K but gets replaced by the surface atom. The melting is signified by the destruction of the shell. In doped clusters, Ga₁₂C undergoes isomerization from icosahedra to decahedra. In both the doped clusters, the central carbon remains inside upto 700 K. Around 800 K, the central carbon comes out, the shell structure is destructed and cluster melts.

It is important to note the binding energy of the carbon-doped clusters, as noted in table 3.1, is higher by about 5eV. However, their melting temperatures are lower than the corresponding host cluster.

4. Stability of gold cages (Au_{16} and Au_{17}) at finite temperature

4.1 INTRODUCTION

In recent years gold nanoparticles have attracted much attention due to their vital role in nanoscale electronic, optical and medical diagnostic devices [268, 269]. One of the interesting applications of these clusters is in the area of catalysis. Gold in its bulk form is known to be a noble metal. But, gold in nanoregime has shown size-sensitive reactive properties and is considered to be a promising chemical catalyst [270, 271, 272]. Owing to such potential applications, a large amount of experimental [273, 274, 275] and theoretical [165, 166, 196, 276, 277, 278, 279] work probing structural and electronic properties of Au clusters has been reported. These reports reveal that the ground state (GS) geometries of gold clusters with sizes up to a few tens of atoms exhibit interesting and strikingly different trends. These undergo a very interesting structural evolution. There has been a debate about the size at which the planar to non-planar transition occurs [164, 276, 280]. A very recent experimental evidence of hollow cage structures [166] (for $n = 16, 17, 18$) analogous to C_{60} has generated an excitement and focused interest on gold clusters in this size range. Such hollow cages are predicted for larger sizes as well [281, 282] which opens up new possibilities of encapsulating impurities like transition metal atoms for tuning their properties [283, 284]. Almost all the studies reported so far on these cages pertain to zero temperature properties. Since the realistic applications are at finite temperatures, typically at room temperature and above, it is of considerable importance to investigate their stability and other properties at finite temperatures. In the present work we investigate the finite temperature behavior of two clusters, namely Au_{16} and Au_{17} , using *ab initio* method.

Finite temperature investigations of small clusters have brought out many interesting and at times counterintuitive facts [179, 176] which have been reviewed in Chapter 1. In nanoregime, there are two scales; the first one consists of a few hundreds to few thousands of atoms where the properties such as melting temperature

show the expected monotonic trend as a function of size of the cluster. However, in the size range of few tens to few hundreds of atoms the details of the electronic structure and the ground state geometry which could be quite different from the bulk can have significant influence on finite temperature properties.

There have been a few calculations reported on the finite temperature behavior of small gold clusters with classical molecular dynamics (MD) using parameterized potentials like Voter-Chen [285, 286]. However, these potentials are based on two-body or three-body interactions and fall short of mimicking the real scenario of many interacting electrons and ions. On the other hand, simulating finite temperature behavior with *ab initio* method is computationally very expensive. To the best of our knowledge, there are only two *ab initio* simulations reported so far. Soulé *et.al.* have simulated finite temperature behavior of gold clusters with 7, 13 and 20 atoms [287]. Krishnamurty *et. al.* carried out extensive first principles MD simulations to investigate finite temperature behavior of Au₁₉ and Au₂₀ [199]. The ground state geometry of Au₁₉ is the same as that of Au₂₀ except for the missing corner atom of the pyramid. Both the clusters melt around 780 K, a temperature much below the bulk melting temperature. However, Au₁₉ undergoes a vacancy-assisted melting transition leading to a broad peak in the heat capacity curve whereas Au₂₀ with a symmetric ground state has a well-defined peak in the heat capacity curve.

In the present work we have investigated the stability of Au₁₆ and Au₁₇ gold cages at finite temperatures. These are the smallest cages of gold clusters found so far. The capacity of these clusters to hold an atom inside the cage makes them technologically very interesting. The isomer distribution of these clusters reveals that the isomers of Au₁₇ are more symmetric than those of Au₁₆. Further, the isomer energy distribution of Au₁₆ is continuous whereas that of Au₁₇ shows gaps. Our simulations indicate that these cages are stable up to at least 850 K with Au₁₇ having a noticeable peak in the heat capacity curve and Au₁₆ with a broad transition region. In section 4.2 we briefly discuss the computational details. Results and discussion are presented in section 4.3. We conclude with summary in section 4.4.

4.2 COMPUTATIONAL DETAILS

All the calculations have been performed within the framework of *ab initio* density functional theory (DFT). We have employed the plane-wave method where the core-

valence interactions are described using Vanderbilt's ultrasoft pseudo-potentials [245] as implemented in the VASP package. It may be noted that pseudopotentials used in the plane-wave method incorporate the relativistic effects. For the purpose of calculating the equilibrium geometries, we have used generalized gradient approximation (GGA). The calculations have been carried out in two steps. In the first step we have obtained 50 distinct isomers for both the clusters. In order to get many distinct initial configurations for geometry optimization, constant temperature Born–Oppenheimer molecular dynamics (BOMD) runs were carried out at four different temperatures 300 K, 600 K, 900 K and 1200 K each with a time-scale of 60ps. Around 150 configurations were chosen from these initial runs by examining the potential energy as a function of time. The resulting isomers after minimization were examined visually as well as by carrying out the nearest neighbor bond length analysis so as to obtain geometrically distinct structures by removing the duplicates. Next, for calculating the heat capacities, BOMD simulations have been carried out for 14 different temperatures in the range of 200 K to 2000 K for Au₁₆ and 12 temperatures in the range of 200 K to 1600 K for Au₁₇. Each cluster is maintained at each temperature for a time period of at least 150ps using Noé thermostat [288]. For each of the temperature first 30ps of data are discarded for thermalization. Thus, the total simulation time is around 2.4ns. An energy cut-off of 179.7 eV is used for the plane-wave expansion of the wave function. We have used a convergence of 10^{-4} eV in the total energy during the self-consistency. The size of the simulation box is chosen to be 20Å which is found to be sufficient for the energy convergence. The data are used to calculate the ionic specific heat of each cluster using multiple histogram method (MH). The calculation of the heat capacity using the MH technique is sensitive to the number of temperatures at which the thermodynamic behavior of the cluster is simulated. The range and the number of temperatures are chosen to ensure an adequate overlap of the potential energy distribution. The MH method extracts the classical ionic density of states $\ln \Omega_C(E)$ of the cluster, or equivalently the classical ionic entropy $S = k \ln \Omega_C(E)$, from the simulation data. With $S(E)$ in hand, one can calculate the thermodynamic averages in a variety of ensembles. We have also calculated the mean square displacements (MSD), an important parameter for monitoring the phase change. The MSD of the cluster indicates the displacement of the ions with respect to their original positions as a function of time. Thus, one

expects MSD to converge to the square of the radius of the cluster when the system is in liquid-like region. We have also calculated the radial distribution function $[g(r)]$. It is defined as the average number of atoms within the region r and $r + dr$ from the centre of mass of the cluster. The radial distribution function for a symmetric cluster will exhibit distinct peaks at low temperatures corresponding to different shells. With increasing temperature these peaks are expected to broaden due to oscillatory motion of ions. Eventually, at high temperatures, there will be a merger of these peaks indicating the diffusive motion of ions.

4.3 RESULTS AND DISCUSSIONS

We begin our discussion by noting the ground state geometries and some low-lying isomers of Au_{16} and Au_{17} which are shown in figures 4.1 and 4.2 respectively. It may be pointed out that the ground state of Au_{16} and Au_{16}^- have been reported and are known to be different from each other [166, 289]. The ground state geometry of neutral cluster is a symmetric flat cage while that of anionic cluster is a hollow cage. Our results agree with those reported in the literature. Since the isomers at various energies are relevant to the finite temperature analysis, we have analyzed about 50 distinct isomers within the energy range of 0.4 eV above the ground state energy. These isomers can be approximately grouped into three categories. The low energy isomers (within 0.1 eV with respect to the ground state) are characterized by the flat cage structures (figures 4.1-(a)–(c)). These structures differ from the ground state with respect to their base and capping. The next in the energy scale (from 0.11 to 0.15 eV with respect to the ground state) are the hollow cages which are characterized by the existence of two six-membered distorted rings arranged nearly parallel to each other (figures 4.1-(d) and 4.1-(e)). These rings give rise to a hollow cage-like structure. Typically, these structures do not display any definite symmetry and once again the isomers in this class differ by the nature of the caps on these rings and small distortions. Lastly, still higher in the energy scale (above 0.16 eV with respect to the ground state) are the intermediate structures between the above two as shown in figures 4.1-(f)–(h).

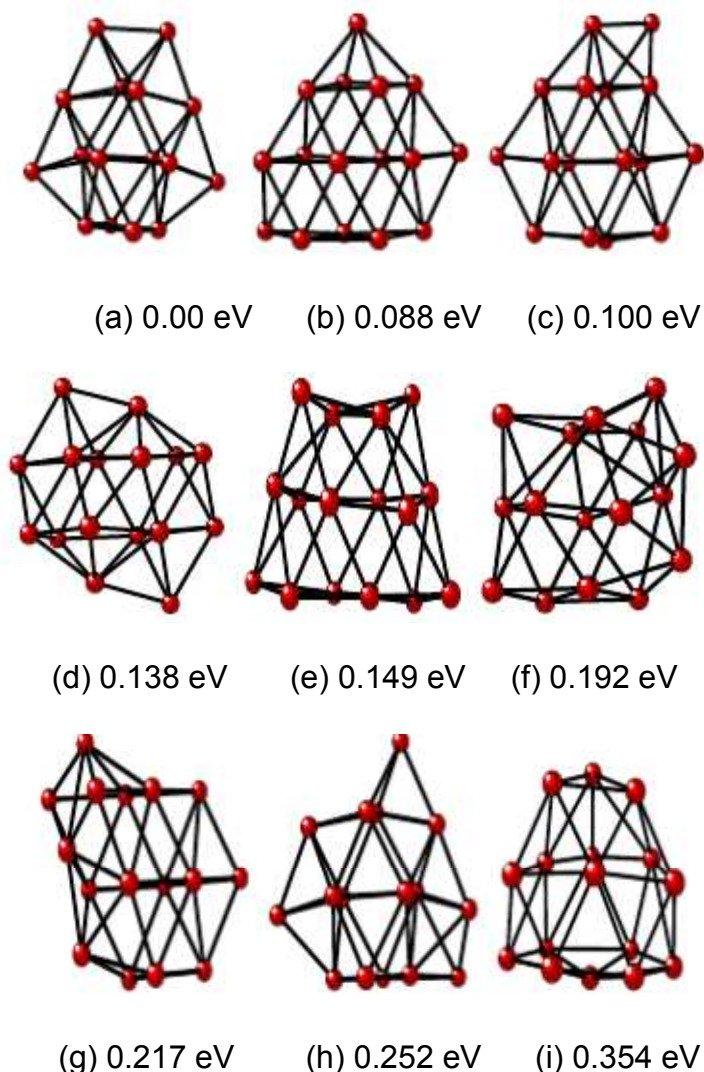


Figure 4.1 –The ground state geometries and various isomers of Au_{16} . The numbers correspond to the difference in the energy with respect to the ground state.

Most of these have only one five or six-membered ring. We also note the existence of a highly symmetric hollow cage (figure 4.1-(i)) which is known to be the ground state of Au_{16}^- . This isomer has an energy which is about 0.35 eV higher with respect to the ground state. Indeed this isomer is observed in our simulations at around 850 K. Another significant characteristic of these isomers is their energy distribution which turns out to be almost continuous. We will discuss its possible effect on the nature of the heat capacity curve and contrast its behavior with that of Au_{17} .

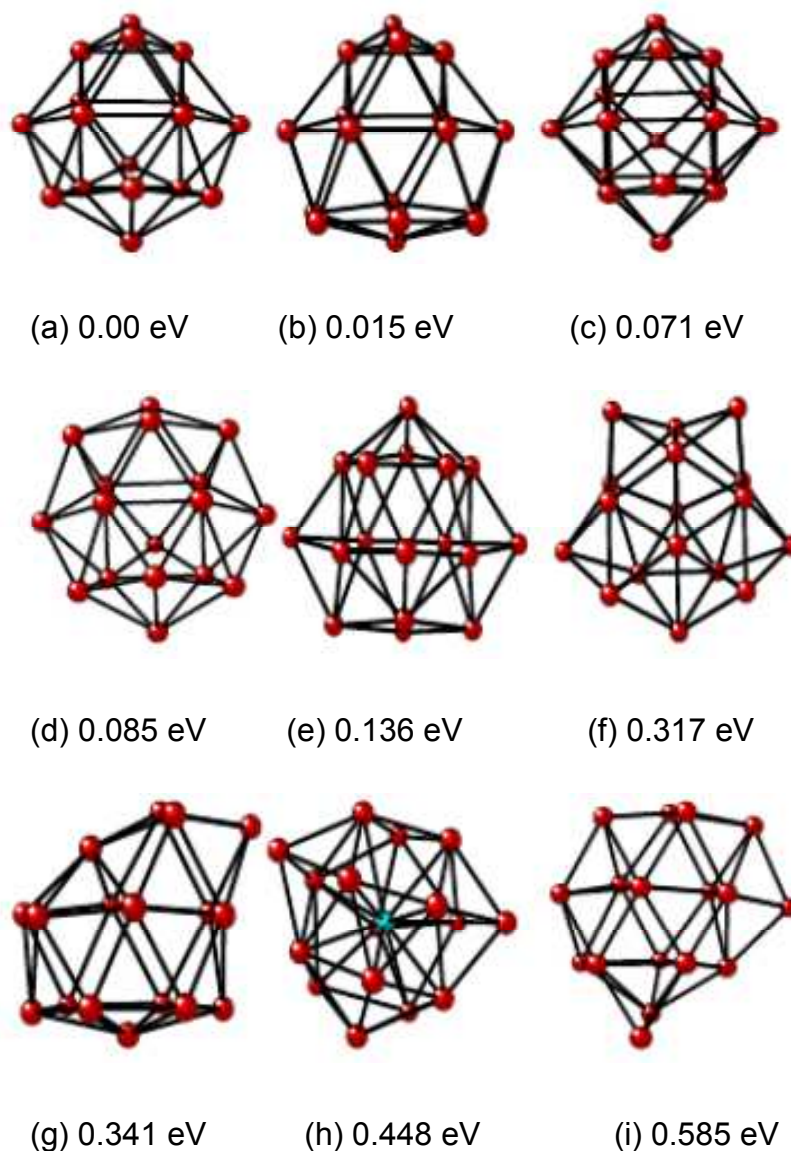


Figure 4.2 –The ground state geometries and various isomers of Au_{17} . The numbers correspond to the difference in the energy with respect to the ground state.

In contrast to Au_{16} , the ground state of Au_{17} exhibits a hollow cage structure. In fact there are two nearly degenerate geometries (very close in energy ≈ 0.01 eV) which are the probable candidates for the ground state as shown in figures 4.2-(a) and 4.2-(b) respectively. While one of the structures has two pentagons stacked over each other and three distinct atomic caps, the other one has a six-membered ring at the centre. Figures 4.2-(c) and 4.2-(d) show the next low-lying isomers which are also hollow cages higher in energy by 0.07 eV. In figure 4.2-(e) we show a caged structure which is slightly distorted while figures 4.2-(f) and 4.2-(g) represent high energy cages with energy around 0.35 eV. Interestingly, none of the structures discussed so far have a

gold atom trapped inside. In figure 4.2-(h) a high energy isomer with such a trapped atom is seen. This isomer occurs at 0.47 eV higher in energy with respect to the lowest energy structure. The noteworthy point is that the isomers even up to a typical energy of 0.35 eV consist of predominantly hollow cages, either symmetric or distorted.

We now present the calculated ionic specific heats in figure 4.3. It is clear from the figure that both Au_{16} and Au_{17} show a rather broad heat capacity curve with some notable differences. Au_{16} shows solid-to-liquid transition from 600 K to 1000 K. In contrast, Au_{17} shows a weak shoulder at 500 K and a noticeable peak at 900 K. This peak may be identified as the melting peak. Typically in the finite size systems, melting temperature is not sharp. At low temperatures, it is easy to characterize the cluster as solid-like, where the atoms execute small oscillatory motion. In this region MSD are small. The other extreme is the liquid-like state where there is a clear diffusive motion of the atoms throughout the cluster. The MSD in this region are of the order of square of the radius of the cluster and tend to saturate. The transition region around the melting peak cannot be definitely characterized as solid-like or liquid-like. In general, as the temperature increases, the pre-melting features can occur due to the isomerization or in some cases surface melting.

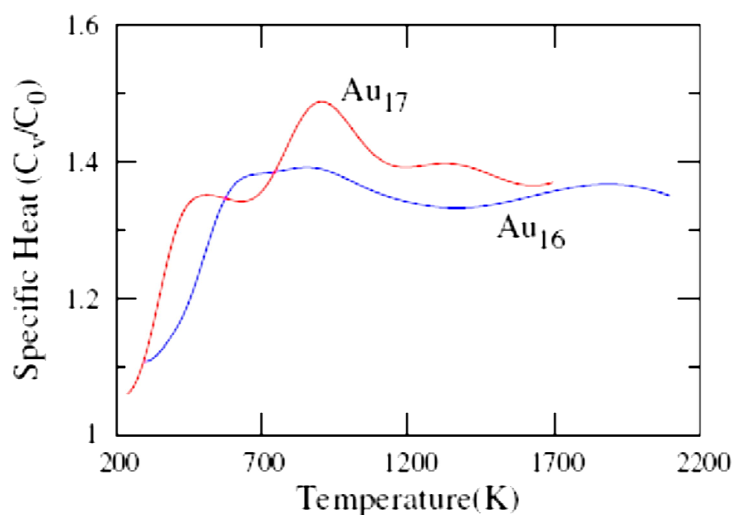
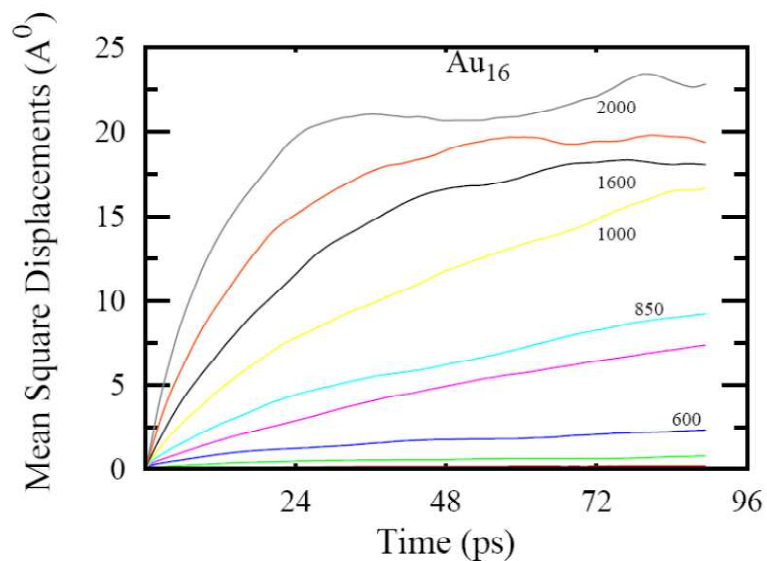
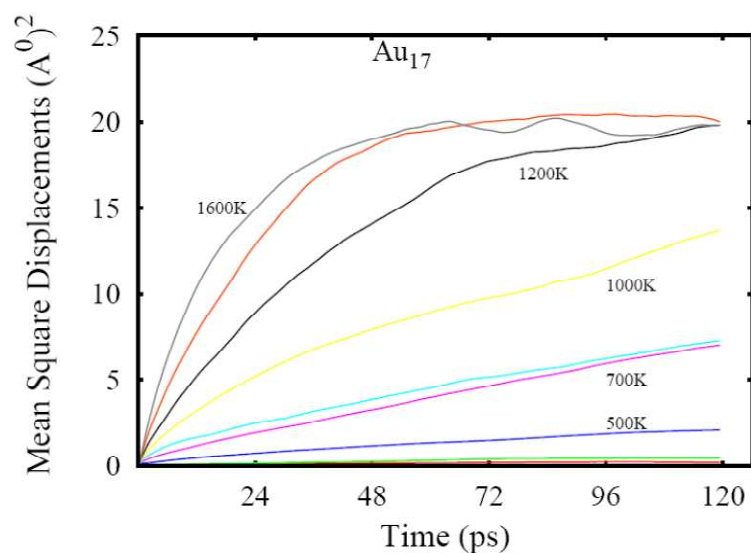


Figure 4.3 – Normalized specific heat for Au_{16} and Au_{17} .

In order to make a detailed analysis of the ionic motion we examine the atomic trajectories in the form of movies. It is observed that at low temperatures (up to 400

K), Au₁₆ cluster is seen to visit the first isomer (figure 4.1-(b)) quite frequently. Further, up to 600 K, in addition to the first isomer, the next low energy structures (figures 4.1-(c) and 4.1-(d)) are also observed. Thus, up to this temperature the cluster moves through either flat or hollow caged isomers. Around 700 K, the cage pattern is seen to be disturbed and a diffusive motion of the atoms results in a high energy distorted flat cage structure (figure 4.1-(h)). Such distortions are retained till 900 K above which the cluster is seen to melt. MSD at 1000 K and onwards are seen to reach about the square of the cluster radius as shown in figure 4.4. Thus, from 600 K onwards the movie reveals that the cluster is dominated by isomerization from flat cages to hollow ones and again to distorted flat type. The process continues even above the melting temperature.

For Au₁₇, a weak shoulder at 500 K can be attributed to isomerization. Up to 800 K, the shape of the cluster remains more or less cage-like in spite of distortions. However, we do not observe a complete destruction of the cage. The motion clearly indicates the dominance of isomers in the sense that at least up to 1000 K many isomers belonging to hollow or distorted type of cages are observed. It is only above 1000 K or so, we observe the open structures and consequently, complete destruction of cages. Indeed, around this temperature the MSD reach the value of 15\AA^2 as shown in figure 4.5. A significant observation that emerges from our studies is that the cage structure is very stable and retains its shape at least till 1000 K resulting into a heat capacity curve with relatively sharper peak.

Figure 4.4- Mean square displacements of Au_{16} over 120 ps.Figure 4.5- Mean square displacements of Au_{17} over 120 ps.

The stability of the hollow cages can be established by calculating the radial distribution functions at various temperatures. In figure 4.6 we show the radial distribution function for Au_{17} . It shows three prominent peaks even up to 500 K, corresponding to the three shells indicating the existence of the cage structure. At 600 K, the three shells merge into two, indicating a diffusive motion of ions within the shell. This shell structure is retained up to 850 K. Around melting temperature, that is

4. Gold cages

≈ 1000 K, these two peaks are seen to merge into a single one. The figure also clearly reveals that there are no atoms within the radius of about 2.0\AA .

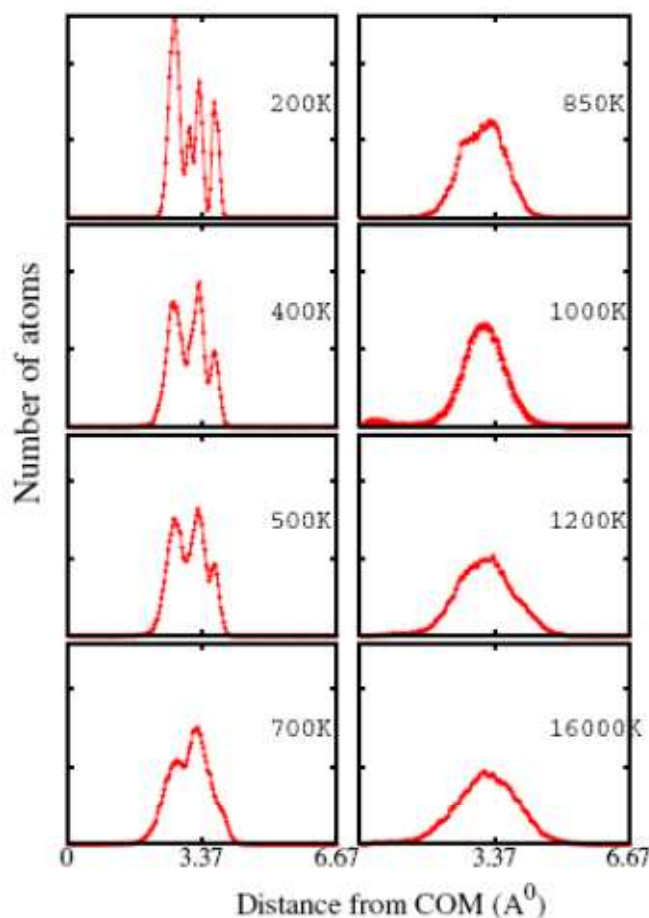


Figure 4.6 - Radial distribution function of Au_{17} .

Now we turn to examine the isomer energy distribution as shown in figure 4.7 and its influence on the specific heat. The significance and relationship between the nature of the isomer energy distribution and the shape of the heat capacity curve has been discussed by Bixon and Jortner [290]. It can be seen from figure 4.7 that the isomer distribution of Au_{16} is relatively continuous while Au_{17} shows a step-like structure or more precisely multiple bunched level structure. As discussed by Bixon and Jortner, such a structure leads to hierarchical isomerization which is seen as a weak shoulder in the specific heat curve of Au_{17} . In the case of systems exhibiting gapless spectra (such as Au_{16}) there is no clear transition in caloric curve and that leads to a relatively broad specific heat curve. It is interesting to note that the ordered structures normally lead the isomer energy distribution having gaps. In the case of disordered ground

states, a minor rearrangement of the atoms gives rise to many nearly degenerate isomers leading to an almost continuous spectrum [193, 267, 291].

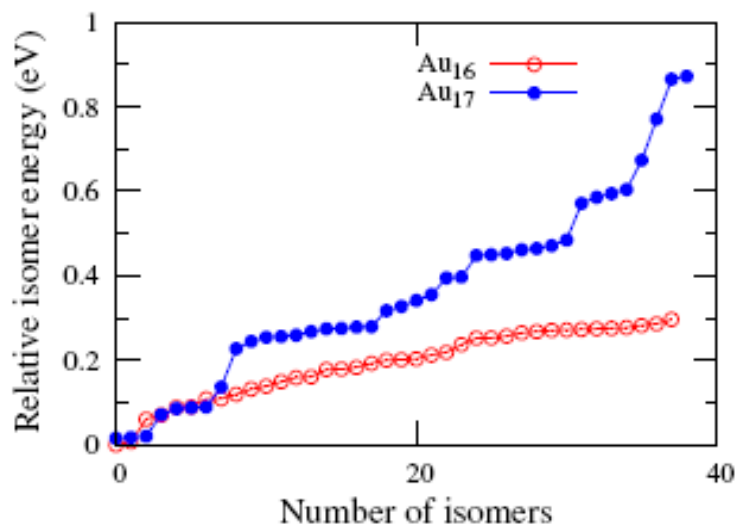


Figure 4.7- The distribution of isomer energies for Au₁₆ and Au₁₇.

Finally, we compare the specific heats of these two clusters with those of Au₁₉ and Au₂₀. [199] It may be recalled that a highly symmetric Au₂₀ cluster shows a sharp melting peak at around 770 K while Au₁₉ having one vacancy (the missing apex atom of the pyramid) has a broad peak. In contrast with Au₂₀ both the clusters here show rather broad specific heat curves. This is consistent with the fact that the ground state of Au₂₀ is highly symmetric while both Au₁₆ and Au₁₇ are relatively disordered. Although Au₁₉ retains the symmetry, the broad specific heat curve has been attributed to the vacancy, i.e. the absence of vertex atom.

4.4 SUMMARY AND CONCLUSIONS

We have carried out finite temperature simulations of the smallest gold cages of gold, namely Au₁₆ and Au₁₇ using *ab initio* density functional molecular dynamics. Au₁₆ is a flat cage while Au₁₇ shows a hollow caged structure. These results are in agreement with the earlier results. Next, we have extensively analyzed about 50 different isomers for both the cages. These isomers are observed at about 0.4 eV above the ground state energy. The isomers have been identified and categorized on the basis of their structural variation. The isomer analysis plays a crucial role in the finite temperature properties. Our calculated heat capacity curves show that both the clusters show rather

broad curve with few notable differences. Au_{16} shows solid-liquid transition from 600-1000 K, while Au_{17} shows a noticeable peak at 900 K. A weak shoulder seen at 500 K is attributed to isomerization. The careful observation of the ionic trajectories shows that Au_{16} visits number of isomers upto 600 K after which the cage structure is disturbed and diffusive motion is seen. Such distortions are retained till 900 K above which the cluster is seen to melt. Au_{17} on the contrary, remains stable up to 1000 K. Upto 1000 K; it visits number of isomers but retains the cage structure in spite of the distortions. It is only above 1000 K, we get open structure indicating the melting.

The isomer energy distribution has a close association with the nature of the heat capacity curve. For Au_{16} the continuous isomer energy distribution leads to a broad peak ranging from 600 K to 1000 K. In case of Au_{17} a step-like energy distribution gives a relatively sharper peak.

5. A Systematic study of electronic structure from Graphene to Graphane

5.1 INTRODUCTION

Carbon is regarded as one of the most versatile elements in the periodic table, forming a wide variety of structures such as three-dimensional sp^3 bonded solids like diamond; sp^2 hybridized two-dimensional systems like graphene and novel nanostructures like fullerenes and nanotubes. The electronic structure and the physical properties of these carbon-based materials turn out to be exotic [292]. Although the existence and the properties of the three-dimensional allotrope, graphite, containing weakly coupled stacks of graphene layers were well known [33], the experimental realization of a monolayer, graphene, brought forth a completely different set of novel properties [293, 294]. The triangular bipartite lattice of graphene leads to an electronic structure having a linear dispersion at the Dirac points. The low energy behavior of such two-dimensional electrons in graphene has been a subject of intense experimental and theoretical activity exploring the electronic, magnetic, mechanical and transport properties, etc. For a recent review the reader is referred to Castro Neto *et. al.* [295].

Although graphene is considered as a prime candidate for many applications, the absence of a bandgap is a worrisome feature for the application to solid state electronic devices. In the past, several routes have been proposed to open a band gap [296, 297, 298]. The most interesting one is the recent discovery of a completely hydrogenated graphene sheet named as *graphane*. *Graphane* was first predicted by Sofo *et. al.* [20] on the basis of electronic structure calculations and has been recently synthesized by Elias *et. al.* [21]. The experimental work also showed that the process of hydrogenation is reversible, making *graphane* a potential candidate for hydrogen storage systems. Since upon hydrogenation, graphene, a semi-metal, turns into an insulator, it is a good candidate for investigating the nature of the metal–insulator transition (MIT).

There are few reports investigating the electronic structure of graphene sheets as a function of hydrogen coverage leading to the opening of a band gap. Most of these are restricted to a small number of hydrogen atoms. The electronic structure of hydrogen adsorbed on graphene has been investigated using density functional theory (DFT) by Boukhvalov *et. al.* [23] and Casolo *et. al.* [24]. Their results support the possibility of using graphene for the hydrogen storage. Their work also shows that the thermodynamically and kinetically favored structures are those that minimize the sublattice imbalance. Flores *et. al.* have investigated the role of hydrogen frustration in *graphane*-like structures using *ab initio* methods and reactive classical molecular dynamics [299]. The stability trends in small clusters of hydrogen on graphene have been discussed in a review by Toman *et.al.* [300]. A recent work by Zhou *et. al.* [27] predicted a new ordered ferromagnetic state obtained by removing hydrogen atoms from one side of the plane of *graphane*. Recently, Wu *et.al.* [301] have reported implications of selective hydrogenation by designing an array of triangular carbon domains separated by hydrogenated strips. The electronic structure of the interface between graphene and the hydrogenated part has been investigated by Schmidt and Loss [302]. They show the existence of edge states for a zigzag interface having a strong spin-orbit interaction. An interesting experimental work using scanning tunneling microscopy by Hornekaer *et.al.* [303, 304] demonstrates clustering of hydrogen atoms on a graphite surface. The work shows that there is a vanishingly small adsorption barrier for hydrogen in the vicinity of already adsorbed hydrogen atoms. The question of the effect of the defect on the electronic structure of atomic hydrogen has been addressed by Duplock *et. al.* [53] within density functional theory. They show that the electronic gap state associated with the adsorbed hydrogen is very sensitive to the presence of defects such as Stone-Wales defects. The localization behavior of disordered graphene by hydrogenation has been reported within the tight binding formalism [28]. The potential of hydrogenated graphene nanoribbons for spintronics applications has been investigated within DFT by Soriano *et.al.* [305]. The defect and disorder induced magnetism in graphene (including adsorbed hydrogen as a defect) has been studied by Yazyev and Helm mainly using Hubbard Hamiltonian and DFT [306, 307, 308]. Theoretical investigations have also been carried out for a single hydrogen defect on a *graphane* sheet using the GW method [22], and for one and two vacancies in *graphane* [309] using DFT. It has been shown that interaction

between adatoms in hydrogenated graphene is long range and its nature is dependent on which sub lattice the adatoms reside in [310]. These results also suggest that the adatoms tend to aggregate. A very recent work by Singh *et.al.* explores the formation of quantum dots as a small island of graphene in a *graphane* host [311].

In the present work, we investigate some aspects of graphene–*graphane* transition by probing the electronic structure of hydrogenated graphene. The objective of our work is to understand the evolution of the electronic structure upon hydrogenation and gain some insight into the way bandgap opens. Therefore we have carried out extensive calculations for eighteen different hydrogen coverages between graphene (0% hydrogen coverage) and *graphane* (100% hydrogen coverage) within the framework of DFT. Our results suggest that the hydrogenation in graphene takes place via clustering of hydrogens. Analysis based on density of states (DOS) indicates that before the gap opens (as a function of hydrogen coverage) the hydrogenated graphene sheet acquires a metallic character. This metallic state is spatially inhomogeneous in the sense; it consists of insulating regions of hydrogenated carbon atoms surrounded by the conducting channels formed by the bare carbon atoms. We also show that it is possible to tune the electronic structure by the selective decoration of hydrogen atoms to achieve semiconducting or metallic state.

5.2 COMPUTATIONAL DETAILS

The calculations have been performed using a plane-wave projector augmented wave method based code, VASP [261]. The generalized gradient approximation as proposed by Perdew, Burke and Ernzerhof [312] has been used for the exchange–correlation potential. The convergence of binding energies with respect to the size of the supercell has been checked using three different sizes, viz., 5×5 , 6×6 and 7×7 containing 50, 72 and 98 carbon atoms for the case of 50% hydrogen coverage. The binding energy per atom changes by about 0.05 eV (a percentage change of 0.06%) in going from 5×5 to 7×7 . Therefore we have chosen a 5×5 unit cell for the coverage up to 50% of hydrogen and 6×6 for the higher coverages. This choice is consistent with the one used by Lebègue *et. al.* [22]. In order to obtain adequate convergence in the density of states, we have carried out calculations on different k grids. It was found that at least 9×9 k grid was required during geometry optimization for an acceptable convergence. However, a minimum of 17×17 k grid was necessary for

obtaining an accurate DOS. The convergence criterion used for the total energy and the force are 10^{-5} eV and 0.005 eV/Å respectively. All the calculations have been performed on the chair conformer configuration where hydrogen atoms are attached to carbon atoms alternatively on opposite sides of the plane. This is known to be a lower energy configuration as compared to the boat conformer [20, 22].

5.3 RESULTS AND DISCUSSIONS

In order to decide the minimum energy positions for hydrogen atoms, following procedure has been adopted. Up to 20% coverage of hydrogen, we have carried out the geometry optimization for two different configurations of hydrogen atoms, first by placing the hydrogen atoms randomly and second by placing the hydrogen atoms contiguously, so as to form a compact cluster of hydrogenated carbon atoms. It turns out that, in all the cases, the configuration forming the compact cluster of the hydrogen atoms is energetically favored. In order to assess the relative stability of different patterns we have calculated six different patterns for 20% coverage case as shown in table 5.1. The binding energy of the most stable structure is the reference level. The more negative binding energy means more unstable structure.

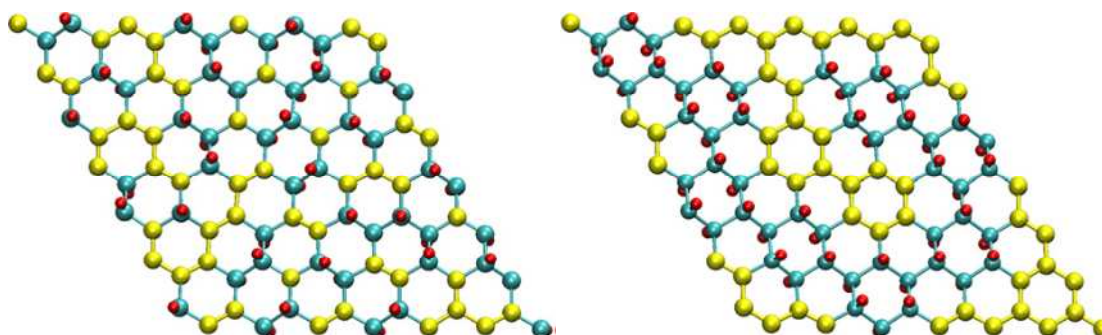
20% hydrogen coverage	
Configuration	BE (total cell) eV
Random placement of hydrogens	-9.32
Five hydrogen pairs placed separately	-4.29
Hydrogens placed along the diagonal of the cell	-2.85
Two clusters of seven and three hydrogens	-2.15
A single hydrogen isolated from a cluster of nine hydrogens	-1.77
One compact cluster	0.00

Table 5.1 - Shifted binding energies (BE) for different configuration of 20% coverage (10H + 50C). The binding energy of the most stable structure is the reference (zero) level. The more negative binding means more unstable structure.

We note that the compact cluster configuration is the lowest in energy and is lower by 0.9 eV/H atom compared to the energy of the configuration with randomly placed hydrogen atoms. Thus our geometry optimization shows a preference for hydrogens to

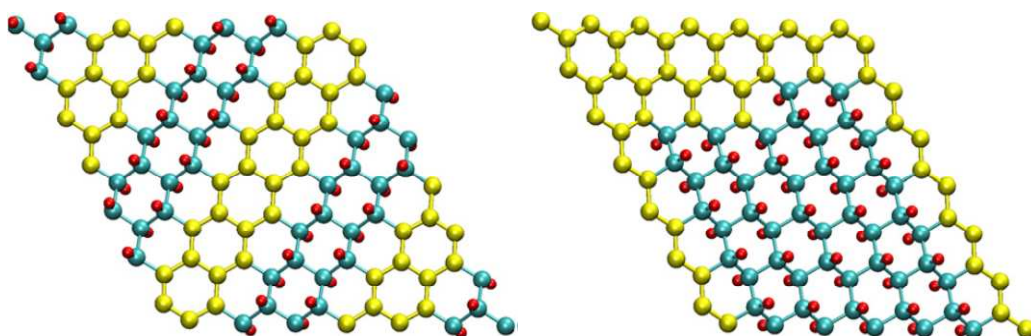
5. Electronic structure of graphene and *graphane*

decorate the graphene lattice in a contiguous and compact manner. In order to assess the validity of this process for the larger coverages and to understand the influence of different edge patterns like zigzag and armchair, we have considered seven different patterns for 50% coverage, as shown in figure 5.1.



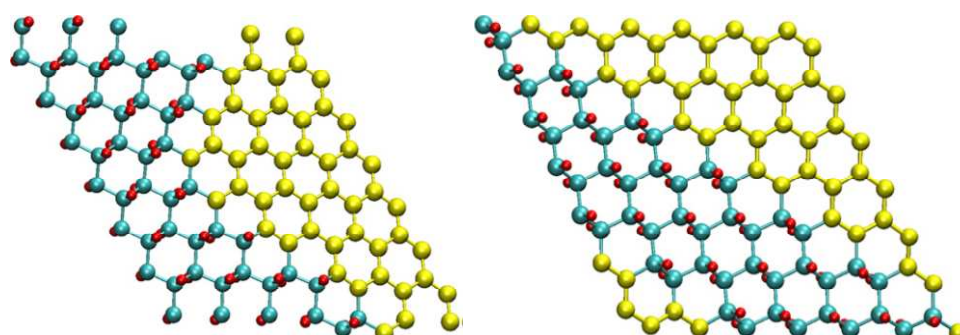
(a) Randomly placed H

(b) Chain of bare carbons



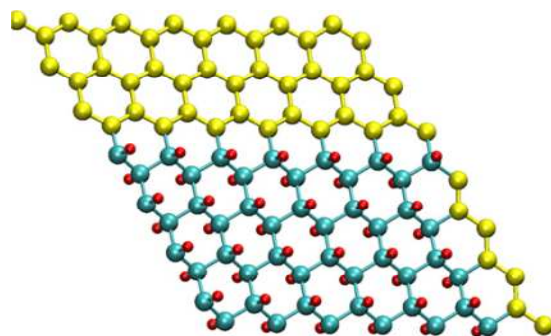
(c) 3 Separated islands

(d) Single cluster with Z-interface



(e) A and Z mixture

(f) Zigzag cluster



(g) A compact cluster

Figure 5.1 – Different hydrogen decorations for 50% concentration. In the figure, yellow (lightly shaded in print) balls are bare carbon atoms, turquoise (darker shades in print) balls are hydrogenated carbons and red (small dark in print) balls are hydrogen atoms.

These calculations have been carried out on a larger unit cell containing 98 atoms of carbon. Although a compact cluster configuration is energetically preferred one, there are different ways in which the hydrogens can be placed yielding a compact geometry. The seven cases considered are: 1- randomly distributed hydrogens (figure 5.1-(a)), 2- a chain of bare carbon atoms (figure 5.1-(b)), 3- three separated clusters as shown in (figure 5.1-(c)), 4- a single cluster having zigzag interface and with one line of bare carbon atoms at the two side edges (figure 5.1-(d)), 5- a mixture of armchair and zigzag pattern at the interface (figure 5.1-(e)), 6- a armchair pattern at the interface (figures 5.1-(f)) and 7- a zigzag pattern at the interface (figure 5.1-(g)). In the zigzag case each hexagonal ring at the edge has three hydrogenated carbons and three empty carbons. An armchair pattern consists of only two hydrogenated carbons at the edge. The binding energies for all these seven structures are compared in the table 5.2. Even among the islands, the ‘most compact’ one (having minimum surface area of covered hydrogens) has the highest binding energy. By the most compact, we mean an island of hydrogenated carbons which covers the minimum area. We have discussed more details about the zigzag and arm chair patterned configurations in section.

50% hydrogen coverage on 98 carbon cell	
Configuration	BE (total cell) (eV)
Random placement of hydrogens	-23.29
Chain of connecting bare carbon atoms	-3.65
Three separated islands	-3.25
Zigzag interface with a line of bare carbon atoms at the two side edges	-2.46
Compact mixed (zigzag & armchair) interface	-1.66
Compact armchair interface	-1.43
Compact zigzag interface	0.0

Table 5.2 - Shifted binding energies (BE) for different configuration of 50% coverage as shown in figure 4.1. The binding energy of the most stable structure is the reference (zero) level. The more negative binding energy means more unstable structure.

The tendency to form the compact cluster can be understood by noting that the hydrogen atom placed on the top of a bare carbon atom pulls up the carbon atom above the plane by 0.33Å and deforms the surrounding lattice points also. Therefore it costs less energy to place an extra hydrogen atom nearest to the existing cluster, since the number of strained bonds are less compared to the case where the hydrogen atom is placed away from the cluster. In the latter case the entire neighborhood is deformed. Our results are consistent with the work of Hornekaer *et. al.* [303]

We have also carried out a similar analysis for the case of four hydrogen vacancies in *graphane*. The calculations for various configurations have been carried out with spin polarization. The calculated binding energies and the magnetic moments are tabulated in table 5.3. The four configurations considered are (1) four hydrogen atoms removed randomly, (2) three hydrogen atoms removed from one hexagon and 1 from other, (3) two hydrogen atom pairs removed from different hexagons and (4) four hydrogens removed from a single hexagon (compact). We observe that the structure having a compact form of vacancies has the highest binding energy. The magnetic moment is about two for the lattice imbalance case. It is fruitful to recall Lieb's theorem which states that for a bipartite lattice (one electron per site) the spin S of the ground state is $\frac{1}{2} * (\text{the lattice imbalance})$ [313]. The magnetic moment seen in

5. Electronic structure of graphene and *graphane*

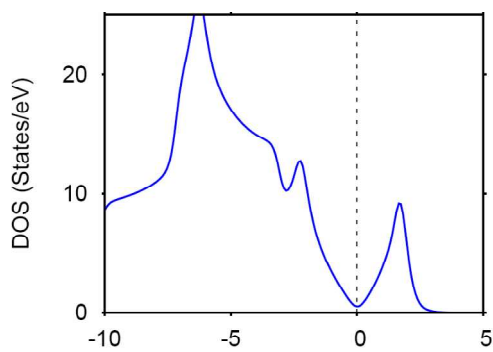
the case of random placement is just the sum of the isolated moments of hydrogen atoms, essentially a non-interacting case.

92% hydrogen coverage (4 vacancies)		
Configuration	BE (total cell)	Magnetic Moment
Random	-5.50	4.0
3H on one hexagon and 1on other	-2.09	1.82
2H pairs placed on different hexagons	-0.11	nil
Compact single island	0.0	nil

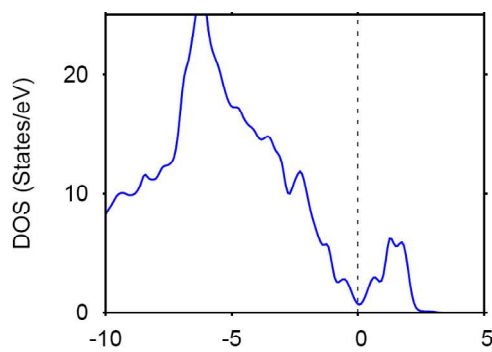
Table 5.3 - Shifted binding energies (BE) (eV) and the magnetic moments (μ_B) of four hydrogen vacancies. The binding energy of the most stable structure is the reference (zero) level. The more negative binding energy means more unstable structure.

Now we discuss the total DOS for different hydrogen coverages which are shown in figures 5.2 and 5.3. All the DOS are for the non-spin polarized cases. The geometry used is for the minimum energy configuration (compact cluster of hydrogen atoms). In both the figures the plots are shown in a restricted region to enhance the clarity near the Fermi energy. The effect of addition of a small concentration of hydrogen in the V-shape DOS near E_f can be seen from figures 5.2-(b) to (d). It can be noted that the characteristic V-shape valley seen in figure 5.2-(a) is due to peculiar sp^2 bonded carbon atoms in graphene, and the producing the deformation in the DOS. Thus in this region, the addition of hydrogen atoms immediately distorts the symmetry DOS is modified by additional localized σ -pz bonds between the hydrogen and carbon.

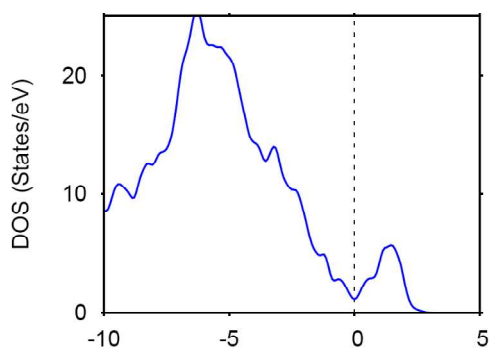
5. Electronic structure of graphene and *graphane*



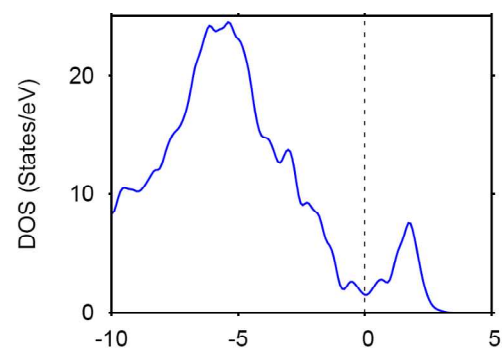
(a)



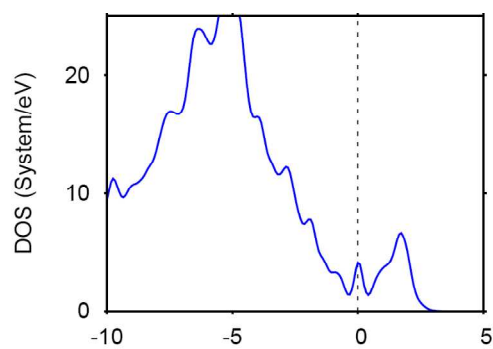
(b)



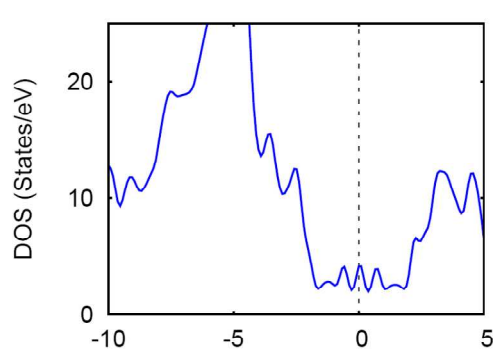
(c)



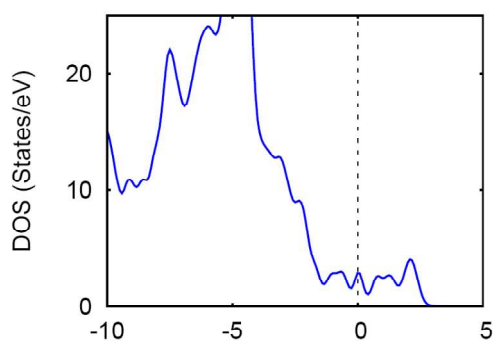
(d)



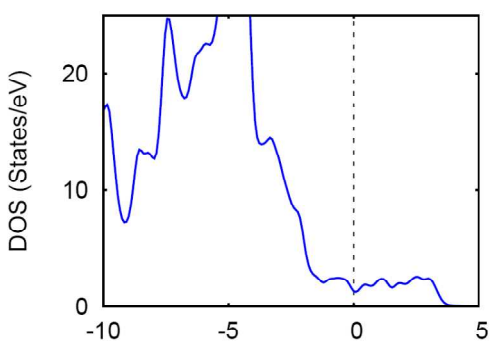
(e)



(f)



(g)



(h)

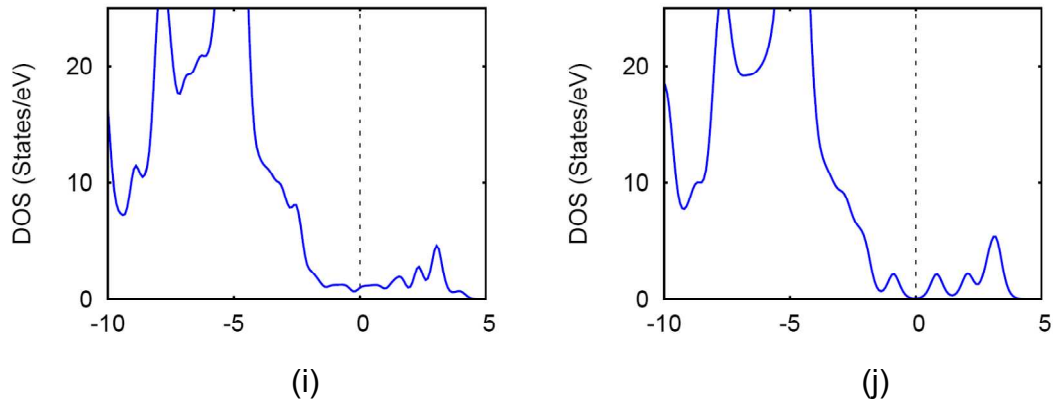


Figure 5.2 - The total DOS for hydrogenated graphene for various hydrogen concentrations below 90%. The zero of the energy is taken at the Fermi level and is marked by a vertical line. X axis denotes $E - E_f$. (a) Graphene; (b) 4% hydrogen; (c) 16% hydrogen; (d) 20% hydrogen; (e) 30% hydrogen; (f) 50% hydrogen; (g) 60% hydrogen; (h) 70% hydrogen; (i) 80% hydrogen; (j) 85% hydrogen.

As the hydrogen coverage increases there is a significant increase in the value of DOS at the Fermi level. The process of hydrogenation is accompanied by the change in the geometry. The hydrogenated carbon atoms are now moved out of the graphene plane, in turn the lattice is distorted and the symmetry is broken. As a consequence, more and more \mathbf{k} points in the Brillouin zone contribute to the DOS near Fermi level, the increase being rather sharp after 20% coverage. The region ranging from 30% coverage to about 60% coverage is characterized by the finite DOS of the order of 2.5 eV^{-1} near the Fermi energy. As we shall discuss this region can be described as having metallic character with delocalized charge density.

Now we complete the discussion of DOS by presenting the cases of hydrogen coverages greater than 90%. In figure 5.3 we show the density of states obtained by the removal of one–four hydrogen atoms in a unit cell containing fifty carbon atoms. Clearly one and three hydrogen vacancies (i.e. 98% hydrogen and 94% hydrogen respectively) induce states on the Fermi level while two and four hydrogen vacancies (i.e. 96% hydrogen and 92% hydrogen respectively) do not induce any state at the Fermi level (see the discussion of hydrogen imbalance later). For a small number of vacancies these are π bonded states localized on bare carbon atoms.

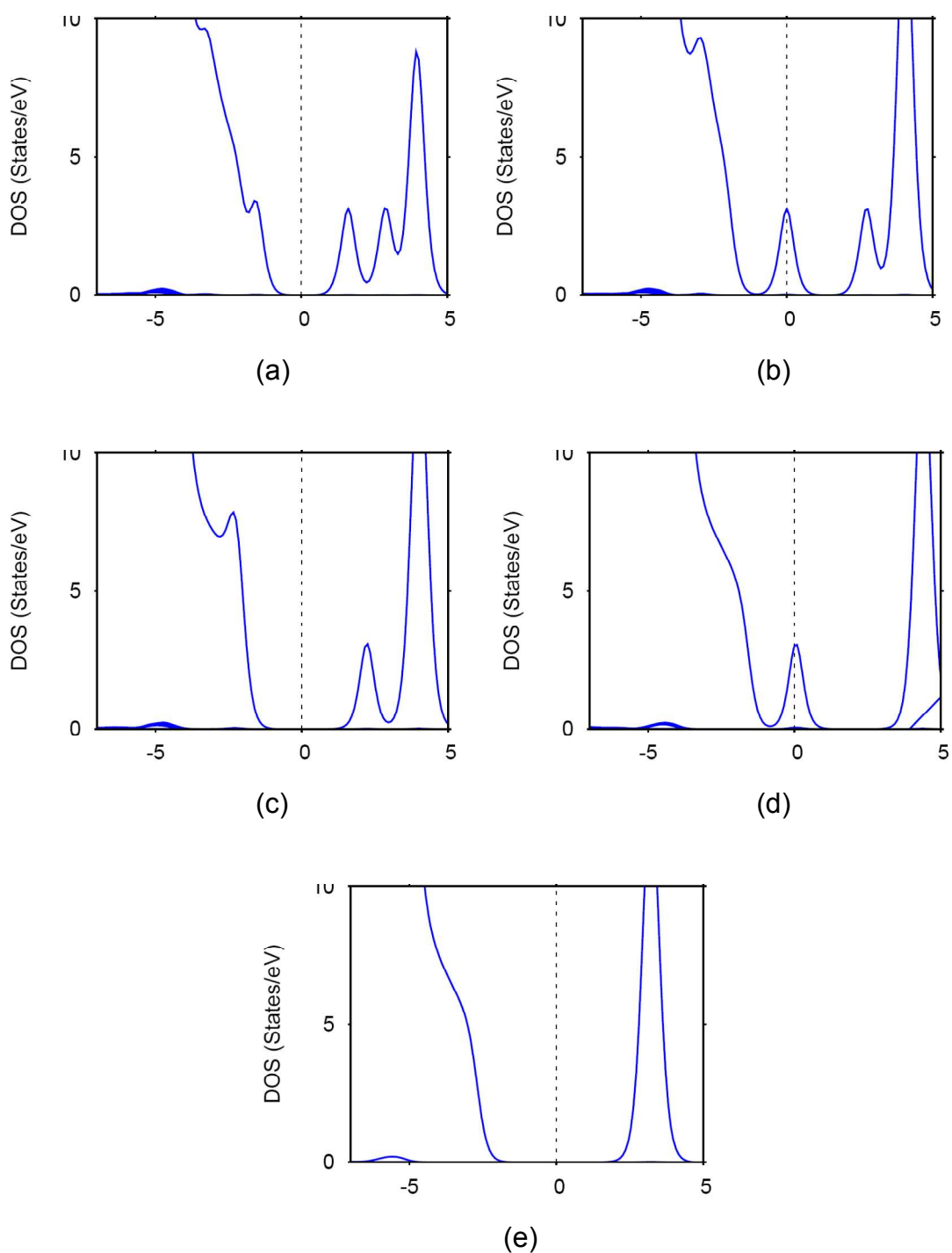


Figure 5.3 - The total DOS for hydrogenated graphene for various hydrogen concentrations above 90%. The zero of the energy is taken at the Fermi level and is marked by a vertical line. X axis denotes $E - E_f$. (a) 92% hydrogen; (b) 94% hydrogen; (c) 96% hydrogen; (d) 98% hydrogen; (e) *graphane*

In summary, it is possible to discern, rather broadly, three regions of hydrogen coverage. A low concentration region, where the DOS undergo the distortions due to

loss of lattice symmetry of the system, intermediate concentration region where a metallic-like phase is seen and a very high concentration region where most of the carbon atoms are hydrogenated and vacancy gives rise to midgap states. As discussed before, our calculations show the presence of localized states in the DOS for very low hydrogen coverage as well as for very high hydrogen coverage (midgap states). These DOS show a pattern of peak or a valley at E_f (in case of low coverage) and at the centre of the gap (in case of high coverage). The reasons can be attributed to the existence of sublattice imbalance. If the difference of hydrogen atoms on the two sides of the sheet is odd then it leads to a peak. Hence by adding impurities one by one to *graphane* we get a sequence of midgap states. This is in consistent with the work of Casolo *et.al.* [24] Interestingly this feature is also retained for the intermediate coverages of hydrogen (where we get a finite DOS at the Fermi level) when the sublattice imbalance of hydrogen is one, e.g., in figures 5.2- (e)–(g), we see the peaks at Fermi level. As we shall see in section 5.3.1 this feature has an implication for the magnetic behavior of the system.

In order to bring out the difference between the local electronic structure of the bare carbon atoms and the hydrogenated carbon atoms, we have analyzed the site projected DOS for all the cases. In figure 5.4, we show site projected DOS for 40% hydrogen coverage depicting the contributions from a hydrogenated carbon site and a bare carbon site. Quite clearly, the contribution around the Fermi level comes from the p_z orbitals of bare carbon atoms only. This is a general feature for all the systems investigated. It may be emphasized that in pure graphene all the carbon atoms contribute to a single k point (Dirac point). In contrast to this, upon hydrogenation, only bare carbon atoms contribute to the DOS at Fermi energy, and they do so at many k points of the Brillouin zone. As the concentration increases further (above 80%), there are too few bare carbon atoms available for the formation of delocalized π bonds. The value of DOS approaches zero and a gap is established with a few midgap states.

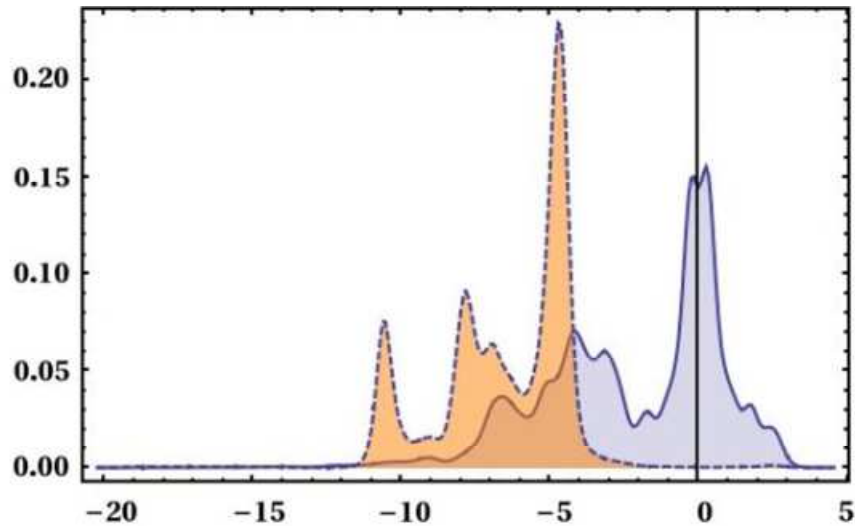


Figure 5.4 - Site projected DOS for hydrogenated carbon sites (dotted line) and bare carbon sites (continuous line) for hydrogen coverage of 40%. Almost all the contribution comes from the p_z which has been shown in the figure. Note that only bare carbon atoms contribute to the DOS at the Fermi level.

The evolution towards the metallic state can be better appreciated by examining the variation in the value of DOS at the Fermi level which is shown in figure 5.5. A clear rise in DOS is seen after 20% hydrogen concentration peaking around 3.5 eV at 50% concentration. This rise is due to the increasing number of k points contributing to the Fermi level, as inferred from the analysis of the individual bands. Evidently, over a significant range of concentration, the value at Fermi level is more than 2 eV^{-1} . The decline seen after 60% is because of the reduction in the number of bare carbon atoms. The character of the DOS changes after about 80%. The value of the DOS at the Fermi level oscillates between zero and some finite value. It is most convenient to describe this region as *graphane* with defects by the removal of a few hydrogen atoms giving rise to midgap states. The nature and the placement of the induced states is dependent on the number of hydrogen atoms removed.

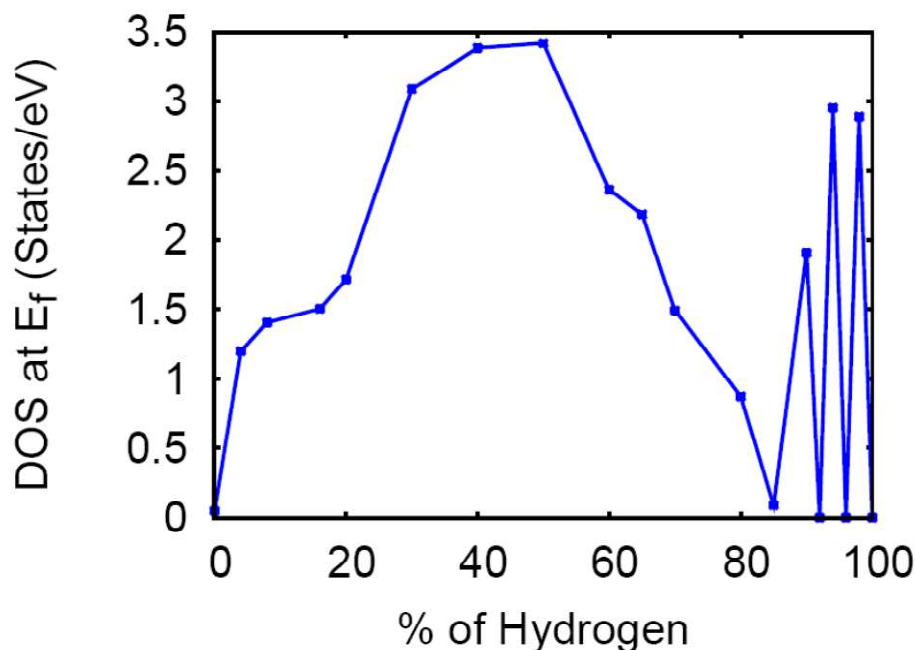
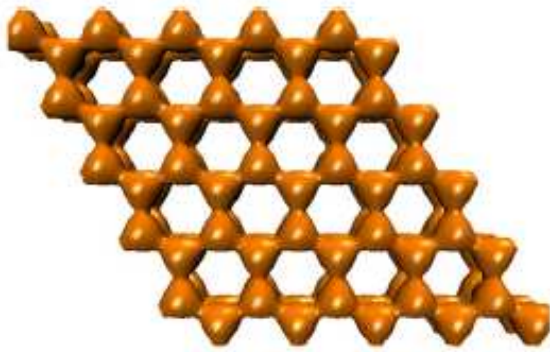


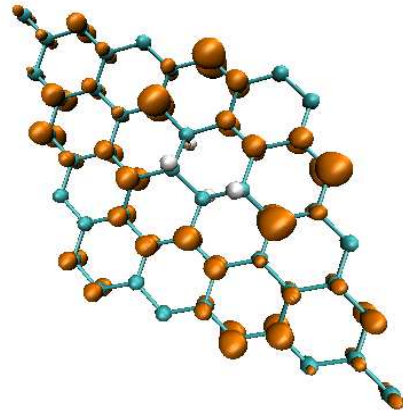
Figure 5.5 - Variation of the value of DOS at the Fermi level as a function of hydrogen coverage.

It may be emphasized that the presence of states around the Fermi level giving finite DOS does not guarantee that the system is metallic unless we examine the nature of localization of the individual states. Therefore we have examined the energy resolved charge densities of the states near the Fermi level and the electron localization function (ELF). The energy resolved charge densities are obtained by summing the charge densities of all the \mathbf{k} points contributing in the small energy region near E_f . Therefore, the charge densities shown in figure 5.6 for different hydrogen coverages specifically bring out the nature of the states near E_f . A particularly striking feature is the formation of two spatially separated regions as seen in figures 5.6-(e) and (f). The hydrogenated regions hardly contribute to the charge density giving rise to the insulating regions surrounded by the π bonded bare carbon atoms forming conducting regions. This feature is also seen for the higher concentrations up to 70%. It may be emphasized that the topology in this range of concentrations (30%–70%) shares a common feature namely, there is a contiguous region formed by the bare carbon atoms.

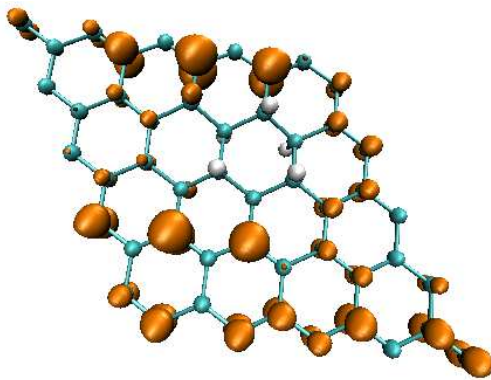
5. Electronic structure of graphene and *graphane*



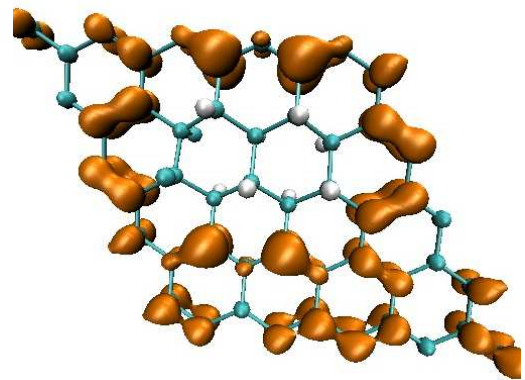
(a) Graphene



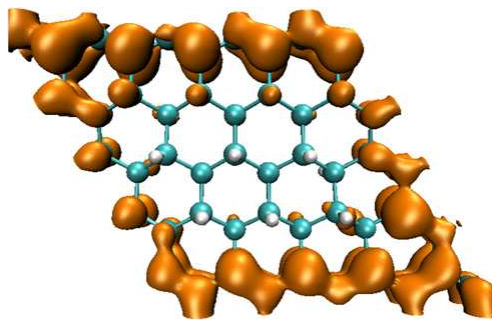
(b) 8%H



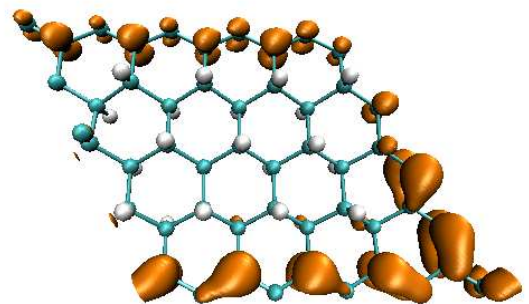
(c) 16%H



(d) 20%H



(e) 40% H



(f) 50% H

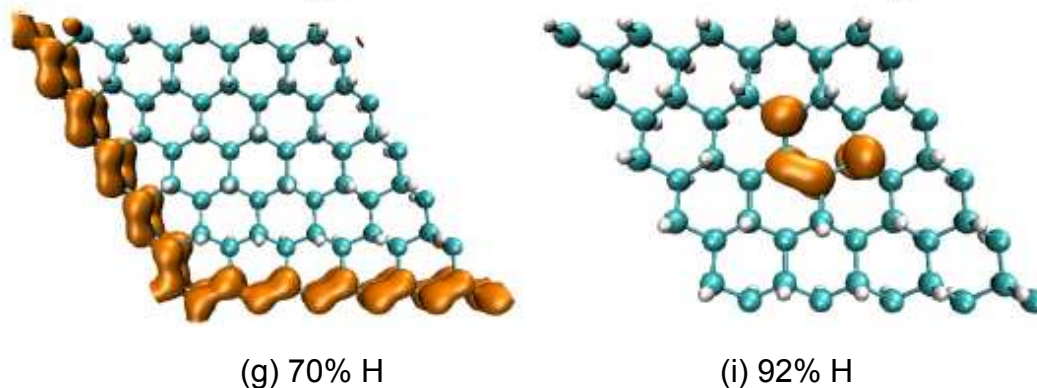


Figure 5.6 – Isosurfaces of charge densities of bands near the Fermi level. For comparison, the charge density of graphene at the Dirac point is also shown. (a) Graphene; (b) 8% hydrogen; (c) 16% hydrogen; (d) 20% hydrogen (e)40% hydrogen (f) 50% hydrogen (g) 70% hydrogen and (i) 92% hydrogen

It may be pointed out that the contiguous charge density is attributed to the favored configuration of compact cluster formation⁵. The change in the character of the state at 90% and above is also evident in figure 5.6-(i). There are insufficient number of bare carbon atoms to form contiguous regions. As a consequence, these carbon atoms form localized bonds giving rise to midgap states noted earlier.

The degree of delocalization of an electron of the system can be understood by examining the electron localization function (ELF) the details of which are given in Chapter 2. We have examined the isosurfaces of ELF for various values between 0.5 and 1.0. The isosurface for a typical value 0.75 is shown in figure 5.7-(a) for 70% coverage. It can be seen that for this high value isosurface exists mainly along carbon–hydrogen bonds (σ - p_z). The existence of localized σ bonds between the bare carbon atoms can also be noticed. In figure 5.7-(b) we show the isosurface for the value of 0.62. The figure shows a continuous surface covering all the bare carbon atoms. This signifies the delocalized nature of the charge density arising out of π bonds formed by p_z orbitals. We have analyzed the ELF for all the coverages. The above features are seen for the coverages from 30% to 80%. Thus the analysis of ELF confirms the delocalized nature of the charge density near the Fermi level for the concentration from 30% to 80%.

⁵ It is our conjecture, based on results of classical bond percolation on 2D hexagonal lattice, that below hydrogen concentration of 61.5% (randomly distributed), the bare carbon atoms will form continuous chains. However, we have not carried out any calculations to verify this.

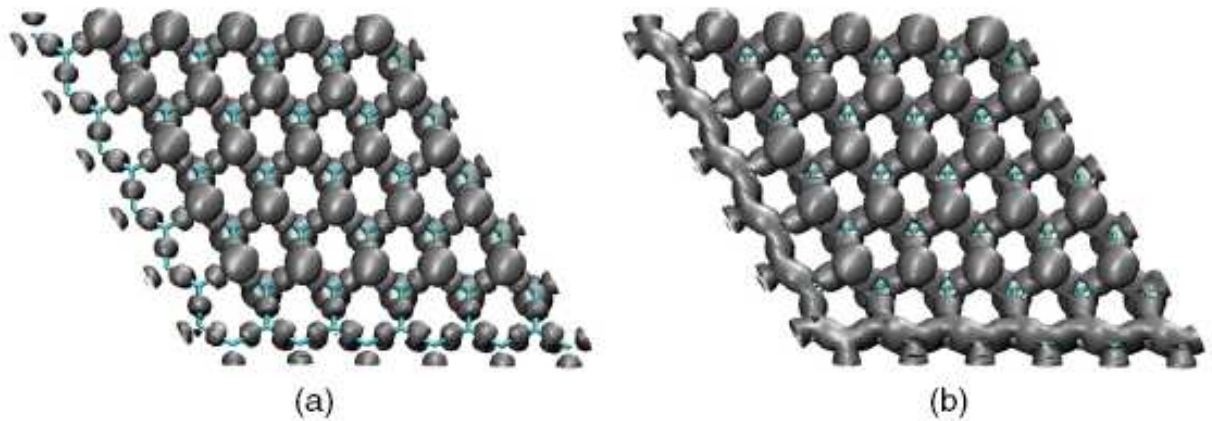


Figure 5.7 - ELF plots with two different isosurface values for 70% hydrogen concentration. (a) shows for isosurface value 0.75 and (b) shows for isosurface value 0.62.

5.3.1 Magnetism

The existence of a peak at Fermi level in the non-spin polarized calculation is an indication of Stoner instability that may lead to a more stable spin-polarized solution. As an example we have analyzed the case of 50% hydrogen coverage which shows a peak in the DOS at the Fermi level. When we allow spin polarization in our calculations, indeed we find a stable ferromagnetic solution, e.g., for 50% hydrogen coverage we get a total magnetic moment $\sim 1\mu_B$ per unit cell as reflected in the spin density plot shown in figure 5.8-(a). However, the exchange splitting seen on the bare carbon atoms is rather small and is expected to survive only at a very low temperature. This fragile nature of magnetism is clearly indicated by the collapse of magnetic moment with a smearing width of 0.08 eV. The site projected DOS for two bare carbon atoms belonging to two different sublattices along with the spin density plots are shown in figures 5.8-(c) and 5.8-(d). Carbon atom belonging to one sublattice shows a spin-polarized behavior whereas the other sublattice shows a spin-polarized behavior whereas the other sublattice carbon atom has an energy gap in the electronic spectrum. This sublattice effect is similar to what is observed in case of graphene nanoribbons [314].

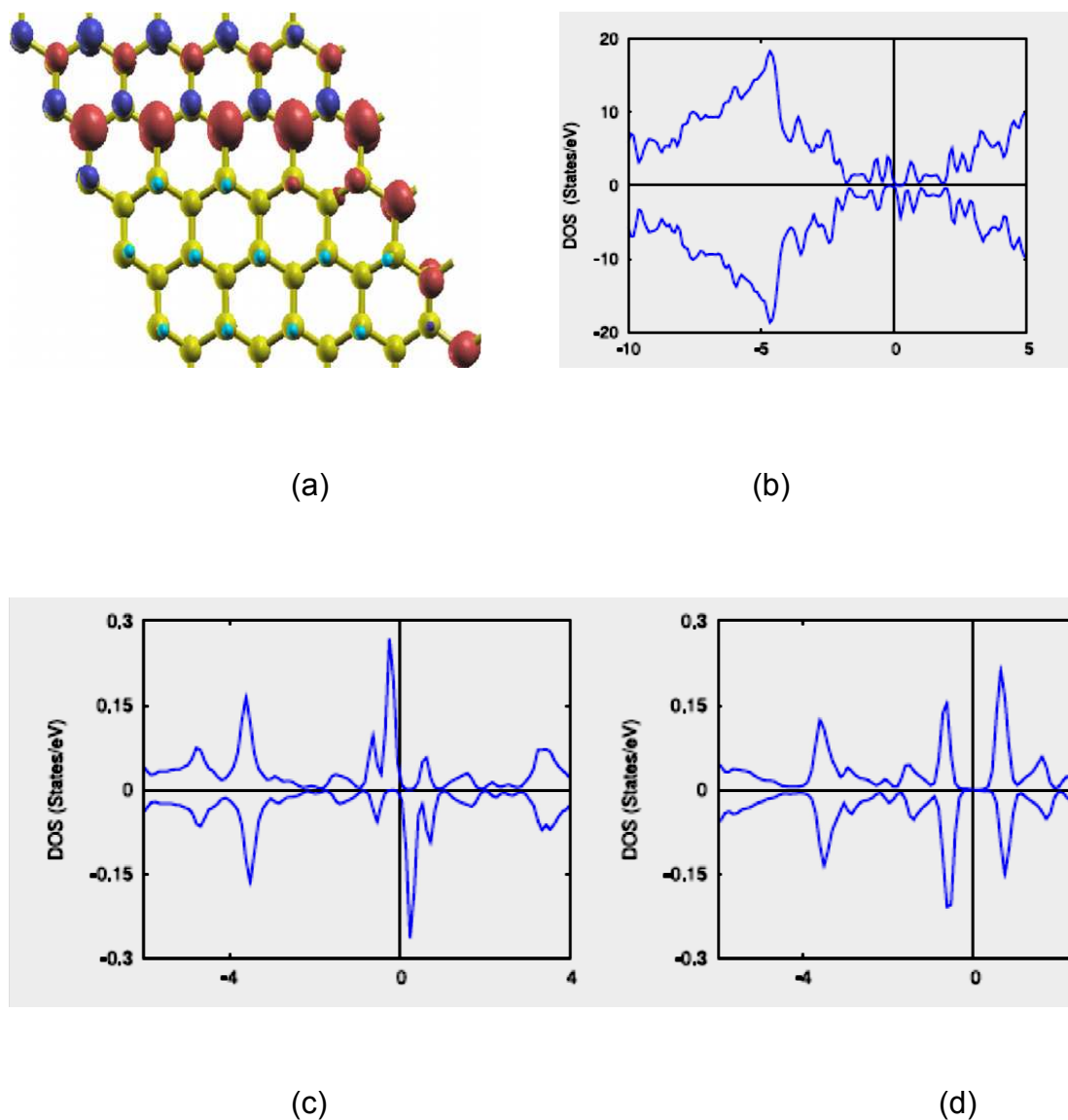


Figure 5.8 – (a) Spin density (b) total DOS (c) and (d) site projected (pz only) DOS for two bare carbon atoms from two different sublattices. X axis of the plots denotes $E - E_f$. This figure is for 50% hydrogen coverage.

5.3.2 Tuning the electronic structure with hydrogenation

Now we bring in another interesting aspect of hydrogenation brought out by our calculations. Our results indicate that it is possible to pattern the graphene lattice with hydrogen and tune the electronic structure. In figure 5.9-(a), the patterning is done by removing the hydrogen atoms along the diagonal of the unit cell where as in figure 5.9-(b) the hydrogen atoms are removed parallel to one edge of the unit cell. The horizontal pattern is more stable than the diagonal pattern by 0.04 eV/H atom. The corresponding DOS are shown in figure 5.9-(c) where a dramatic difference is seen.

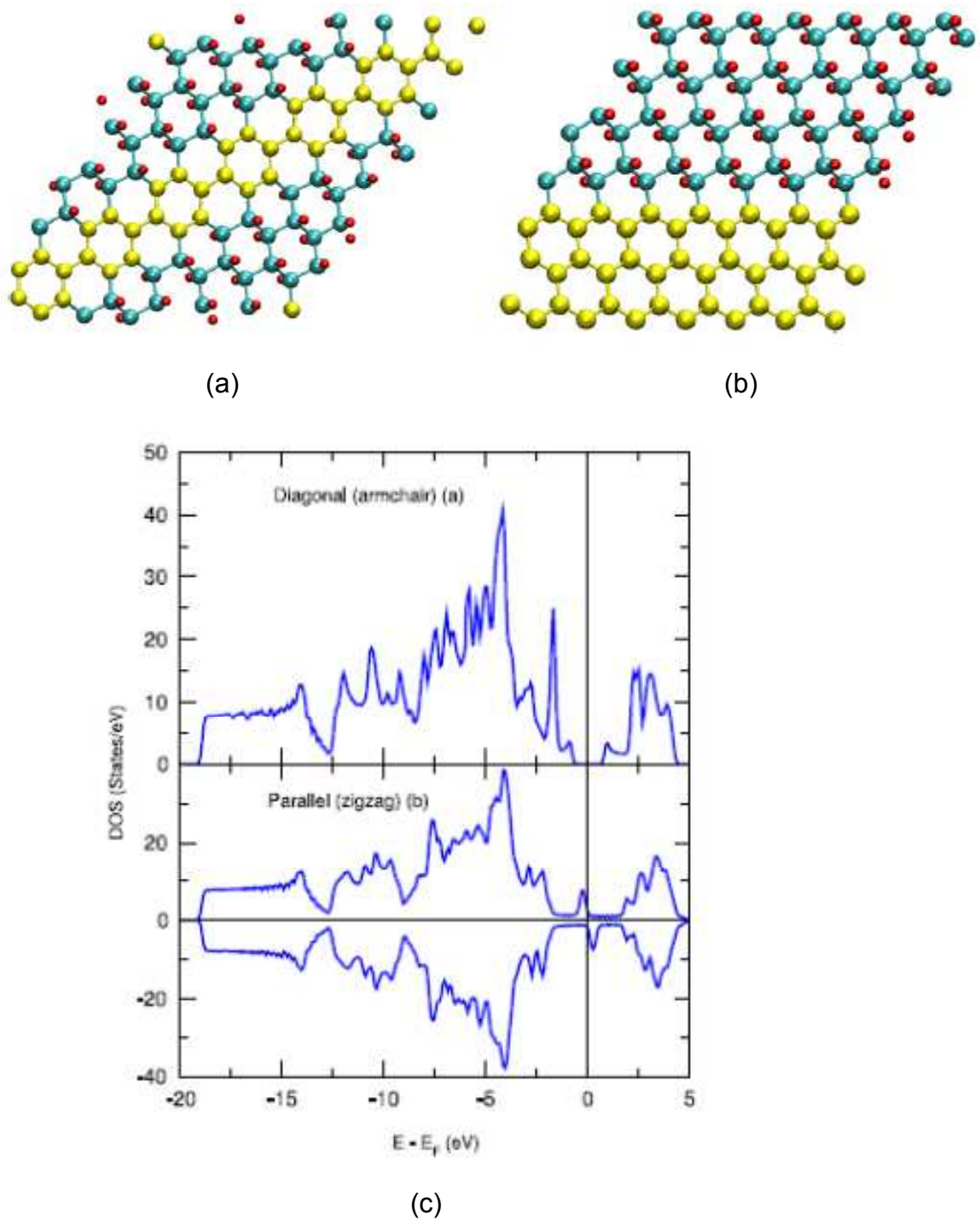


Figure 5.9- Decoration of hydrogen (a) along the diagonal of the unit cell and (b) along the edge of the unit cell. The yellow atoms are the bare carbon atoms. (c) DOS plots for the two cases. The lone atoms seen are from repeating super cells.

The diagonal pattern shows a clear bandgap of 1.4 eV whereas the horizontal pattern shows finite DOS along with a magnetic solution. A close inspection of the geometry reveals an analogy with graphene nanoribbons (GNR). The diagonal pattern

resembles an armchair GNR with a chain of hexagons while the horizontal pattern is analogous to a zigzag GNR with a width of three rows in this particular case. The corresponding DOS also resemble the electronic structure of an armchair (zigzag) GNR with a semiconducting (metallic) nature [315]. It is a reasonable conjecture that the bandgaps of the patterned system can be tuned by controlling the width of the bare carbon channels analogous to the case of armchair GNR where the band gap decreases as the width of GNR is increased.

We emphasize that the hydrogenated systems chosen in this work are such that the energy is always minimum. These are the naturally preferred arrangements of the hydrogen atoms on graphene. However, it is interesting to note that the designed patterns can yield band gaps, magnetic and non-magnetic patterns as discussed in an illustration above. A good deal of work has been carried out on the subject after the publication of this work. Magnetic impurities (single and double Fe atoms) placed in graphene with dehydrogenated channels (armchair and zigzag) are studied via DFT by Haldar *et.al.* [316]. The calculations are performed on 3 different channel widths. Their results show that it is possible to stabilize Fe along the channels of bare carbon atoms, giving rise to a magnetic insulator or a spin gapless semiconductor. The chemical reactivity of the pristine and lithium doped monolayer and bilayer graphene is studied using periodic DFT by Dennis [317]. The results demonstrate that lithium doping can dramatically increase the reactivity of graphene to such an extent that chemical groups that do not react with graphene become bonded when lithium is underneath. Havu *et.al.* demonstrate that that in order to hydrogenate graphene on SiO₂ substrate with different surface termination, it is beneficial to oxygenize the surface and saturate it with hydrogen [318]. A current article discusses the graphene functionalization via hydrogenation in details [319].

5.4 SUMMARY AND CONCLUSIONS

In conclusion, our detailed density functional investigations have revealed some novel features of graphene *graphane* metal–insulator transition. As the hydrogen coverage increases, graphene with a semi-metallic character turns first into a metal and then to an insulator. Hydrogenation of graphene pulls the carbon atom out of the plane breaking the symmetry of pure graphene. As a consequence, many k points in the Brillouin zone contribute to the DOS at the Fermi level giving rise to a metallic

system. The metallic phase has some unusual characteristics: the sheet shows two distinct regions, a conducting region formed by bare carbon atoms and embedded into this region are the non-conducting islands formed by the hydrogenated carbon atoms. The onslaught of insulating state occurs when there are insufficient numbers of bare carbon atoms to form connecting channels. This also means that the transition to insulating phase depends on the distribution of hydrogen atoms and will occur when the continuous channels are absent. The present work opens up the possibility of using partially hydrogenated graphene having designed patterns of conducting channels along with insulating barriers for the purpose of devices. Our results also show that it is possible to design a pattern of hydrogenation so as to yield a semiconducting sheet with a bandgap much lower than that of *graphane*. Finally we may note that the calculation of conductivity in such a disordered system is a complex issue. The present study focuses on the evolution of the density of states to understand the change in the character of single particle orbitals as a function of hydrogen coverage. An obvious extension of this work is the study of transport properties to have a more vivid picture. We believe that in near future, there will be exploding activity leading to graphene based materials.

6. Electronic structure of GNR and H-GNR encapsulated in SWNT

6.1 INTRODUCTION

Encapsulating single walled carbon nanotubes (SWNT) with nano materials such as clusters, [108, 126] linear chains of carbon [140, 145] and cages like fullerene [125, 139] have attracted considerable attention of experimentalists as well as theoreticians. The goal is to use one dimensional nature and the hollow space to create new materials. Indeed a variety of nano structures such as water molecules, [135, 320, 321, 322] liquid gallium, [323] polymeric nitrogen, [324] clusters of aluminum, [325] chains of metal nanowires [326] as well as chains of carbon atoms [142, 144] etc. have been investigated, some experimentally and many via simulations. A class of novel carbon based materials of intense current interest is graphene nanoribbons (GNR), [61] being investigated mainly due to their perceived immense potential for a variety of device applications. Properties of GNR can be tuned by modifying the width and geometry which opens up a possibility of using these in electronic devices. Until recently, the question of filling nanotubes with such GNR was not successfully addressed. Very recently two experimental groups [12, 92] demonstrated the synthesis of such a new material i.e, GNR inside nanotubes. Both the groups have used a novel idea of using the confined space in the nanotubes as a reactor for synthesizing the GNR. Their results indicate that the GNR are energetically stable inside the tube, show twists and can have helical shapes. Interestingly, the preliminary calculations by Talyzin *et.al.* [12] show that the electronic structure can be approximately considered as a superposition of that of bare nanotubes and free standing GNR. Quite clearly this property is of considerable interest for practical applications. The width of hydrogen terminated GNR formed in their experiment and also investigated using density functional theory (DFT) is 3 hexagons.

In the present work we have carried out detailed electronic structure calculations on carbon nanotubes encapsulated by the smallest GNR (partially as well as fully hydrogenated) using DFT. In addition to the references noted above there are two reports on the electronic structure of graphene strips inside nanotubes. Liu *et.al.* [140] have examined the geometries of graphene strip in the SWNT having diameter

smaller than 9.5\AA which corresponds to $(n,m)=(7,7)$. They have also investigated the geometries of finite size carbon chains upto 6 atoms. Their calculations predict that GNR with single hexagon width cannot be inserted in the tubes with diameters less than 12\AA . However, as pointed out by Talyzin *et al.* these helices are formed in rather different way than seen in the experiments.

Indeed, the GNR in CNT is a fascinating area and there are number of reports published recently (after our work). Chamberlain *et.al.* discuss the structure and stability of sulphur terminated GNR in CNT of different diameters [327]. The encapsulated S-GNR exhibit diverse dynamic behavior, including rotation, translation, and helical twisting inside the nanotube, which offers a mechanism for control of the electronic properties of the graphene nanoribbon via confinement at the nanoscale. In another work, dispersion-corrected density functional theory (DFT-D) is applied for investigation of structure and electronic properties of chiral GNR inside CNT [328]. Xie and co-workers investigate the atomic structures, Raman spectroscopic and electrical transport properties of individual graphene nanoribbons of widths $\sim 10\text{--}30\text{ nm}$ derived from sonochemical unzipping of multiwalled carbon nanotubes [329]. Few interesting classical calculations on GNR are worth noting. MD simulations by Jiang *et.al.* on nanoribbons in SWNT [330] show formation of helical structures. In their study the GNR inserted are of the order of 500\AA long and the emphasis is on insertion dynamics. Another work by Li's group, predict that the graphene nanoribbon (GNR) can be helically wrapped onto and insert into the single-walled carbon nanotube (SWNT) to form helical configurations which are close to helices found in nature [331]. Two GNRs would form a DNA-like double-helix with the same handedness. The dependence of the diameter and chirality of SWNT and the width of GNR in the helix-forming process are investigated.

6.2 COMPUTATIONAL DETAILS

All the calculations have been performed within the Kohn-Sham formulation of DFT using Perdew, Burke and Ernzerhof (PBE) [312] scheme of generalized gradient approximations using projector augmented wave (PAW) method as implemented in VASP package with the energy cut-off 400eV . The size of the box along x and y is large enough to avoid the interactions. Typically 10\AA distance is maintained on each side of the tube along x and y direction. The pure GNR consists of 20 carbon atoms

while hydrogenated GNR has additional 20 hydrogen atoms. The length of the ribbons is approximately 12.5Å. The lengths of all the nanotubes are adjusted to match this length by constructing a large unit cell. The whole system is considered to be periodic. We have used the metallic and semiconducting SWNT with parameters (n,m) as : (10,0),(17,0),(22,0) and (6,6),(10,10),(13,13) corresponding to diameters ranging from 8Å to 17Å. During the optimization all the atoms are allowed to relax, the total number in the largest system being 304. The corresponding supercell units along z axis are 5 and 3 times that of unit cell for metallic and semiconducting tubes respectively. We have used 1×1×7 k-mesh for optimization and 1×1×27 for self-consistent calculations.

The relative stabilities of the ribbons are determined by calculating the binding energy (BE) which is defined as

$$E_{bind} = E_{total}(GNR@CNT) - [E_{total}(GNR) + E_{total}(CNT)]$$

Where $E_{total}(GNR@CNT)$ is the total energy of the CNT with the GNR inside it. The negative value of E_{bind} indicates more binding to the tube and the structure is stable.

6.3 RESULTS AND DISCUSSIONS

6.3.1 Pure GNR inside CNT

We will begin the discussion by presenting the geometries, the density of states (DOS) and the partial charge densities of pure GNR. The free standing GNR containing 20 atoms, shown in figure 6.1-(a) is approximately 12.5Å long. We will mainly present the results for the metallic nanotubes and bring up the contrast between the metallic and semiconducting tubes wherever necessary. We have used CNT with 3 different diameters for metallic and semiconducting tubes which are given in table 6.1. For convenience, we shall henceforth refer these as M1, M2 and M3 – metallic CNT and S1, S2 and S3 - semiconducting CNT.

Diameters (Å)	CNT short forms	Diameters (Å)	CNT short forms
8.14	M1	7.83	S1
12.20	M2	13.31	S2
17.63	M3	17.21	S3

Table 6.1 – CNT of different diameters used and their short forms.

In figure 6.1-(b) to figure 6.1-(d) we show optimized geometries of GNR inside the tubes with given diameters.

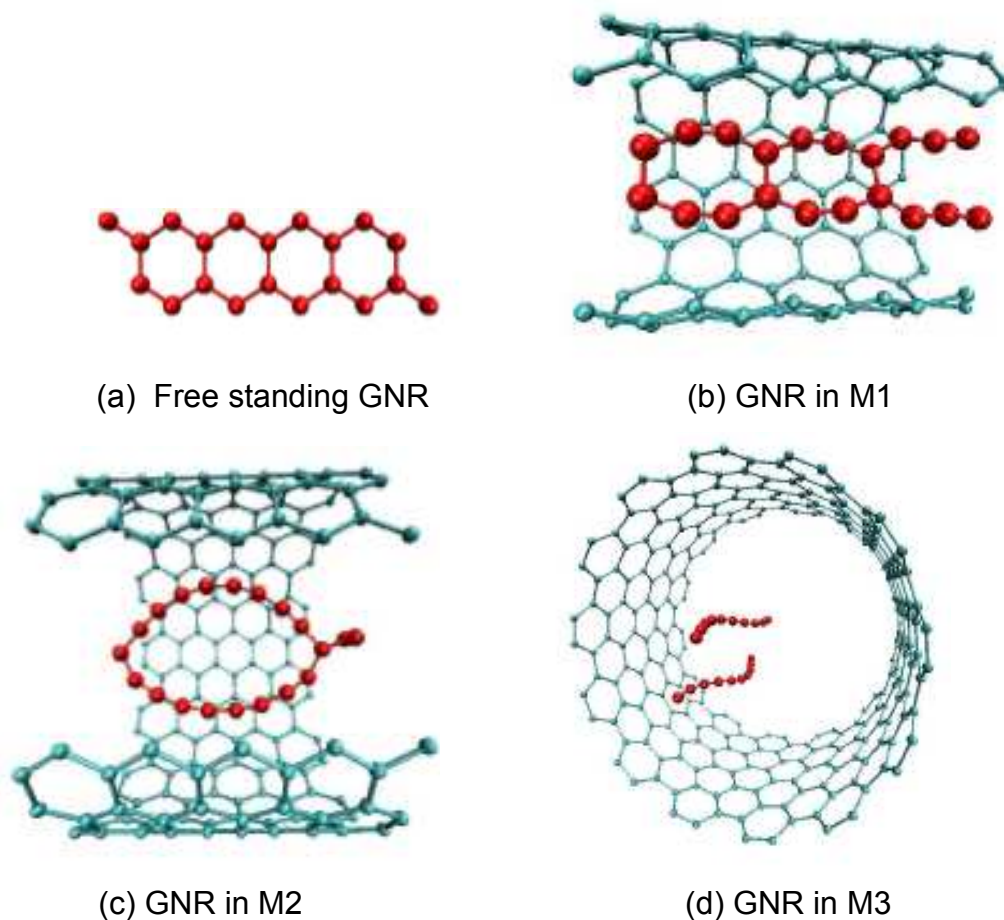


Figure 6.1 - Free standing and optimized geometries of graphene ribbons in the metallic CNT. (a) Original GNR (b) Ring structure having 8 atoms is seen to sustain in the smallest tube. (c) Formation of a single oval shape is seen in larger diameter. (d) Well separated, curved 1-d chains in the largest tube are not placed symmetrically with respect to the axis. The average distance between the chains is 3.8Å.

The remarkable feature observed is the tendency to break the vertical bonds with increasing diameter, leading to two separate chains in the largest diameter (M3) considered. The rings (although with 8 members) are retained in the smallest tube (M1) because of the confinement where the shortest distance between the GNR and the wall is about 3.46\AA . The formation of an interesting oval shape structure seen in the larger tube (M2) indicates that such quasi one dimensional shape is sensitive to the degree of confinement. The two separated chains which is the stable structure in the largest diameter CNT (figure 6.1-(d)), are curved. The GNR inside the semiconducting tubes of similar diameters have similar geometries as shown in figure 6.2.

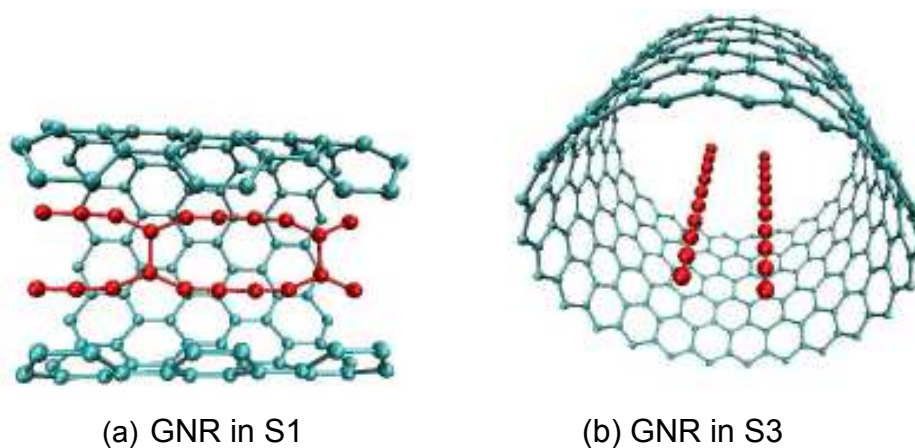


Figure 6.2 - Optimized geometries of graphene ribbons in the semiconducting smallest and largest CNT. (a) Ring structure is having 12 atoms in the smallest tube. (b) Well separated, almost linear 1-d chains in the largest tube indicate that the degree of confinement plays important role in determining the geometry. The average distance between the chains is 3.8\AA

However there are subtle variations in the structures retaining the overall pattern. For example the chains in the largest diameter (S3) are parallel and not curved. In this case the interaction between the ribbon and the walls is somewhat weaker than in the metallic case. We expect such a structure to appear for larger diameters for the metallic tubes. Notwithstanding these differences the nature of the tubes (metallic or semiconducting) is less relevant, physical confinement is more decisive. In free space the GNR are known to show spontaneous instabilities leading to twists [332]. Interestingly for the smallest GNR considered here, the sp^2 bonds are broken and formation of sigma bonds (p_x orbitals) stabilizes the linear structure.

Next, we examine the electronic structure via density of states and the relevant partial charge densities near Fermi level, which are shown in figure 6.3 and 6.4 for the

metallic tubes. The DOS of the bare tubes are also shown for the reference. The nature of the electronic states near the Fermi level can be analyzed by summing the charge densities of all the states near the Fermi level in the narrow energy range of 0.1eV. Isosurfaces for such partial charge densities are also shown in figures. As seen from figures, there is a substantial enhancement in the DOS at Fermi energy (E_f) in all the cases. In the smallest tube (M1), it is evident from figure 6.3-(b) that the contribution at the Fermi energy is mainly due to the carbon atoms located near the end of GNR and does not show a clear delocalized character over the entire length. In figure 6.3-(c), we have also shown the isosurfaces near the prefermi peak observed in DOS at about 0.3eV lower than Fermi level. Indeed this contribution too comes from all the carbons atoms of GNR. We note that the vertical p_z overlap is an additional contribution which was absent at Fermi level.

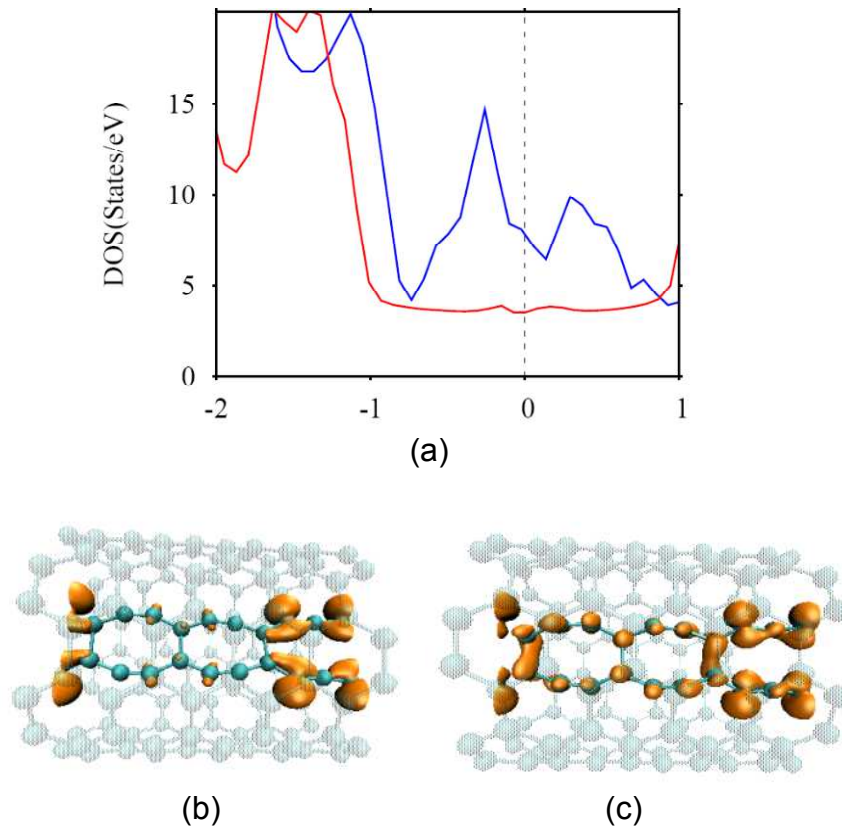


Figure 6.3 – (a) Total DOS for pure GNR in metallic tube S1. The zero of the energy is taken at the Fermi level and is marked by a vertical line. X axis denotes $E - E_f$. The DOS for pure tubes are also shown for reference. (b) Corresponding isosurfaces of charge densities at $1/10^{th}$ of the maximum value. These are the charge densities of the states very close to the Fermi level. At this value the contribution from tube carbon atoms is negligible. The enhancement seen at Fermi is purely from the end-carbon atoms of GNR as shown. (c) The contribution to the prefermi peak is from all the carbons atoms of GNR.

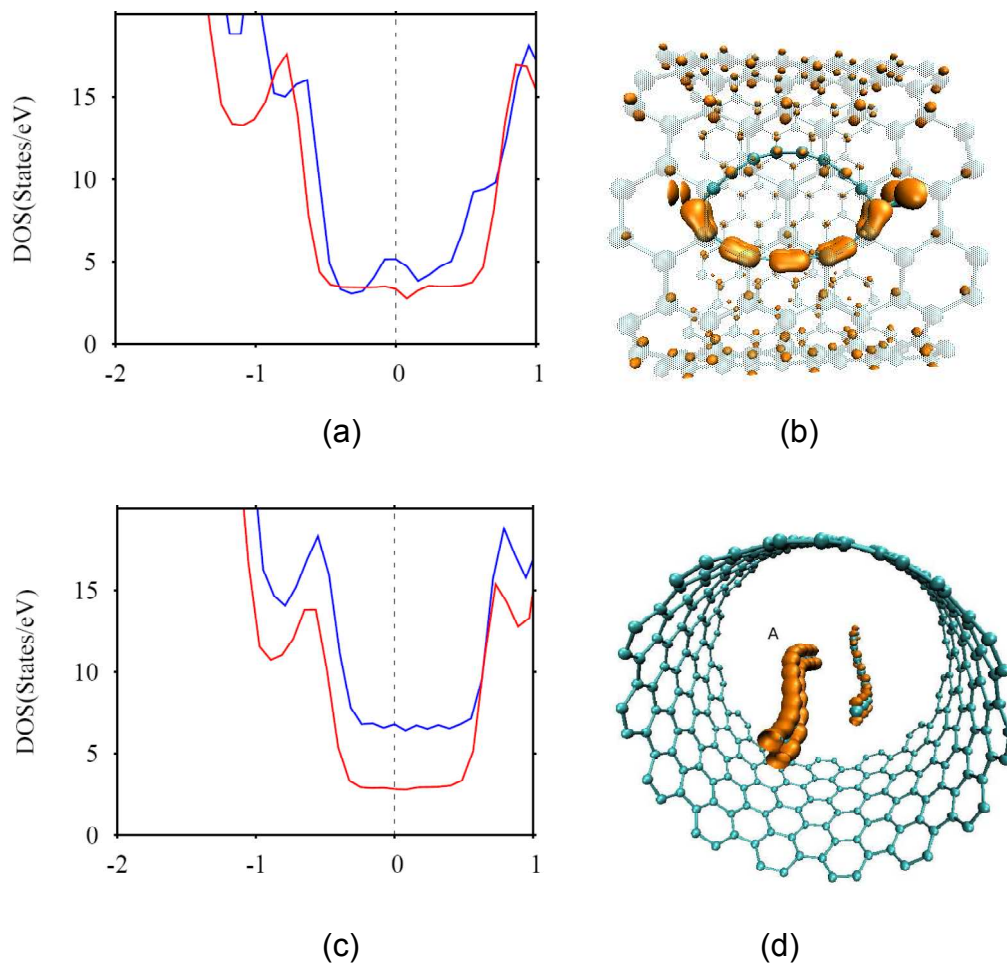


Figure 6.4 – (a) Total DOS and (b) Corresponding isosurfaces of charge densities (close to Fermi) at $1/10^{th}$ of the maximum value in metallic CNT M2. Carbons atoms from one side of the oval GNR contribute more than the other. This contribution is seen in DOS at Fermi. (c) DOS and (d) Isosurfaces of charge densities (close to Fermi) at $1/10^{th}$ of the maximum value for M3. There is a clear enhancement seen at Fermi level retaining the nature of tube DOS. Chain A being close to the wall contributes more than other chain.

In the larger tube (M2), (figure 6.4-(a) and (b)) the contribution from one side of the ring is more than the other because of the asymmetric placement of the ring. In case of the largest diameter CNT (M3) the enhancement at E_f is definitely due to the states from the chain atoms only (figure 6.4-(c) and (d)). The evolution of geometries towards one dimensional structure is clearly reflected in DOS. The DOS evolve from having a peak near Fermi level to a flat one similar to that of pure tube. The curved chains in the largest tube show completely delocalized charge density as depicted in figure 6.4-(d). Quite clearly, the delocalized states are formed by π bonded p_z orbitals

sitting on carbon atoms of the ribbon. It may be recalled that the two chains are not symmetrically placed with respect to the tube axis. The chain marked A is closer to the wall and contributes dominantly at the Fermi level while the second one contributes just below the Fermi energy. Thus our calculations bring out the possibility of forming stable 1-d conductor inside metallic CNT.

The overall pattern of DOS in semiconducting case is very similar to metallic tubes except that the states due to ribbons appear inside the gap. We show two representative cases for CNT S1 and S2 in figure 6.5 and 6.6. We note that the additional states appearing in the gap are from the ribbon. Similar picture is observed in these cases that is, contribution to Fermi level is from GNR atoms. For S2, the partial charge density is calculated for the pre-fermi peak also and is shown in figure 6.6-(c). It is interesting to note that this peak is due to the carbon atoms of the tube only. The GNR atoms only contribute at Fermi level (figure 6.6-(b)). In S1, such peak is observed well below Fermi level at about 1eV. For the largest CNT S3, the two parallel chains formed give rise to the additional states appearing in the gap (figure 6.7).

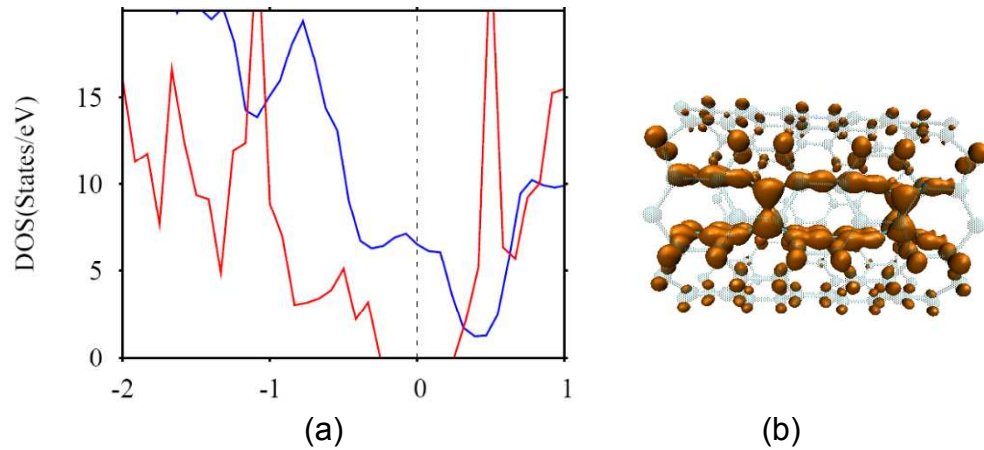


Figure 6.5 – (a) Total DOS for pure GNR in S1. The zero of the energy is taken at the Fermi level and is marked by a vertical line. X axis denotes $E - E_f$. The DOS for pure tube is also shown for reference. The states occurring at Fermi level are due to the GNR atoms. (b) Corresponding isosurfaces of charge densities (close to Fermi) at $1/10^{th}$ of the maximum value.

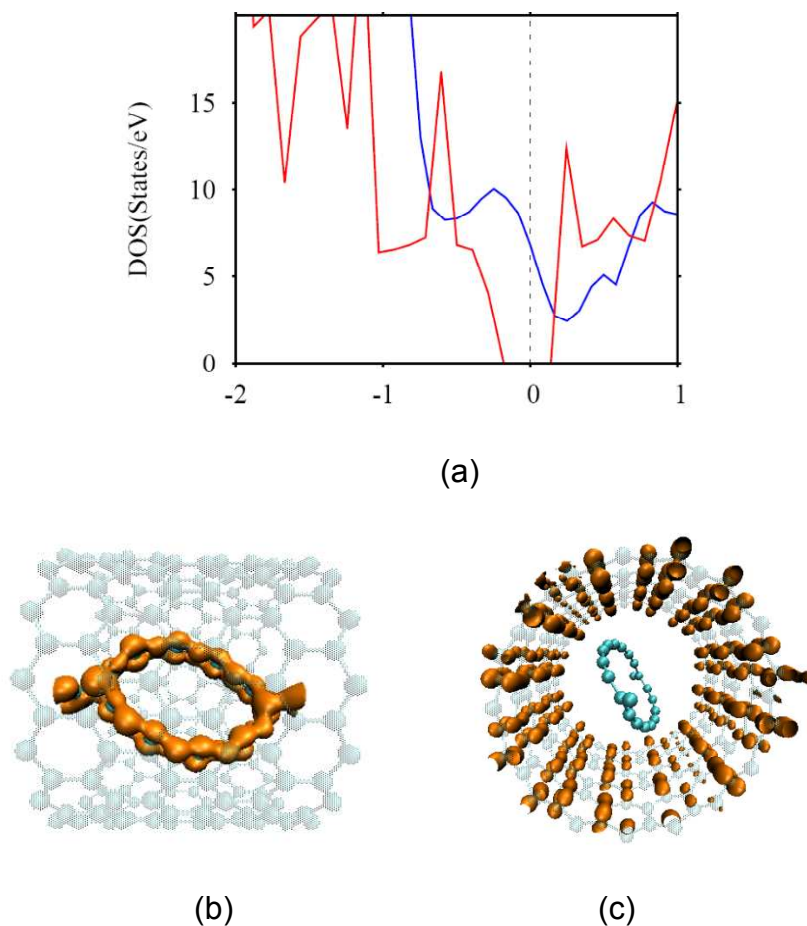


Figure 6.6 – (a) Total DOS for S2. The zero of the energy is taken at the Fermi level and is marked by a vertical line. X axis denotes $E - E_f$. The DOS for pure tube is also shown for reference (red color). The states seen at Fermi are due to GNR atoms only. (b) Corresponding isosurfaces of charge densities (close to Fermi) at $1/10^{th}$ of the maximum value. (c) Isosurfaces near the pre-fermi peak depicting contribution only from the CNT atoms.

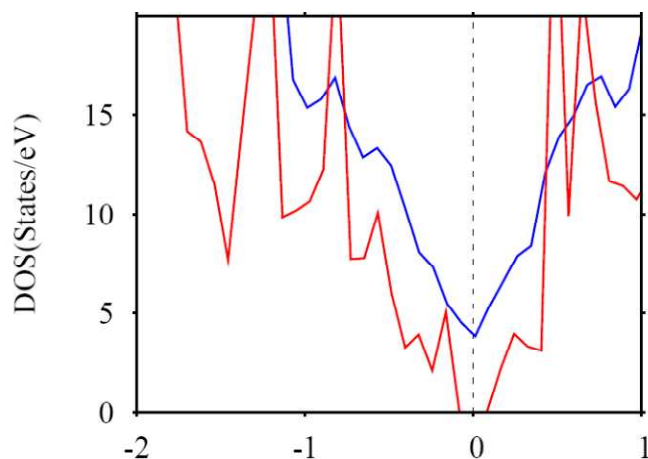


Figure 6.7 – Total DOS for GNR in S3. The corresponding geometry is same as shown in figure 6.2-(b), i.e two parallel chains. The GNR atoms contribute to Fermi giving the midgap states.

Next, our analysis of site projected DOS for all the subsystems reveals that the states appearing at Fermi level are prominently from that of the carbon atoms of GNR. A representative site projected DOS for GNR in S1 are shown in figure 6.8. For the purpose of clarity, the DOS are shown for central and end carbon atoms for angular momentum projections p_y and p_z . The dominant contribution to the peak below Fermi level comes from the sigma bonds formed out of p_y orbitals of (along the bond) carbon atoms of GNR. The contribution from both p_y and p_z of GNR carbons is seen on the Fermi level as shown in figure 6.8. The enhanced DOS at the E_f for this case does not necessarily indicate the existence of conducting channel through GNR.

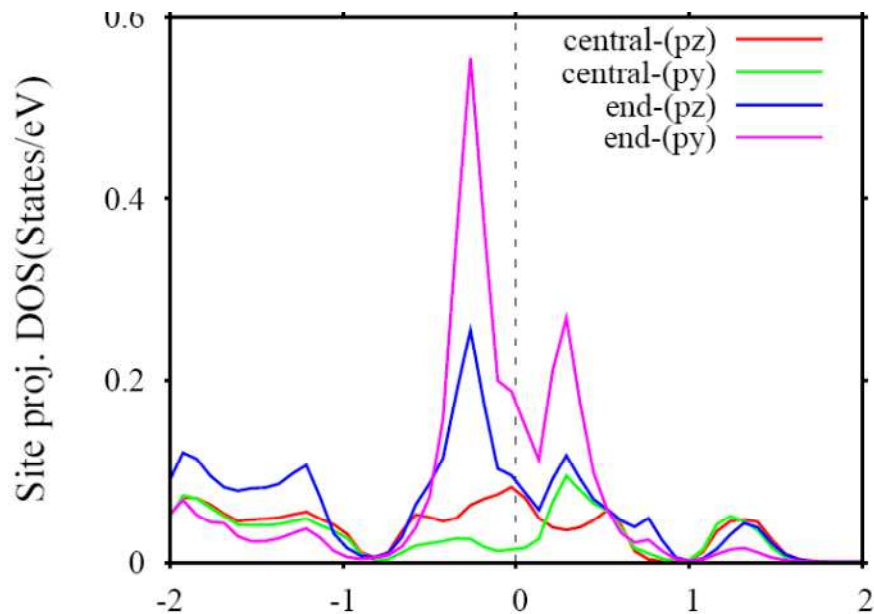


Figure 6.8 - Site projected DOS for graphene nanoribbon in the S1. The prominent contribution towards the peak before Fermi level is from the from the end carbon atoms of the ribbon.

Thus our calculations bring out the possibility of forming stable 1-d conductor inside metallic or semiconducting shell by adjusting the diameter and the width to explore exotic physics of chains and rings experimentally. Recent work by Zeng *et.al.* [333] shows that such carbon chains can act as perfect spin filters and spin valves.

6.3.2 50%H GNR inside CNT

Next we turn to the case of encapsulation of hydrogenated GNR. It is known that hydrogenation of graphene changes its geometry as well as the electronic structure, and the change is dependent on the degree of hydrogenation [20, 21]. Therefore it is of considerable interest to investigate the optimized geometries of 50% hydrogenated GNR as well as fully hydrogenated GNR. We have used two configurations for the placement of hydrogen for the 50% case: systematic and random. In the first case 20 atom GNR is decorated with 50% hydrogens in a systematic manner as shown in figure 6.9-(a). Each hexagon of the ribbon is decorated with two hydrogens placed on the opposite carbon atoms, one on the top and the other on the bottom side, the *graphane* way. We shall refer to this structure as SH. In the second type of configuration, the hydrogens are placed randomly on the GNR keeping the same number of hydrogens on the top and bottom as shown in figure 6.9-(b). This will be referred as RH. Strikingly, for SH all the hydrogens go over to in-plane positions and resulting geometries are independent of the diameter considered (figure 6.9-(c)). The structure is planer leading to hydrogen terminated GNR. This is what has been observed in the experiment [12] in the sense that the in-plane terminated nanoribbons are energetically stable inside the CNT. A point to note is that GNR used in their work are 3 hexagons wide while our work is on a single width GNR. Thus even the smallest GNR (if terminated by hydrogen) having single hexagon width can be stabilized in the nanotube. As expected the electronic structure of this system can be viewed as a superposition of electronic structure of sub systems (figure 6.10). The examination of geometries in the semiconducting CNT shows no significant difference when compared with the metallic ones.

The story is different for randomly placed hydrogenated ribbon (RH). The RH geometries show significant diameter dependent features. The geometries are closer to those of pure GNR except for severe distortions due to hydrogen attachment as shown in figure 6.9-(d). The tendency to form parallel chains by breaking the intermediate bonds in large diameter tubes also persists (figure 6.9- (e)), however structures are modulated by strong C-H bond leading to displacements of carbons away from planer or linear shape. Quite clearly, the placement of hydrogens plays an important role in determining the shapes of the ribbons inside.

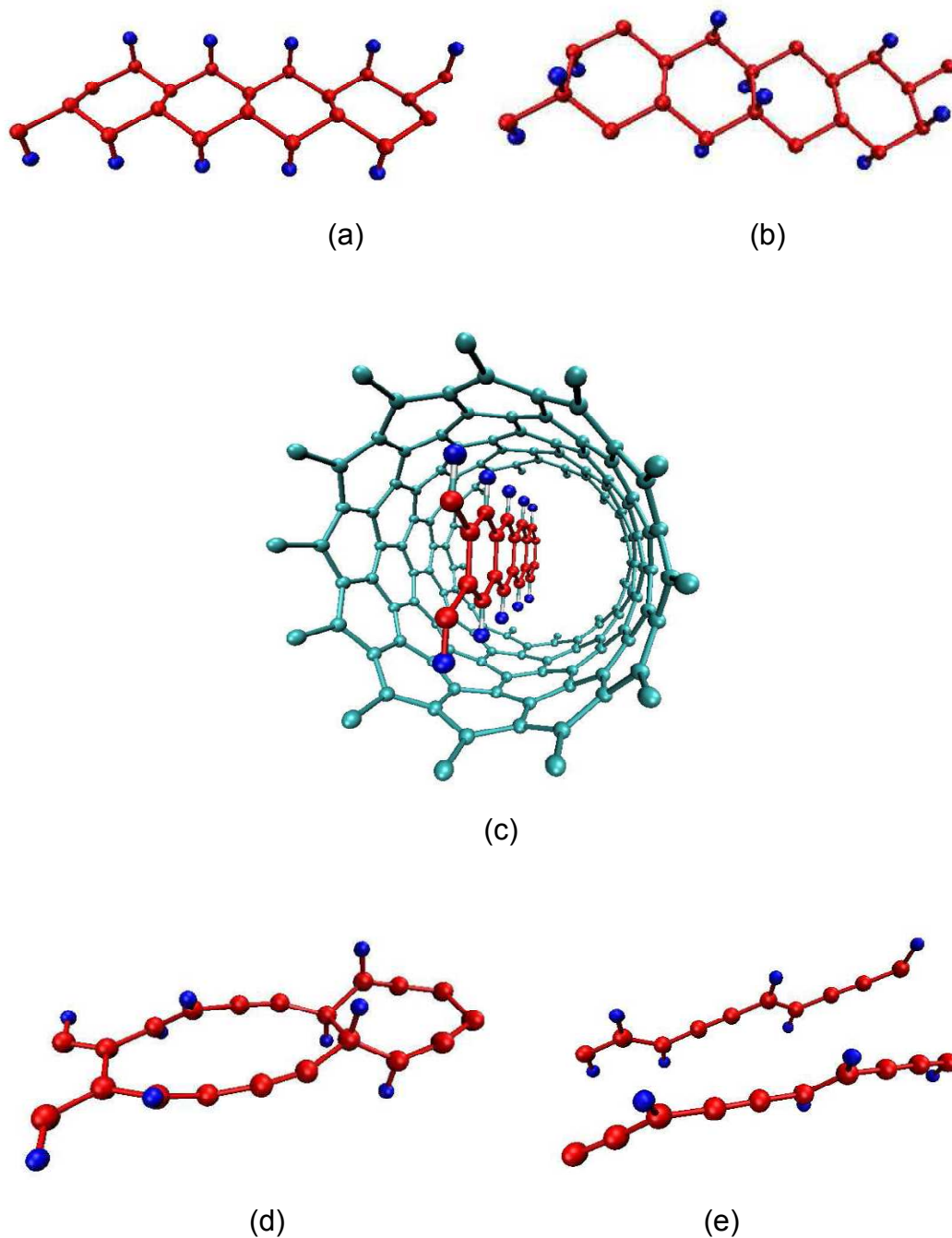


Figure 6.9 - Original geometries for 50%H-GNR – (a) Systematic and (b) random placement in CNT. (c) The SH structure becomes planer after optimization in all CNT (d) RH forms some intermediate shapes in the smaller diameter CNT (e) separated chains in the largest CNT. Note the effect of attached hydrogens leading to distortions.

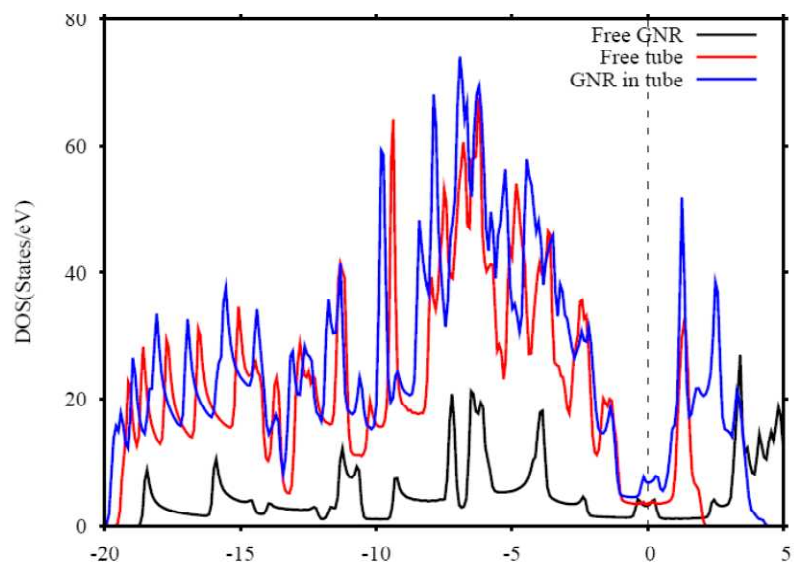


Figure 6.10 - Superimposed DOS for 50%H systematic placement. The zero of the energy is taken at the Fermi level and is marked by a vertical line. X axis denotes $E - E_f$

6.3.3 Fully hydrogenated GNR (H-GNR)

Now we present the results for fully hydrogenated GNR. Remarkably the optimized geometries are not sensitive to the diameter at all. The final structure remains the same, namely two parallel chains in all types of CNT (figure 6.11-(b)). A comparison with the geometries of pure GNR (figure 6.1) reveals some noteworthy differences. In the present case the carbon atoms show zigzag arrangement, as each atom is pulled by the attached hydrogen. The two chains are symmetrically placed with respect to the tube axis due to stronger confinement. It is interesting to look at the DOS for both types of tubes (figure 6.11-(c) and figure 6.11-(d)) which show enhancement at E_f similar to the DOS for pure GNR in the largest tube in spite of the structures being different. In figure 6.11-(e) and (f) we show isosurfaces of partial charges densities in which the overlap of p_z orbitals leading to delocalized charge density along the two chains is evident. The contribution of both the chains is equal unlike in the case of pure GNR. It is interesting to note that there are two stable conducting channels available inside CNT.

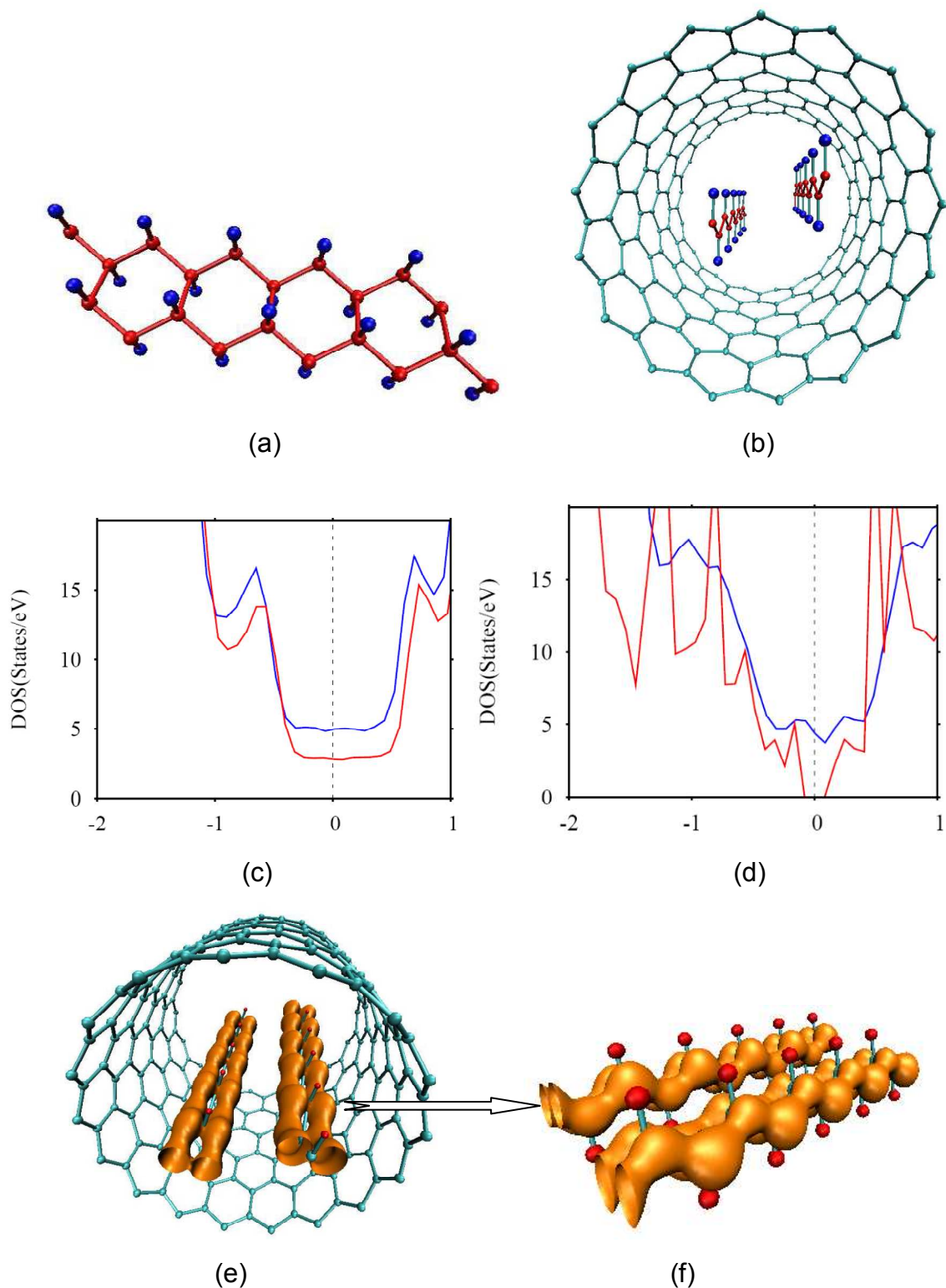


Figure 6.11 – (a) Original H-GNR consisting of 20 carbon and 20 hydrogen atoms. (b) Optimized geometry is same in all CNT, namely parallel stripes with the separation distance varying from 2.58Å to 4Å as the diameter is varied (c) and (d) DOS of H-GNR in a metallic tube and semiconducting tube resp. showing added states at Fermi. (e) Partial charge density shown for semiconducting CNT. The delocalized nature is evident and is observed for H-GNR in all CNT. (f) Close view of the bonding in H-GNR.

We have also calculated the binding energies (BE) for all GNR and the results are tabulated in table 6.2. It turns out that the GNR are stable inside all the tubes. The range of BE/atom for metallic cases is -0.14 eV to -0.06 eV while for semiconducting it is -0.09 eV to -0.03 eV, indicating that the binding is relatively stronger for metallic CNT. There is a decreasing trend in BE/atom as diameter is increased. Our results for BE of GNR are complimentary to those of Liu *et.al.* [143] who have considered such a 20 atom stripe in CNT upto diameter of 9.5Å. Few variations observed are due to the difference in large cutoff and large number of k-points used for optimization.

Metallic			Semiconducting		
Diameter	GNR	H-GNR	Diameter	GNR	H-GNR
8.14	-0.14	-0.12	7.83	-0.09	-0.07
12.20	-0.09	-0.13	13.31	-0.07	-0.09
17.63	-0.06	-0.08	17.21	-0.06	-0.03

Table 6.2 - Binding energies for GNR and H-GNR in different nanotubes

6.4 SUMMARY AND CONCLUSIONS

Finally we note that our results for GNR having one hexagon width compliment DFT results reported in early work [18]. They are also complimentary to the work by Liu *et.al.*[143] where the nanotube diameters were limited to less than 8Å and taken together bring out many interesting features. The geometries of pure GNR change drastically inside the nanotubes having diameters more than 8Å. In the large tubes it can lead to two conducting chains. Our work also reveals the crucial role of in-plane hydrogen termination in stabilizing GNR. Even the smallest possible GNR is seen to be stable inside tubes having sufficiently large diameter. In fact the optimized geometries turn out to be sensitive to the degree of hydrogen coverage. Fully hydrogenated GNR separate into two one dimensional conducting chains, at least for small width case. The nature of the tube (metallic or semiconducting) does not play any significant role in determining the geometry. The possibility of tuning the geometries using CNT of different diameters and GNR of various widths to obtain one dimensional or two dimensional structures could lead to exciting developments.

7. Outlook

The physics of low dimensional systems is undergoing an intense activity both experimentally and theoretically. This thesis focuses on particular aspects of few nanosystems. So the question is where do we expect this field to move? A difficult question indeed!!

The systems examined here are clusters, graphene, *graphane* and GNR inside CNT. Beyond these lie many exotic nanosystems such as clusters on surfaces, two dimensional boron nitride sheets (BNC), defects and impurities in graphene, magnetic clusters, biomolecules and many more. The advent of nanoscience has given a boost to the physics of nanoclusters and nanosystems. There are vast applications of these nanosystems in the areas including spintronics, sensors, tiny binary alloys and many more.

The first phase of the investigations involves the zero temperature properties, stability, bonding etc. Further, the calculations can be extended to incorporate the applications of these novel nanosystems. Lot of work has been carried out on free clusters so far. Such clusters when deposited on surfaces show interesting properties. ‘Clusters on surfaces’ are particularly important in the area of catalysis. Cluster assembled materials on surface are expected to show different mechanical, chemical and magnetic properties. We expect some progress in this area.

The problem of obtaining stable GNR and H-GNR by encapsulation with CNT is still partially addressed in this work. The stability of 2-3 hexagons wide GNR is not examined in the present work. The typical width of GNR used in applications is of few nanometers and hence it is important to test their stability in CNT. Apart from GNR, there is possibility of designing new composite materials where stuffing CNT with quasi 1D material can yield desired properties. Such possibility will be driven by availability of new experimental work.

Apart from graphene, there is also emerging 2D materials such as Boron nitride sheets (BN sheets) exhibiting conducting properties. The transport measurement in these 2D materials as well as GNR based problems is still an open area to work. Our work is limited to the calculation of density of states which simply predicts the conducting nature but the actual conductivity calculations with graphene

based materials is a challenging task. Graphene has been investigated in various areas such as optoelectronic devices; spin transport on graphene grown on SiC, chiral superconductivity in doped graphene, graphene FET, graphene oxide films.

Indeed, the field of graphene and graphene based nanomaterials is exploding and we expect immense activity in the next few years. It goes without saying that this is a paradigm shift towards 'Nano'.

References

- [1] P. Jena, S. N. Khanna and B. K. Rao. *Physics and Chemistry of Finite Systems: From Clusters to Crystals, Vols. 1 and 2*. Kluwer Academic, Dordrecht, Netherlands, 1992.
- [2] P. Jena and S. N. Behera. *Clusters and Nanostructured Material*. Nova Science Publishers Inc., New York, 1996.
- [3] V. Kumar, K. Esfarjini and Y. Kawazoe. *Advances in Cluster Scienc*. Springer-Verlag, Heidelberg, 2000.
- [4] B. Hartke. *Adv. Chem. Int*, 41:1469, 2002.
- [5] P. Jensen. *Rev. Mod. Phys*, 71: 1695, 1999.
- [6] H. Haberland. *Clusters of Atoms and Molecules*. Springer-Verlag, Berlin, 1994.
- [7] R. L. Johnston. *Atomic and Molecular Clusters*. Taylor & Francis, Oxford , 2002.
- [8] F. Baletto and R. Ferrando. *Rev. Mod. Phys.* 77(1): 371, 2005.
- [9] J. Jellinek. *Theory of Atomic and Molecular Cluster*. Springer-Verlag, Berlin, 1999.
- [10] S. N. Khanna and P. Jena. *Phys. Rev. B*, 51(19): 13705, 1995.
- [11] S. N. Khanna and P. Jena. *Phys. Rev. Lett.*, 69(11): 1664, 1992.
- [12] A. V. Talyzin, I. V Anoshkin , A. G. Nasibulin, A. Krashennnikov, R. M. Nieminen, H. Jiang and E. Kauppinen. *Nano Lett.*, 11: 4352-4356, 2011.
- [13] N. F. Johnson. *Journal of Physics:Condensed Matter*, 7: 965, 1995.
- [14] S. D. Tarucha, D. G. Austing, T. Honda, R. J. van der Hage and L. Kouwenhoven. *Phys. Rev. Lett.*, 77(17):3613, 1996.
- [15] U. Meirav, P. L. McEuen, M. A. Kastner, E. B. Foxman, A. Kumar and S. J. Wind. *Z. Phys. B*, 85:357, 1991.
- [16] M. A. Kastner. *Rev. Mod. Phys*, 64:849, 1992.
- [17] K. S. Novoselov, A. K. Geim, S. V. Morozov, D. Jiang, Y. Zhang, S. V. Dubonos, I. V. Grigorieva and A. A. Firsov. *Science*, 306:666, 2004.
- [18] K. S. Novoselov, A. K. Geim, S. V. Morozov, D. Jiang, M. I. Katsnelson, I. V. Grigorieva, S. V. Dubonos and A. A. Firsov. *Nature (London)*, 438: 197, 2005.
- [19] M. I. Katsnelson, K.S. Novoselov and A. K. Geim. *Nature Physics*, 2: 620, 2006.
- [20] J. O. Sofo, A. S. Chaudhari and G. D. Barber. *Phys. Rev. B*, 75:153401, 2007.

- [21] D. C. Elias, R. R. Nair, T. M. G. Mohiuddin, S. V. Morozov, P. Blake, M. P. Halsall, A. C. Ferrari, D. W. Boukhvalov, M. I. Katsnelson, A. K. Geim, and K. S. Novoselov. *Science*, 323 (5914): 610-613, 2009.
- [22] S. Lebègue, M. Klintonberg, O. Eriksson and M. I. Katsnelson. *Phys. Rev. B*, 79:245117, 2009.
- [23] D. W. Boukhvalov, M. I. Katsnelson and A. I. Lichtenstein. *Phys. Rev. B*, 77:035427, 2008.
- [24] S. Casolo, O. M. Løvvik, R. Martinazzo and G. F. Tantardini. *J. Chem. Phys.*, 130:054704, 2009.
- [25] M. Wu, X. Wu, Y. Gao and X. C. Zeng. *J. Phys. Chem. C*, 114(1):139-142, 2010.
- [26] M. Yang, A. Nurbawono, C. Zhang, Y. P. Feng and Ariando. *Appl. Phys. Lett.*, 96:193115, 2010.
- [27] J. Zhou, Q. Wang, Q. Sun, X. S. Chen, Y. Kawazoe and P. Jena. *Nano. Lett.*, 9:3867-3870, 2009.
- [28] J. Bang and K. J. Chang. *Phys. Rev. B.*, 81:193412, 2010.
- [29] B. R. Matis, J. S. Burgess, F. A. Bulat, A. L. Friedman, B. H. Houston and J. W. Baldwin. *ACS Nano*, 6: 17-22, 2012.
- [30] D. Haberer, D. V. Vyalikh, S. Taioli, B. Dora, M. Farjam, J. Fink, D. Marchenko, T. Pichler, K. Ziegler, S. Simonucci, M. S. Dresselhaus, M. Knupfer, B. Büchner and A. Grüneis. *Nano Lett.*, 10:3360, 2012.
- [31] B. S. Pujari, S. Gusarov, M. Brett and A. Kovalenko. *Phys. Rev. B*, 85:041402, 2011.
- [32] A. H. Castro Neto, F. Guinea and N. M. R. Peres, K. S. Novoselov and A. K. Geim. *Rev. Mod. Phys.*, 81(1):109, 2009.
- [33] R. P. Wallace. *Phys. Rev.*, 71:622, 1947.
- [34] H. P. Boehm, A. Clauss and U. Hofmann. *J. Chim. Phys.*, 58:141, 1961.
- [35] H. P. Boehm, A. Clauss, U. Hofmann and G. O. Fischer. *Z. Naturf*, 17:150, 1962.
- [36] P. Sutter. *Nature Material*, 8:171, 2009.
- [37] C. Berger, Z. Song, T. Li, X. Li, A. Y. Ogbazghi, R. Feng, Z. Dai, A. N. Marchenkov, E. H. Conrad, P. N. First and Walt A. de Heer. *J. Phys. Chem. B*, 108:19912, 2004.
- [38] D. R. Cooper, B. D'Anjou, N. Ghattamaneni, B. Harack, M. Hilke, A. Horth, N. Majlis, M. Massicotte, L. Vandsburger and E. Whiteway and V. Yu. *ISRN Condensed Matter Physics*, 501686:56, 2012.

- [39] A. H. Castro Neto and K. Novoselov. New directions in science and technology: two-dimensional crystals. *Reports on progress in physics*, 74(8):082501, 2011.
- [40] M. S. Fuhrer, C. N. Lau and A. H. MacDonald. Graphene: Materially Better Carbon, *MRS Bulletin*, 35:289, 2010.
- [41] A. F. Young and P. Kim. Electronic Transport in Graphene Heterostructures. *Annual Review of Condensed Matter Physics*, 2:101-120, 2011.
- [42] S. D. Sarma, S. Adam, E. H. Hwang and E. Rossi. Electronic transport in two dimensional graphene. *Rev. Mod. Phy*, 83: 407, 2011.
- [43] P. Avouris, *Nano Lett.*, 10:4285, 2010.
- [44] F. Bonaccorso, Z. Sun, T. Hasan and A. C. Ferrari. Graphene photonics and optoelectronics. *Nature Photonics*, 4: 611, 2010.
- [45] J. Wu, M. Agarwal, H. A. Becerril, Z. Bao, Z. Liu, Y. Chen and P. Peumans. *ACS Nano*, 4(1): 43-48, 2010.
- [46] C. Lee, X. Wei, J. W. Kysar and J. Hone. *Science*, 321(5887);385-388, 2008.
- [47] A. A. Balandin. Thermal properties of graphene and nanostructured carbon materials. *Nature Materials*, 10:569. 2011.
- [48] A. A. Balandin, S. Ghosh, W. Bao *et. al.* *Nano Lett.*, 8:902, 2008.
- [49] S. Ghosh, I. Calizo, D. Teweldebrhan *et. al.* *App. Phys. Lett.*, 92:151911, 2008.
- [50] W. Cai, A. L. Moore, Y. Zhu, X. Li, S. Chen, L. Shi and R. S. Ruoff. *Nano Lett.*, 10:1645, 2010.
- [51] S. Chen, A. L. Moore, W. Cai, J. W. Suk, J. An, C. Mishra, C. Amos, C. W. Magnuson, J. Kang, Li Shi and R. S. Ruoff. *ACS Nano*, 5: 321, 2011.
- [52] Y. Zhang, Y.-W. Tan, H. L. Stormer and P. Kim. *Nature(London)*, 438: 201, 2005.
- [53] E. J. Duplock, M. Scheffler and P. J. D. Lindan. *Phys. Rev. Lett.*, 92:225502, 2004.
- [54] R. Balog, B. Jørgensen, L. Nilsson, M. Andersen, E. Rienks, M. Bianchi, M. Fanetti, E. Laegsgaard, A. Baraldi, S. Lizzit, Z. Slijivancanin, F. Besenbacher, B. Hammer, T. G. Pedersen, P. Hofmann and L. Hornekær. *Nat. Mater.*, 9:315, 2010.
- [55] P. Shinde and V. Kumar. *Phys. Rev. B*, 84:125401, 2011.
- [56] G. Giovannetti, P. A. Khomyakov, G. Brocks, P. J. Kelly and J. Brink. *Phys. Rev. B*, 76:073103, 2007.
- [57] D. Jariwala, A. Srivastava and P. M. Ajayan. Graphene Synthesis and Band Gap Opening. *J. Nanosc. and Nanotech.* 11: 6621, 2011

- [58] X. Fan, Z. Shen, A. Q. Liu and Jer-Lai Kuo. *Nanoscale*, 4:2157, 2012.
- [59] C. Chang, X. Fan, L. Li and Jer-Lai Kuo. *J.Phys. Chem C*, 116:13788, 2012.
- [60] R. Martinazzo, S. Casolo and G. F. Tantardini. *Phys. Rev. B*, 81:245420, 2010.
- [61] M. Fujita, K. Wakabayashi, K. Nakada and K. Kusakabe. *J. Phys. Soc. Jpn.*, 65:1920, 1996.
- [62] K. Nakada, M. Fujita, G. Dresselhaus and M. S. Dresselhaus. *Phys. Rev. B*, 54:17954, 1996.
- [63] K. Wakabayashi, M. Fujita, H. Ajiki and M. Sigrist. *Phys. Rev. B*, 59:8271, 1999.
- [64] Y. Son, M. L. Cohen and S. G. Louie. *Phys. Rev. Lett.*, 97:216803, 2006.
- [65] L. Brey and H. A. Fertig. *Phys. Rev. B*, 73:235411, 2006.
- [66] M. Y. Han, B. Özyilmaz, Y. Zhang P. Kim. *Phys. Rev. Lett.*, 98:206805, 2007.
- [67] T. Shimizu, J. Haruyama, D. C. Marcano, D. V. Kosinkin, J. M. Tour, K. Hirose and K. Suenaga. *Nature Nanotechnology*, 6: 45-50, 2011.
- [68] M. Ezawa. *Phys. Rev. B*, 73:045432, 2006.
- [69] Z. H. Chen, Y. M. Lin, M. J. Rooks and P. Avouris. *Physica E (Amsterdam)*, 40:228-232, 2007.
- [70] V. Barone, O. Hod and G. E. Scuseria. *Nano. Lett.*, 6:2748-2754, 2006.
- [71] J. J. Palacios, J. Fernández-Rossier, L. Brey and H. A. Fertig. *Electronic and magnetic structure of graphene nanoribbon*, *Semicond. Sci. Technol.*, 25:033003, 2010.
- [72] M. Terrones et.al. *Graphene and graphite nanoribbons: Morphology, properties, synthesis, defects and applications*. *Nano Today*, 5(4): 351, 2010.
- [73] S. Dutta and S. K. Pati. *Novel properties of graphene nanoribbons: a review*. *J. Mat. Chem.*, 20: 8207-8223, 2010.
- [74] L. Jiao, L. Zhang, X. Wang, G. Diankov and H. Dai. *Nature Lett.*, 458:877-880, 2009.
- [75] L. Jiao, X. Wang, G. Diankov, H. Wang and H. Dai. *Nature Nanotechnology*, 5: 321, 2010.
- [76] D. V. Kosynkin, A. L. Higginbotham, A. Sinitski, J. R. Lomeda, A. Dimive, B. K. Price and J. M. Tour. *Nature Lett.*, 458:872-876, 2009.
- [77] L. Ma, J. Wang and F. Ding. *Recent Progress and Challenges in Graphene Nanoribbon Synthesis*. *ChemPhysChe*, ISSN: 1439-7641, 2012.
- [78] L. Tapasztó, G. Dobrik, P. Lambin and L. P. Biro. *Nature Nanotech.*, 3: 397-401, 2008.

- [79] J. Cai, P. Ruffieux, R. Jaafar, M. Bieri, T. Braun et al. *Nature Lett.*, 466:470-473, 2010.
- [80] X. Li, X. Wang, L. Zhang, S. Lee and H. Dai. *Science*, 319:1229-1232, 2008.
- [81] H. C. Schniepp et al. *J. Phys. Chem. B*, 110: 8535-8539, 2006.
- [82] E. Rollings et al. *J. Phys. Chem. Solids*, 67:2172-2177, 2006.
- [83] S. S. Datta, D. R. Strachan, S. M. Khamis and A. T. Johnson. *Nano. Lett.*, 8: 1912-1915, 2008.
- [84] X. Yang, X. Dou, A. Rouhanipour, L. Zhi, H. J. Räder and K. Müllen. *J. Am. Chem. Soc.*, 130: 4216, 2008.
- [85] J. Campos-Delgado et al. *Nano Lett.*, 8:2773-2778, 2008.
- [86] D. K. James and J. M. Tour, *Macromol. Chem. Phys.*, 213:1033, 2012.
- [87] L. Dossel, L. Gherghel, X. Feng and K. Müllen. *Chem. Int. Ed*, 50:2540, 2011.
- [88] A. P. Seitsonen, A. M. Saitta, T. Wassmann, M. Lazzeri and F. Mauri. *Phys. Rev. B*, 84: 115425, 2010.
- [89] C. Jin, H. Lan, L. Peng, K. Suenaga and S. Iijima. *Phys. Rev. Lett.*, 102:205501, 2009.
- [90] Z.-S. Wu, W. Ren, L. Gao, B. Liu, J. Zhao and H.-M. Cheng. *Nano Res*, 3:16, 2010.
- [91] A. Sinitskii and J. M. Tour. *Appl. Phys. Lett.*, 100:103106, 2012.
- [92] A. Chuvilin, E. Bichoutskaia, M. C. Gimenez-Lopez, T. W. Chamberlain, G. A. Rance, N. Kuganathan, J. Biskupek, U. Kaiser and A. N. Khlobystov. *Nature Materials*, 10:687-692, 2011.
- [93] S. Iijima. *Nature*, 56:354, 1991.
- [94] N. Hamada, S. Sawada & A. Oshiyama. *Phys. Rev. Lett.*, 68:1579, 1992.
- [95] M. S. Dresselhaus, G. Dresselhaus, J. C. Charlier and E. Hernández. *Electronic, thermal and mechanical properties of carbon nanotubes*. *Phil. Trans. R. Soc. Lond. A*, 362:2065-2098, 2004.
- [96] S. P. Frank, P. Poncharal, Z. L. Wang and W. A. de Heer. *Science*, 280:1744, 1998.
- [97] P. McEuen. *Phys. World*, 13:31, 2000.
- [98] R. Baughman, A. Zakhidov and Walt A. de Heer. *Science*, 297:787, 2002.
- [99] J. M. Schnorr and M. Timothy. *Chem. Mater.*, 23:646-657, 2011.
- [100] J. C. Charlier, X. Blase and S. Roche. *Rev. Mod. Phys.*, 79:677-732, 2007.

- [101] J. W. Mintnire and C. T. White. *Carbon*, 33(7):893-902, 1995.
- [102] M.S. Dresselhaus, G.Dresselhaus and R. Saito. *Carbon*, 33:883, 1995.
- [103] O. Gülseren, T. Yildirim and S. Ciraci. *Phys. Rev. B*, 66:121401, 2002.
- [104] A. Nikitin, X. Li, Z. Zhang, H. Ogasawara, H. Dai and A. Nilsson. *Nano Lett.*, 8(1):162-167, 2008.
- [105] H. Lee, J. Ihm, M. L. Cohen and S. G. Louie. *Phys. Rev. B*, 80:115412, 2009.
- [106] T. Yildirim and S.Ciraci., *Phys. Rev. Lett.*, 94:175501, 2005.
- [107] E. Durgun, S. Ciraci and T. Yildirim. *Phys. Rev. B*, 77:085405, 2008.
- [108] B. Chen, B. Li and L. Chen. *App. Phys. Lett.*, 93:043104, 2008.
- [109] S. Pekker, J.-P. Salvetat, E. J akab, J.-M. Bonard and L. Forró. *J. Phys. Chem. B*, 105:7938-7943, 2001.
- [110] H. Zeng, J. Leburton, H. Hud and J. Weie. *Solid State Commu.*, 151:9-12, 2010.
- [111] F. Liang, A. K. Sadana, J. Chattopadhyay, Z. Gu, R. H. Hauge and W. E. Billups. *Nano Lett.*, 4:1257, 2004.
- [112] J. Guo, Y. Xu and C. Wang. *Nano Lett.*, 11(10): 4288, 2011.
- [113] J. Chen, Y. Liu, A. I. Minett, C. Lynam, J. Wang and G. G. Wallace. *Chem. Mater.*, 19: 3595, 2007.
- [114] A. L. M. Reddy, M. M. Shaijumon, S. R. Gowda and P. M. Ajayan. *Nano Lett.*, 9:1002, 2009.
- [115] M. Zheng, A.Jagota, E. D. Semke, B. A. Diner, R. S. Mclean, S. R. Lustig, R. E. Richardson and N. G. Tassi. *Nature Materials*, 2:338-342, 2003.
- [116] X. Tu, S. Manohar, A. Jagota and Ming Zheng. *Nature*, 460:250-253, 2009.
- [117] X. Tu and M. Zheng. A DNA-based approach to the carbon nanotube sorting problem. *Nano Research*. 1(3): 185-194, 2008.
- [118] Y. Liu, C. Chipot, X.Shao and W. Cai. *J. Phys. Chem. B*, 114:5783-5789, 2010.
- [119] P. M. Ajayan and O. Z. Zhou. *Topics in applied physics. Springer Berlin*, 80:391, 2001.
- [120] Y. Lin, F. Lu,Y. Tu and Z. Ren. *Nano. Lett.*, 4:191-195, 2004.
- [121] R. Martel, T. Schmidt, H. R. Shea, T. Hertel and Ph. Avouris. *App. Phys. Lett.*, 73:2447, 1998.

- [122] H. W. Ch. Postma, T. Teepen, Z. Yao, M. Grifoni and C. Dekker. *Science*, 293:76-79, 2001.
- [123] V. Derycke, R. Mertel, J. Appenzeller and Ph. Avouris. *Nano Lett.*, 1:453, 2001.
- [124] B. W. Smith, M. Monthieux and D. E. Luzzi. *Nature*, 296:323, 1998.
- [125] B. W. Smith, M. Monthieux and D. E. Luzzi. *Chem. Phys. Lett.*, 321:169, 2000.
- [126] S. Suzuki, F. Maeda, Y. Watanabe and T. Ogino. *Phys. Rev. B.*, 67:115418, 2003.
- [127] M.A.Gialampouki and Ch. E.Lekka. *J. Phys. Chem C*, 115(31):15172, 2011.
- [128] G. -H. Jeong, A. A. Farajian, R. Hatakeyama, T. Hirata, T. Yaguchi, K. Tohji, H. Mizuseki and Y. Kawazoe. *Phys. Rev. B*, 68(7):075410, 2003.
- [129] P. Kappen, A. Rider, P. J. Pigram and N. Brack. *J. Phys. Chem. C*, 115(43):21083, 2011.
- [130] S. Arcidiacono, J. H. Walther, D. Poulikakos, D. Passerone and P. Koumoutsakos. *Phys. Rev. Lett.*, 94:105502, 2005.
- [131] Z. Li, Z. Chena, G. Kanga and X. Hea. *Catalysis Today*, 165:25-31, 2011.
- [132] S. Yuan, Y. Kong, F. Wen and F. Li. *J. Phys.:Condens. Matter*, 19: 466203, 2007
- [133] S. Yuan, X. Wang, P. Li, F. Li and S. Yuan. *J. App. Phys.*, 104:054310, 2008.
- [134] P. A. Denis. *J. Phys. Chem. C*, 115(41):20282, 2011.
- [135] O. Byl, J. C. Liu, Y. Wang, W. L. Yim, J. K. Johnson and J. T. Yates Jr. *J. Am. Chem. Soc.*, 128:12090-97, 2006.
- [136] A. Striolo. *Nano Lett.*, 6: 633-639, 2006.
- [137] Y. Maniwa, H. Kataura, M. Abe, A. Udaka, S. Suzuki, Y. Achiba, H. Kira, K. Matsuda, H. Kadowaki and Y. Okabe. *Chem. Phys. Lett.*, 401:534-538, 2004.
- [138] G. Zuo, R. Shen and W. Guo. *Nano. Lett.*, 11: 5297, 2011.
- [139] L. Guan, K. Suenaga, T. Okazaki, Z. Shi, Z. Gu and S. Iijima. *J. Am. Chem. Soc. Comm.*, 129: 8954, 2007.
- [140] Y. Liu, R. O. Jones, X. Zhao and Y. Ando. *Phys. Rev. B*, 68:125413, 2003.
- [141] X. Zhao, Y. Ando, Y. Liu, M. Jinno and T. Suzuki. *Phys. Rev. Lett.*, 90:187401, 2003.
- [142] Z. Wang, X. Ke, Z. Zhu, F. Zhang, M. Ruan and J. Yang. *J. Phys. Rev. B(RC)*, 61:R2472-R2474, 2000.
- [143] X. Fan, L. Liu, J. Lin, Z. Shen and J. Kuo. *ACS Nano*, 3(11): 3788-3794, 2009.

- [144] Y. Wang, Y. Huang, B. Yang and R.Liu. *Carbon*, 46(2):276-284, 2008.
- [145] C. Zhao, R. Kitaura, H. Hara, S. Irie and H. Shinohara. *J. Phys. Chem. C*, 115(27): 13166, 2011.
- [146] R. Kuwahara, Y.Kudo, T.Morisato and K. Ohno. *J. Phys. Chem. A*, 115:5147, 2011.
- [147] A. Hirsch. *Angew. Chem.Int.Ed.*, 31(11):1853-1859, 2002.
- [148] V. Georgakilas, K. Kordatos, M. Prato, D. M. Guldi, M. Holzinger and A. Hirsch. *J. Am. Chem. Soc.*, 124(5):760-761. 2002.
- [149] D. Tasis, N. Tagmatarchis, A. Bianco and M. Prato. *Chem. Rev.*, 106:1105-1136, 2006.
- [150] C. N. R. Rao, B. C. Satishkumar, A. Govindaraj and M. Nath. *Chemphyschem*, 2: 78-105, 2001.
- [151] H. Kuzmany, A. Kukovecz, F. Simona, M. Holzweber, Ch. Kramberger and T. Pichler. *Synthetic Metals*, 141:113-122, 2004.
- [152] P. M. Ajayan. *Chem. Rev.*, 99(7): 1787-1800, 1999.
- [153] W. D. Knight, K. C. Klemenger, W.A.de Heer, W.A.Saunders, M. Y. Chou and M.L.Cohen. *Phys. Rev. Lett.*, 52: 2141, 1984.
- [154] T. P. Martin. *Phys. Rep*, 273:199, 1996.
- [155] T. P. Martin, U. Naher and H. Schaber. *Chem. Phys. Lett.*, 199:470, 1992.
- [156] B. K. Rao, S. N. Khanna and P. Jena. *J. Cluster Science*, 10: 477, 1999.
- [157] W. A. de Heer. *Rev. Mod. Phys.*, 65:611, 1993.
- [158] M. F. Jarrold and V. A. Constant. *Phys. Rev. Lett.*, 67:2994, 1991.
- [159] M. F. Jarrold and V. A. Constant. *J. Chem.Phys.*, 96: 9180, 1992.
- [160] J. M. Hunter, J. L. Fye, M. F. Jarrold and J. E. Bower. *Phys. Rev. Lett.*, 73:2063, 1994.
- [161] A. A. Shvartsburg and M. F. Jarrold. *Phys. Rev. A*, 60:1235, 1995.
- [162] H. W. Kroto, J. R. Heath, S. C. O'Brian, R. F. Curl and R.E. Smalley. *Nature*, 318:162, 1985.
- [163] Xi Li, Hongbin Wu, Xue-Bin Wang and Lai-Sheng Wang. *Phys. Rev. Lett.*, 81:1909, 1998.
- [164] L. Xiao and L.Wang. *Chem. Phys. Lett*, 392:452, 2004.
- [165] W Fa and J. Dong. *J. Chem. Phys.*, 124(11): 114310, 2006.

- [166] S Bulusu, X Li, L-S Wang and X-C Zeng. *Proc. Natl. Acad. Sci. USA*, 103:8326, 2006.
- [167] A. J. Cox, J. G. Louderback, S. E. Apsel and L. A. Bloomfield. *Phys. Rev. B*, 49:12295, 1994.
- [168] J. A. Alonso. *Structure and Properties of Atomic Nanoacluster*, Imperial College Press, 2005.
- [169] P. Jensen. *Rev. Mod. Phys*, 71:1695, 1999.
- [170] A. Aguado and M. F. Jarrold. *Annu. Rev. Phys. Chem*, 62:151-72, 2011.
- [171] S. Chacko and D. G. Kanhere. *Handbook of Nanophysics : Melting of Finite Sized Systems*. CRC Press, 1-22, 2010.
- [172] T. L. Hill. *The Thermodynamics of Small Systems Part I and Part II*. New York : Benjamin, 1963.
- [173] D. G. Kanhere, A. Vichare, and S. A. Blundell. *Reviews in Mordern Quantum Chemistry. Edited by K. D. Sen. World Scientific, Singapore*, 2001.
- [174] H. Haberland, T. Hippler, J. Donges, O. Kostko, M. Schmidt and B. von Issendorff. *Phys. Rev. Lett.*, 94:035701, 2005.
- [175] M. Schmidt, R. Kusche, W. Kronmüller, B. von Issendorff and H. Haberland. *Phys. Rev. Lett.*, 79:99, 1997.
- [176] G. A. Breaux, R. C. Benirschke, T. Sugai, B. S. Kinnear and M. F. Jarrold. *Phys. Rev. Lett.*, 91:215508, 2003.
- [177] G. A. Breaux, D. A. Hillman, C. M. Neal, R. C. Benirschke, and M. F. Jarrold. *J. Am. Chem. Soc.*, 126: 8628, 2004.
- [178] S. Chacko, K. Joshi, D.G. Kanhere and S.A. Blundell. *Phys. Rev. Lett.*, 92:135506, 2004.
- [179] A. A. Shvartsburg and M. F. Jarrold. *Phys. Rev. Lett.*, 85:2530, 2000.
- [180] K. Joshi, D. G. Kanhere, and S. A. Blundell. *Phys. Rev. B*, 66:155329, 2002.
- [181] M. Schmidt, R. Kusche, B. von Issendorff and H. Haberland. *Nature (London)*, 393:238, 1998.
- [182] R. Kusche, Th. Hippler, M. Schmidt, B. von Issendorff and H. Haberland. *Eur. Phys.*, 9:1, 1999.
- [183] M. Schmidt, R. Kusche, T. Hippler, J. Donges, W. Kronmüller, B. von Issendorff and H. Haberland. *Phys. Rev. Lett.*, 86:1191, 2001.
- [184] M. Schmidt and H. Haberland. *C. R. Physique*, 3: 327, 2002.

- [185] H. Haberland, T. Hippler, J. Donges, O. Kostko, M. Schmidt and B. von Issendorff. *Phys. Rev. Lett.*, 94:035701, 2005.
- [186] M-S. Lee, S. Chacko and D. G. Kanhere. *J. Chem. Phys.*, 123: 164310, 2005.
- [187] M-S. Lee and D. G. Kanhere. *Phys. Rev. B*, 75:125427, 2007.
- [188] S. Ghazi, M-S. Lee and D. G. Kanhere. *J. Chem. Phys.*, 128:104701, 2008.
- [189] M-S. Lee and D. G. Kanhere. *Phys. Rev. B*, 75:125427, 2007.
- [190] S. Chacko, D. G. Kanhere and S. A. Blundell. *Phys. Rev. B*, 71:155407, 2005.
- [191] G. A. Breaux, C. M. Neal, B. Cao and M. F. Jarrold. *Phys. Rev. Lett.*, 94:173401, 2005.
- [192] S. Krishnamurty, S. Chacko, D. G. Kanhere, G. A. Breaux, C. M. Neal and M. F. Jarrold. *Phys. Rev. B*, 73:045406, 2006.
- [193] K. Joshi, S. Krishnamurty and D. G. Kanhere. *Phys. Rev. Lett.*, 96:135703, 2006.
- [194] H. Häkkinen and U. Landman. *Phys. Rev. B*, 62:2287, 2000.
- [195] Li Xiao and L. Wang. *Chem. Phys. Lett.*, 392:452, 2004.
- [196] J. Wang, G. Wang and J. Zhao. *Phys. Rev. B*, 66:035418, 2002.
- [197] J. C. Idrobo, W. Walkosz, S. F. Yip, S. Ögüt, J. Wang and J. Jellinek. *Phys. Rev. B*, 76:205422, 2007.
- [198] J. Li, X. Li, H. Zhai and L. Wang. *Science*, 299:864, 2003.
- [199] S. Krishnamurty, G. Shafai, D. G. Kanhere, B. Soulé de Bas and M. J. Ford. *J. Phys. Chem. A*, 111:10769, 2007.
- [200] A. Karttunen, M. Linnolahti, T. Pakkanen and P. Pyykko. *ChemComm*, 4: 465, 2008.
- [201] L. Wang, S. Bulusu, W. Huang, R. Pal, L. Wang and X. C. Zeng. *J. Am. Chem. Soc.*, 129:15136, 2007.
- [202] J. Wang, J. Jellinek, J. Zhou, Z. Chen, R. B. King and P. Ragué Schleyer. *J. Phys. Chem. A*, 109:9265, 2005.
- [203] R. O. Jones, A. I. Lichtenstein and J. Hutter. *J. Chem. Phys.*, 106:4566, 1997.
- [204] B. V. Reddy, S. N. Khanna, and B. I. Dunlap. *Phys. Rev. Lett.*, 70:3323, 1993.
- [205] A. Dhavale, V. Shah and D. G. Kanhere. *Phys. Rev. A*, 57:4522, 1998.
- [206] M. Deshpande, D. G. Kanhere, I. Vasiliev and R. M. Martin. *Phys. Rev. A*, 65:033202, 2002.

- [207] C. Mottet, G. Rossi, F. Baletto, and R. Ferrando. *Phys. Rev. Lett.*, 95:035501, 2005.
- [208] J. L. Fye and M. F. Jarrold. *J.Phys.Chem.A*, 101:1836, 1997.
- [209] S. Shetty, S. Pal and D. Kanhere. *J. Chem. Phys*, 118:7288, 2003.
- [210] E. Janssens and P. Lievens. *Adv. Nat. Sci: Nanosci. Nanotechnol.*, 2:023001, 2011.
- [211] V. Kumar, S. Bhattacharjee and Y. Kawazoe. *Phys. Rev. B*, 61:8541, 1999.
- [212] M-S. Lee, S. Gowtham, H. He, Kah-Chun Lau, Lin Pan and D. G. Kanhere. *Phys. Rev. B*, 74:245412, 2006.
- [213] K. Joshi and D. G. Kanhere. *J. Chem. Phys.*, 119:12301, 2003.
- [214] K. Joshi and D. G. Kanhere. *Phys. Rev. A*, 65:043203, 2002.
- [215] S. Zorriasatein, K. Joshi and D. G. Kanhere. *Phys. Rev. B*, 75:045117, 2007.
- [216] X. Li, B. Kiran, L.-F. Cui and L.-S. Wang. *Phys. Rev. Lett.*, 95:253401, 2005.
- [217] L-M. Wang, R. Pal, W. Huang, X. Zeng and L. Wang. *J.Chem. Phys.*, 130:051101, 2009.
- [218] L-M. Wang *et.al.*, *Phys.Rev.B*, 79:033413, 2009.
- [219] N. S. Venkataramanan, R. Sahara, H. Mizuseki and Y. Kawazoe. *J.Phys.Chem. A*, 114:5049-5057, 2010.
- [220] J. L. Rao, G. Krishna Chaitanya , S. Basavaraja , K. Bhanuprakash and A. Venkataramana. *THEOCHEM* 803:89, 2007.
- [221] P. Pyykkö and N.Runeberg. *Angew. Chem. Int. Ed*, 41:2174, 2002.
- [222] S. Neukermans, E. Janssens, H. Tanaka, R. E. Silverans and P. Lievens. *Phys. Rev. Lett.*, 90:033401, 2003.
- [223] S. N. Khanna, B. K. Rao and P. Jena. *Phys. Rev. B*, 65:125105, 2000.
- [224] X. G. Gong and V. Kumar. *Phys. Rev. Lett.*, 70:2078, 1993.
- [225] V. Kumar and V. Sundarajan . *Phys. Rev. B*, 57:4939, 1998.
- [226] S. F. Lee and X. G. Gong. *Phys. Rev. B*, 70:075404, 2004.
- [227] A. P. Seitsonena, K. Laasonen, R. M. Nieminen and M. L. Klein. *J. Chem. Phys*, 103:8075, 1995.
- [228] A. Melzer, A. Schella, J. Schablinski, D. Block and A. Piel. *Phys. Rev Lett.*, 108:225001, 2012.
- [229] V. G. Grigoryan and M. Springborg . *Phys. Rev. B*, 83(15):155413, 2011.

- [230] F. Calvo. *Phys. Rev. B*, 85:060502, 2012.
- [231] A. Pulido, M. Boronat and A. Corma. *New J. Chem*, 35: 2153, 2011.
- [232] Y. Zhao, X. Kuang, B. Zheng, Y. Li and S. Wang. *J. Phys. Chem. A*, 115(5): 569, 2011.
- [233] Y. Gao, N. Shao, Y. Pei, Z. Chen and X. C. Zeng. *ACS Nano*, 5:7818, 2011.
- [234] C. M. Neal, A. K. Starace and M. F. Jarrold. *J. Am. Soc. Mass Spectrom*, 18:74, 2007.
- [235] D. E. Clemmer and M. F. Jarrold. *J. Mass Spectrom*, 32:577, 1997.
- [236] R. Parr and W. Yang. *Density Functional Theory of Atoms and Molecules*. Oxford University Press, 1989. ISBN 0-19-504279-4.
- [237] R. M. Martin. *Electronic Structure : Basic theory and practical methods*. Cambridge University Press, 2004. ISBN 0-521-78285-6.
- [238] J. Kohanoff. *Electronic Structure Calculations for Solids and Molecules : Theort and Computational Methods*. Cambridge University Press, 2006.
- [239] P. Hohenberg and W. Kohn. *Phys. Rev.*, 136:B864, 1964.
- [240] W. Kohn and L. J. Sham. *Phys. Rev.*, 140:A1133, 1965.
- [241] W. Kohn and P. Vashista. *Theory of the Inhomogeneous Electron Gas*. Edited by S. Lundqvist and N. H. March. New York : Plenum Press, 1983, chapter 2.
- [242] Perdew, D. C. Langreth and J. P. Perdew. *Phys. Rev. B*, 21:5469, 1980.
- [243] J. C. Phillips and L. Kleinman. *Phys. Rev.*, 116:287, 1959.
- [244] D. R. Hamman, M. Schlüter and C. Chiang. *Phys. Rev. Lett.*, 43:1494, 1979.
- [245] D. Vanderbilt. *Phys. Rev. B*, 41:7892, 1990.
- [246] W. A. Harrison. *Pseudopotentials in the Theory of Metals*. Benjamin, NY, 1966. ; M. L. Cohen and V. Heine. *Solid State Physics*. Academic, NY, 1970. Edited by H. E. Ehrenreich and F. Seitz and D. Turnbull.
- [247] L. Kleinman and D. M. Bylander. *Phys. Rev. Lett.*, 48: 1425, 1982.
- [248] P. E. Blöchl. *Phys. Rev. B*, 50:17953, 1994.
- [249] B. J. Alder and T. E. Wainwright. *J. Chem. Phys.*, 31(2): 459, 1959
- [250] R. Car and M. Parrinello. *Phys. Rev. Lett.*, 55: 2471, 1985.
- [251] L. Verlet. *Phys. Rev.*, 158:98, 1967.

- [252] W. C. Swope, H. C. Andersen, P. H. Berens and K. R. Wilson. *J. Chem. Phys.*, 76:637, 1982.
- [253] B. Silvi and A. Savin. *Nature (London)*, 371:683, 1994.
- [254] S. Nosé. *Prog. Theor. Phys. Suppl.*, 103:1, 1991.
- [255] A. M. Ferrenberg and R. H. Swendsen. *Phys. Rev. Lett.*, 61:2635, 1988.
- [256] H. Hiura, T. Miyazaki, and T. Kanayama. *Phys. Rev. Lett.*, 86:1733, 2001.
- [257] M.-S. Lee, D. G. Kanhere and K. Joshi. *Phys. Rev. A*, 72:015201, 2005.
- [258] A. Aguado, L. E. González and J. M. López. *J. Phys. Chem. B*, 108:11722, 2004.
- [259] D. Cheng, S. Huang and W. Wang. *Phys. Rev. B*, 74:064117, 2006.
- [260] S. Krishnamurty, K. Joshi, D. G. Kanhere and S. A. Blundell. *Phys. Rev. B*, 73:045419, 2006.
- [261] G. Kresse and J. Furthmüller. *Phys. Rev. B.*, 54:11169, 1996.
- [262] J. P. Perdew, K. Burke and M. Ernzerhof. *Phys. Rev. Lett.*, 77:3865, 1996.
- [263] S. Noše. *Mol. Phys.*, 52:255, 1984.
- [264] P. Labastie and R. L. Whetten, *Phys. Rev. Lett.*, 65:1567, 1990.
- [265] J-Y. Yi. *Phys. Rev. B*, 61:7277, 2000.
- [266] B. K. Rao and P. Jena. *J. Chem. Phys.* 111:1890, 1999.
- [267] S. Krishnamurty, K. Joshi, S. Zorriatein and D. G. Kanhere. *J. Chem. Phys.*, 127: 054308, 2007.
- [268] P. J. Dyson and D. M. P. Mingos. *Gold: Progress in Chemistry, Biochemistry and Technology*. Edited by H Schmidbaur, 511, 1999.
- [269] P. Pyykko. *Chem. Rev.*, 88:563, 1988.
- [270] J. H. Teles, S. Brode and M. Chabanas. *Angew. Chem.*, 99:2589, 1999.
- [271] M. Valden, X. Lai and D. W. Goodman. *Science*, 281:1647, 1998.
- [272] B. Yoon, H. Häkkinen, U. Landman, A. S. Wörz, J-M. Antonietti, S. Abbet, K. Judai and U. Heiz. *Science*, 307:403, 2005.
- [273] F. Furche, R. Ahlrichs, P. Weis, C. Jacob, S. Gilb, T. Bierweiler and M. M. Kappes. *J. Chem. Phys.*, 117: 6982, 2002.
- [274] X. Xing, B. Yoon, U. Landman and J. H. Parks. *Phys. Rev. B.*, 74:165423, 2006.
- [275] Y-K. Han. *J. Chem. Phys.*, 124:024316, 2006.

- [276] E. M. Fernandez, J. M. Soler, I. L. Garzon and L. C. Balbas. *Phys. Rev. B*, 70:165403, 2004.
- [277] W. Fa, C. Luo and J. Dong. *Phys. Rev. B*, 72:205428, 2005.
- [278] P. K. Jain. *Struc. Chem.*, 16: 421, 2005.
- [279] H. Häkkinen . *Chem. Soc. Rev.*, 37:1847, 2008.
- [280] H. Häkkinen and U. Landman. *Phys. Rev. B*, 62:R2287-R2290, 2000.
- [281] M. Ji, X. Gu, X. Li, X. Gong, J. Li and L-S. Wang. *Angew. Chem. Int. Ed*, 44:7119, 2005.
- [282] A. Lechtken, D. Schooss, J. R. Stairs, M. N. Blom, F. Furche, N. Morgner, O. Kostko, B. V. Issendorff and M. M. Kappes. *Angew. Chem. Int. Ed.*, 46:2944, 2007.
- [283] L-M. Wang, S. Bulusu, H-J. Zhai, X-C. Zeng and L-S. Wang. *Angew. Chem*, 46:2915, 2007.
- [284] S. Zorriasatein, K. Joshi and D. G. Kanhere. *J. Chem. Phys.*, 128:184314, 2008.
- [285] E. K. Yildirim and Z. B. Guvenc. *Modeling Simul. Mater. Sci. Eng*, 14:947, 2006.
- [286] E. K. Yildirim, M. Atis and Z. B. Guvenc. *Physica Scripta*, 75:111, 2007.
- [287] B. Soul'e de Bas, M. J. Ford and M. B. Cortie. *J. Phys. Condens. Matter*, 18:55, 2006.
- [288] S. Nosé. *Mol. Phys.*, 52:255, 1984.
- [289] S. Bulusu and X. C. Bulusu. *J. Chem. Phys*, 125:154303, 2006.
- [290] M. Bixon and J. Jortner. *J. Chem. Phys.*, 91:1631, 1989.
- [291] C. M. Neal, A. K. Starace, M. F. Jarrold, K. Joshi, S. Krishnamurty and D. G. Kanhere. *J. Phys. Chem. C*, 111:17788, 2007.
- [292] R. E. Smalley. *Rev. Mod. Phys.*, 69:723, 1997.
- [293] A. K. Geim and K. S. Novosolov. *Nature Materials*, 6:183, 2007.
- [294] A. H. Castro Neto, F. Guinea and N. M. R. Pere. *Phys. World*, 19:33, 2006.
- [295] A. H. Castro Neto, F. Guinea, N. M. R. Peres, K. S. Novoselov and A. K. Geim. *Rev. Mod. Phys.*, 109:81(1), 2009.
- [296] R. M. Ribeiro, N.M. R. Peres, J. Coutinho and P. R. Briddon. *Phys. Rev. B*, 78:075442, 2008.

References

- [297] E. Bekyarova, M. E. Itkis, P. Ramesh, C. Berger, M. Spinkle, W. A. De Heer and R. C. Haddon. *J. Am. Chem. Soc.*, 131:1336, 2009.
- [298] P. A. Denis, R. Faccio and A. W. Mombru. *ChemPhysChem*, 10: 715, 2009.
- [299] M. Z. S. Flores, P. A. S. Autreto, S. B. Legoas and D. S. Galvao. *Nanotechnology*, 20:465704, 2009.
- [300] T. Roman, W. A. Diño, H. Nakanishi and H. Kasai. *J. Phys. :Condensed Matter*, 21:474219, 2009.
- [301] M. Wu, X. Wu, Y. Gao and X. C. Zeng. *J. Phys. Chem. C*, 104:139-142, 2009.
- [302] M. J. Schmidt and D. Loss. *Phys. Rev. B*, 81:165439, 2010.
- [303] L. Hornekaer, E. Rauls, W. Xu, Z. Sljivancanin, R. Otero, I. Stensgaard, E. Laegsgaard, B. Hammer and F. Besenbacher. *Phys. Rev. Lett.*, 97:186102, 2006.
- [304] L. Hornekær, Z. Sljivancanin, W. Xu, R. Otero, E. Rauls, I. Stensgaard, E. Laegsgaard, B. Hammer and F. Besenbacher. *Phys. Rev. Lett.*, 96:156104, 2006.
- [305] D. Soriano, F. Muñoz-Rojas, J. Fernández-Rossier and J. J. Palacios. *Phys. Rev. B*, 81: 165409, 2010.
- [306] O. V. Yazyev. *Rep. Prog. Phys.*, 73:056501, 2010.
- [307] O. V. Yazyev. *Phys. Rev. Lett.*, 101:037203, 2008.
- [308] O. V. Yazyev and L. Helm. *Phys. Rev. B*, 75:125408, 2007.
- [309] B. S. Pujari and D. G. Kanhere. *J. Phys. Chem. C*, 113:21063-7, 2009.
- [310] A. V. Shytov, D. A. Abanin and L. S. Levitov. *Phys. Rev. Lett.*, 103:016806, 2009.
- [311] A. K. Singh, E. S. Penev and B. I. Yakobson. *ACS Nano*, 4:3510, 2010.
- [312] J. P. Perdew, K. Burke and M. Ernzerhof. *Phys. Rev. Lett.*, 78:1396, 1997.
- [313] E. H. Lieb. *Phys. Rev. Lett.*, 62:1201-4, 1989.
- [314] S. Bhandary, O. Eriksson, B. Sanyal and M. I. Katsnelson. *Phys. Rev. B*, 82:165405, 2010.
- [315] Y-W. Son, M. L. Cohen and S. G. Louie. *Phys. Rev. Lett.*, 97:216803, 2006.
- [316] S. Haldar, D. G. Kanhere and B. Sanyal. *Phys. Rev. B*, 85:155426, 2012.
- [317] P. A. Denis. *J. Phys. Chem. C*, 115:13392, 2011.
- [318] P. Havu, M. Ijäs and A. Harju. *Phys. Rev. B*, 84:205423, 2011.

- [319] A. I. Shkrebtii, E. Heritage, P. McNelles, J. L. Cabellos and B. S. Mendoza. *Graphene and graphane functionalization with hydrogen: electronic and optical signatures. Phys. Status Solidi C*, 9:1378-1383, 2012.
- [320] S. Ghosh, K. V. Ramachandran, K. S. Sood. *Europhys. Lett*, 65:678, 2004.
- [321] L. Kolesnikov, J. M. Zanotti, C. K. Loong and P. Thiyagarajan. *Phys. Rev. Lett.*, 93: 0355001, 2004.
- [322] D. Takaiwa, I. Hatano, K. Koga and H. Tanaka. *PNAS*, 39: 105, 2008.
- [323] B. Xu and B. C. Pan. *J. Phys. Chem. C*, 113:567, 2008.
- [324] H. Abou-Rachid, A. Hu, V. Timoshevskii, T. Song and L.-S. Lussier. *Phys. Rev. Lett.*, 100:196401, 2008.
- [325] I. Garg, H. Sharma, K. Dharamvir, V.K. Jindal and D. G. Kanhere. *J. Phys. Chem. C*, 44:114, 2010.
- [326] V. V. Ivanovskaya, C. Köhler and G. Seifert. *Phys. Rev. B*, 75:075410, 2007.
- [327] T. W. Chamberlain et.al. *ACS nano*, 6(5): 3943, 2012.
- [328] I. Lebedeva, A. Popov, A. Knizhnik, A. N. Khlobystov and B. Potapkin. *Nanoscale*, 4:4522, 2012.
- [329] L. Xie, H. Wang, C. Jin, X. Wang, L. Jiao, K. Suenaga and H. Dai. *J. Am. Chem. Soc.*, 133:10394, 2011.
- [330] Y. Jiang, H. Li, Y. Li, H. Yu, K. M. Liew, Y. He and X. Liu. *ACS Nano*, 5(3):2126-2133, 2011.
- [331] Y. Li, F. Sun and H. Li. *J. Phys. Chem. C*, 115(38):18459, 2011.
- [332] K. V. Bets and B. I. Yakobson. *Nano Research*, 2:161, 2009.
- [333] M. G. Zeng, L. Shen, Y. Q. Cai and Y. P. Feng. *Appl. Phys. Lett.*, 96:042104, 2010.

List of Publications

1. Electronic structure of graphene and hydrogenated graphene nanoribbons encapsulated in single walled carbon nanotubes.
Prachi Chandrachud and D. G. Kanhere.
Communicated (2012).
2. A systematic study of electronic structure from graphene to graphane.
Prachi Chandrachud, B. S. Pujari, S. Haldar, B. Sanyal and D. G. Kanhere.
J. Phys.: Condens. Matter, 22:465502, (2010).
3. Stability of gold cages (Au_{16} and Au_{17}) at finite temperature.
Prachi Chandrachud, K. Joshi, S. Krishnamurthy and D. G. Kanhere.
Pramana, 72(5): 845, (2009).
4. Thermodynamics of carbon-doped Al and Ga clusters: Ab initio molecular dynamics simulations.
Prachi Chandrachud, K. Joshi and D. G. Kanhere.
Phy. Rev. B, 76: 235423, (2007).